Design and Fabrication of Microarchitected Thermoelectric Generators: Prospects and Challenges

Saeed Asadikouhanjani[1], Ali Zolfagharian[2] and **Mahdi Bodaghi[1,*]**
[1]Department of Engineering, School of Science and Technology, Nottingham Trent University, Nottingham, NG11 8NS, UK; corresponding author: mahdi.bodaghi@ntu.ac.uk
[2]School of Engineering, Deakin University, Geelong, Victoria, 3216, Australia

Abstract

Solid state devices called thermoelectric generators (TEGs) can convert waste heat from production into electrical power. For emerging devices like thermally integrated energy-autonomous devices, medicinal equipment, and Internet of things, μ-TEGs are essential because they can produce power even from minor temperature gradients. An review of the history and state-of-the-art of μ-TEGs is provided in this article. In addition, it concentrates on highly effective approaches for achieving high-performance miniature vertical thermoelectric (TE) devices. Design and optimizing methodologies for vertical μ-TEGs are also investigated since their output power, efficiency and integrity are critical to the architecture. Improving electrical and mechanical performance may be achieved via optimization methods, including multi-objective and finite-dimensional optimization in three dimensions (3D). Additionally, the idea and latest advancements of employing the 3D micro-additive manufacturing (micro-AM) technique for producing μ-TEGs are discussed, along with their advantages and disadvantages. The concept of "micro architected TEGs" as opposed to "μ -TEGs" is provided by the new paradigm of digital additive manufacturing and architected material concept, which also broadens the scope of material adaptability and innovative structural design. The difficulties experienced are summed up when increasing the output power of μ-TEG and the prediction of future trends is the final step.

GA: This review explores the significance of micro thermoelectric generators (μ-TEGs) in harnessing waste heat for power in emerging applications like energy-autonomous devices, medical equipment, and IoT. Focusing on high-performance miniature vertical thermoelectric devices, it delves into design, optimization methodologies, and 3D micro-additive manufacturing. Micro-architected TEGs are introduced, highlighting challenges in enhancing output power and predicting future trends in μ-TEG development.

Key Words: microarchitected vertical TEGs, multi-objective optimization, finite element method, 3D micro-AM technique

1-Introduction

Miniaturized systems' growing desire for ubiquitous power generation on a worldwide scale, drives the creation of novel materials and technologies that can capture environmental energy and offer wire- and battery-free, long-lasting autonomy. Energy harvesting or scavenging technology, which takes advantage of the abundant energy found in nature, can be used to run low-power equipment.

This article has been accepted for publication and undergone full peer review but has not been through the copyediting, typesetting, pagination and proofreading process, which may lead to differences between this version and the Version of Record. Please cite this article as doi: 10.1002/adem.202301609.

It appears that the power density (tens of microwatts to milliwatts per cubic centimeter), which might be needed by microelectronic devices, wireless sensor network nodes, and remote actuators can all be powered by ambient energy sources like vibrational, solar, and thermal. [1, 2]. A small-power revolution in energy harvesters could be led by thermoelectric generators (TEGs), which can convert heat gradients that naturally exist into electricity. In proper circumstances, such solid-state devices may become a long-term power source for low-power miniaturized system configurations due to their excellent reliability, scalable size, comparably inexpensive, zero operating noise, zero pollution, and a wide working temperature range [1, 3-6]. The efficiency of converting current in thermoelectric (TE) devices, however, is significantly lower than in other mechanical systems. So, geometry and material optimization have been widely investigated recently, maintaining low material costs and enhancing the performance and TEs output. In these sectors, improving TE equipment conversion efficiency represents a considerable difficulty. Hicks and Dresselhaus demonstrated in the 1990s that low-dimensional TE materials, such as quantum wires and quantum wells, display exceptionally large ZT values, where ZT is dimensionless figure of merit. [7, 8]. Low-dimensional nanostructures were shown to be a novel method to precisely modify the transmission and scattering features of electrons and phonons in TE materials, thereby improving their TE properties [9-11]. By adding Pt nano-inclusions through pulsed laser deposition, Sun et al. improved the TE properties of n-type $Bi_2Te_{2.7}Se_{0.3}$ thin films [12]. Sumithra et al. improved the ZT of Bi_2Te_3 specimens by introducing semimetal nano inclusions [13]. From a material perspective, microgenerators are switching from pellet-like macrostructures to nanostructures such as thin films, superlattices, and nanowires, which provide a base for greater material efficiencies and reduced prices. Although researchers successfully achieved TE materials using high ZT and PF (power factor) via the utilization of low dimensions and nanostructures, the functionality of the majority of such materials was evaluated, and they seemed not to be implemented in practice.

Another exciting strategy for boosting TE efficiency and power output is to optimize the design of μ-TEGs devices. This is because small devices may accommodate a variety of material pairs, producing high voltages even at extremely small temperature fluctuations. Despite recent advances in TE material efficiency, the geometry of μ-TEGs remains behind, and n- and p-type TE materials can only be arranged in a standard planar manner, resulting in inadequate power output. To evolve high-performance TE devices, appropriate design, contacts, thermal interfaces, mechanical characteristics, interconnects, packaging methods, and TE materials possessing an excellent figure of merit are required. But unlike conventional ones, μ-TEGs have a distinct structure. First, it appears that the operating temperature of μ-TEG is normally low, and second, the effect of semiconductor and metal contact resistance is noticeable [14]. Third, the contact thermal resistance must be considered [15]. Depending on the device's heat flow direction, the suggested designs could be classified into two groups: in-plane (lateral) or cross-plane (vertical) arrangements. The substrate chosen in the in-plane design seems to have a heat flux that is parallel to it and preferentially has a low thermal conductivity to reduce parasitic heat fluxes. Heat flows perpendicular to the substrates, which are anticipated to be superior heat conductors, in the cross-plane configuration. In terms of physical construction, cross-plane (vertical) design permits more pair packing and hence more power per unit area. However, TE materials for vertical configurations must be deposited in more extensive layers to limit heat transfer between the hot and cold sides. In-plane (horizontal arrangement), planar deposition enables the manufacture of couplings with a higher aspect ratio (length versus thickness) but at a reduced packing density and power density per unit area (Table 1) [16-19].

Table1. Design, material, performance factor (ϕ), the literature's figure of merit (Z) of TEGs [19].

P(μWcm^{-2})	ϕ(μWcm^{-2}K^{-2})	material	ΔT	TC Layout/heat flow	Z(K^{-1})
0.13 mW	1.7	BiTe(p-n)	98	Radial/hot gas	
755.5	0.29	BiTe(p-n)	51.2	Vertical/Vertical	2*10^{-5}
30.3	0.075	Si-n/Al	20	Lateral/Lateral	
4.2	2.3*10^{-3}	Cu/Ni	40	Vertical/Vertical	1.5*10^{-5}
1.3	0.052	Si (p-n)	5*	Lateral/Lateral	4*10^{-5}

*Considering ΔT_G across the generator calculates in software ANSYS and not the real temperature difference (130K) between hot plate and cooler

So, to power micro-systems, smart selection of the innovative μ-TEGs design is required in addition to material selection. The power production, efficiency, and structural integrity of vertical TEGs are therefore being optimized by architectural designs and geometric structural modification. Techniques for design and geometry optimization, such as three-dimensional (3D) finite elements modeling, multi-objective optimization techniques, or combinations of those, are investigated. Software programs, such as COMSOL and ANASYS, which enable simultaneous integration of all TE influences and may provide great forecast accuracy for TEG optimization, make 3DFEM accessible. After conducting a theoretical analysis, Sahin and Yilbas developed a formula for TEGs' output power and efficiency using different leg shapes by FEM [20]. The shape parameter benefits efficiency for various tested hot side temperatures and external load resistances. Thimont and LeBlanc studied TEGs' output power and thermal resistance using varied leg designs. Rectangular, triangular, and circular hollow cross-section geometries were considered [21]. When creating novel TE materials and devices through FEM, one of the difficulties, which should be considered, is the structural durability of TEGs. Erturun et al. established the significance of leg geometry in influencing leg stresses and stated that leg geometry might be a factor in reducing total module stresses [22, 23]. Yilbas et al. investigated rectangular and tapered pin designs while running thermal and stress finite element simulations on a horizontal TEG. The results indicate that von Mises stress is greatest at hot and cold side intersections. Furthermore, it was discovered that a design with tapered pins reduces thermal stress in comparison to a setup with rectangular pins [24]. Since all the TE devices' characteristics are totally connected and thus have coupled impacts on its performance, achieving meaningful performance improvement by focusing on one parameter is impossible. Various researchers have utilized distinct optimization strategies. Artificial bee colonies (ABC), harmony search (HS), particle swarm optimization (PSO), and genetic algorithms (GA) are examples of nature-inspired multi-parameter and multi-objective optimization techniques [25]. There is a possibility to use FEM and optimization approaches simultaneously. For instance, a 3D ANASYS TEG model has been linked using the multi-objective genetic algorithm (MOGA) by Chen et al. [26, 27], showing strong correlations with experimental data. In order to facilitate the multi-objective optimization of a TE energy conversion system, Meng et al. [28] develop a TEG model in COMSOL. Aside from that, artificial neural networks (ANNs) have drawn a lot of interest due to their effectiveness in processing huge datasets and their revolutionary effects on the fields of computer vision and voice recognition [29, 30]. Trained ANNs could cooperate to optimize the leg height, leg width, fill factor, and connection height of the TEG. Yuxiao Zhu [32] describes the first forward modeling of TEG utilizing fully connected ANNs relying on deep learning, which displays good accuracy and efficiency. The

novel ANN can be used to predict TEG performance in various operational conditions without any prior knowledge of the TE device (such as constant temperature differences and constant heat flux). The ANN seems capable of learning the complicated underlying interactions in the dataset and undertaking assumptions in a clear and precise way after training utilizing a dataset obtained from a 3D TEG model using COMSOL simulations. It takes into account the nonlinear TE effects, electrical contact resistance, temperature-dependent TE material properties, and heat transfer with the environment.

The current trend in many industries, including TEG, is to make products smaller. This calls for better micro- and nano-fabrication technologies, as well as an analysis of how the shape of a module's legs affectsitsability to convert energy. These 3D structures play a crucial role in creating a high-temperature differential over a TE leg and obtaining high power in a μ-TEG [33-39]. Various micro-fabrication methods, such as micro-electro-mechanical-system (MEMS) methods based on traditional lithography, deposition, etching, and release, are used to create miniature TEG. However, current techniques are limited to the fabrication of patterned, planar two-dimensional (2D) TE legs, and it is too expensive to create unique micro goods with complicated 3D microstructures and high aspect ratios [40]. As was already indicated, these 3D structures seem to be particularly important for generating high power and a significant temperature gradient over a μ-TEG. Additionally, traditional TEG fabrication involves the well-known but time-consuming steps of (a) powder synthesis, (b) pressing, (c) dicing and polishing, (d) metallization, (e) leg dicing, (f) soldering, and (g) module assembly [41-44]. To improve the capabilities of microfabrication technology in the real 3D micro component manufacturing arena, creative approaches like micro additive manufacturing (micro-AM) may be taken into consideration. The rise in the AM market during the previous eight years has been remarkable, with an estimated annual increase of 27% and an estimated value of almost $7 billion. Although macroscale AM tools and devices have experienced the majority of such expansion, attention to the innovation of microscale AM technologies has expanded due to the ongoing need for miniature device in the electronics, biotechnology, medical, automotive, and optical industries [39, 45-47]. However, while reducing traditional AM to the microscale, there are substantial obstacles, such as restricted build rates, component complexity, and available materials. The use of AM for TE materials and devices still seems comparatively novel, even though AM has grown widespread. The viability of the production strategy for such semiconductor materials must have been proven utilizing AM methods on a range of low and high temperature TE materials, such as bismuth telluride, higher manganese silicide (HMS), half Heusler, and skutterudite. Because of such improvements in production capacity, wide ranges of TE leg geometries that seem to be formerly unfeasible are now viable [48–58]. TE materials were produced using various methods, including stereolithography, extrusion-based printing, and selective laser sintering [58-65]. Recent advancements in AM (or 3D printing) have represented a novel age crucial to creating intricate, multiscale structures and gave rise to previously unattainable structural, mechanical, chemical, thermal, and functional mixtures. By integrating AM technologies with advanced materials and digital freeform design, AM is transforming the μ-TEG. Architecture has always had a significant effect on material characteristics and structural efficiency. Architected materials (i.e., materials with architectures added to them) allow material scientists to customize the physical characteristics [66–68]. Architected materials with ideally planned topologies (cellular or completely dense, single or multiphase, periodic or functionally graded) exhibit several distinguishing characteristics. Specifically, they make it possible to decouple features conventionally associated with monolithic materials that compete with one another, such as decoupling thermal conductivity and the Seebeck coefficient [69].

Given the architected materials and the digital design used for AM in micro-TE technology, the name "μ -TEG" is no longer suitable and must be replaced by the name "microarchitected TEG". This review presents a comprehensive examination of the existing research on μ-TEGs as well as numerous developments in improving μ-TEGs' performance from the viewpoints of design, geometry optimization, and μ-TEG manufacturing technology. Along with improving electrical performance, modifying TE design and structure may also increase mechanical functioning and structural integrity (efficiency and output power). Finally, suggestions for future study in the μ-TEGs geometry-structure optimization and micro-fabrication approaches are presented as a reference to involved investigators.

2- Classification of μ-TEGs

The last decade has seen the investment of many efforts in the development of μ -TEG. Many of these initiatives will be briefly reviewed. One method to classify μ -TEG is in accordance with their structures as outline below:

2.1- Vertical structure

Micro-thermoelectric generators feature both vertical heat and current flow (refer to Figure 1a) [43]. The typical μ -TEG structure, sometimes referred to the vertical or sandwich structure, is what is employed in most commercial TE products. The huge output power, high conversion efficiency, and straightforward construction of these type of μ-TEGs are generally considered to be their advantages. Nonetheless, their major drawbacks compared to other types are their high technological requirements and difficult fabrication. Considering their “out-of-the-plane” (vertical) architecture, the replication of such geometry using the microelectronics technology like MEMS is difficult. The reason for such a limitation is merely related to the process because, historically, the manufacturing of lateral structures on silicon wafers has been made possible by microelectronics methods, and typically, the vertical distances between layers have been kept to a minimum. The combination of MEMS and thick film technologies is regularly employed for the fabrication of μ-TEGs with a vertical structure. The thermopile length is determined by the film thickness, which, in turn, determines the thermal resistance of the μ-TEG. Generally speaking, thicker films will result in better performance because the package has a higher thermal resistance. Nonetheless, the film thickness is constrained by cost limitations and the level of fabrication technology. As far as we are aware, the first business to adopt a vertical structure μ-TEGs to supply the power for its wristwatches was the Japanese company Seiko [70]. The watches featured 1 W energy consumption with a driving voltage of 1.5 V. The wristwatch is shown schematically, and the μ-TEGs’s scanning electron microscopy (SEM) image is shown in Figure 1 b. The 104 thermocouples made up the μ-TEGs, which had overall dimensions of 2 mm × 2 mm × 1.3 mm. The dimensions of a single thermocouple were 80 μm×80 μm×600 μm. Given the superb thermoelectric efficiency of The Bi-Te compounds at around room temperate, they were selected

as the TE material. Electrical output power at its highest estimate was 22.5 W. Jet Propulsion Laboratory's G. J. Snyder et al. (2003) introduced a TE micro-device made using a MEMS-like electrochemical process [71]. The cited device included 126 N-type and P-type (Bi, $Sb)_2Te_3$ TE elements (60 µm in diameter and 20 µm tall). Metal interconnects were created using a 3-um-thick Au and Ni layer to lower the contact resistance. J. F. Li et al. (2003), integrated materials processing and MEMS technology into a new process to manufacture a high aspect-ratio µ-TEG and densely aligned fine-scale thermocouples [72]. They filled a silicon mold with TE materials after micromachining the silicon mold. Ultimately, the P-type and N-type legs were coupled in sequence to create a thermopile. The SEM image of the µ-TEGs is shown in Figure 1c. Although the authors could successfully fabricate TE elements of 40 µm cross-sectional width and 300 µm height, they did not report the performance of those elements. H. Bottner et al. (2004) proposed the first TE apparatus based on the V-VI compounds (Bi, $Sb)_2Te_3$ and Bi_2Te_3, which is producible by fusing the traditional thin film and microsystem technologies [73]. Initially, co-sputtering was used to create n- and p- materials on two wafers up to around 20 m of layer thickness, respectively. Subsequently, through chip-to-wafer, wafer-to-wafer, or chip-to-chip soldering, the two-wafer procedure eventually resulted in the manufacture of devices. At a temperature differential of 5°K and matched load resistance, the µ-TEGs's maximum power output was 0.67 W. This concept was taken by the Micropelt technology as the technical answer for highly dense µ-TEGs. H. Bottner et al. delivered a report on the most recent state of Micropelt -TEG development TE [73]. At that time, devices with up to ~8000 p-n-couples per cm^2 were supported by the Micropelt platform technology. The obtained open circuit voltage was about 2.3 V at a 10 K temperature difference. The low-power wireless sensor networks (WSNs) power supply could be powered by the system's maximum power output, which was 2.8 mW.

Flexible and completely integrated TEGs were presented by Glatz et al. (2009) [74]. Using Bi_2Te_3- and Ni-Cu- based µ-TEGs, the overall system optimization was verified. The created devices produced up to 2.6×10^{-3} $\mu Wcm^{-2}K^{-2}$ and 0.29 $\mu Wcm^{-2}K^{-2}$ for the equipment with Ni-Cu thermocouples and Bi2Te3-based generators in the planar state, respectively. Elyamny et al. [75] suggested a chip-level vertical µ-TEGs on the basis of a high-density SiNW array developed through metal assisted chemical etching (MACE) technique, as depicted in Figure 1d. The thermopile featuring a height of 100µm was composed of doped SiNW bundles. The $1\times1cm^2$ sample was capable of generating 1 $\mu Wcm^{-2}K^{-2}$ across the SiNW. According to Li et al. [76], who employed polyimide as the filler material, their µ-TEGs's efficiency dramatically increased. It now has a maximum power output of 0.47 W and operates with an experimental setup temperature differential of 70 K. In order to create TE devices compatible with mass production methods and the most advanced semiconductor industry, a sputtering technique based on integrated $Bi_{2+x}Te_{3-x}$ at the wafer level was presented by Böttner et al. [77]. This team created a high voltage thin-film thermogenerator that can deliver 0.14 VK^{-1} and is currently available for purchase (refer to Figure 1e). A revolutionary technology was also created by Venkatasubramanian, who created a high-voltage µ-TEG with an output power of 1.5 mW at a temperature of 10 K (0.025 VK^{-1}) and an open circuit voltage of 0.25 V [78]. This generator was based on a Bi_2Te_3-Sb_2Te_3 superlattice.

Li et al. also developed a top-down CMOS (complementary metal-oxide-semiconductor)-compatible high-density silicon nanowire-based TEG [79]. Referring to Figure 1f-h, the 25 mm^2 TEG is made up of tightly packed bundles of alternating p- and n-type silicon nanowires (Si NW), each of which has a height of 1 µm and a diameter of 80 nm (each bundle functions as a single TE component

with 540 × 540 wires). The constructed TEG has an evaluated temperature gradient of 0.12 Kelvin across the apparatus, and is capable of providing a short circuit current of 3.79 µA and an open-circuit voltage of 1.5 mV . Given that silicon is the second most common material in the Earth's crust and that it has a developed and established technology, it is regarded as an ideal material used to develop all CMOS devices. If silicon is nanostructured into nanomeshes, porous membranes, or nanowires, it can improve the bulk TE performance of this material with a ZT ≈ 0.01. For the unique situation of single silicon nanowires, Hochbaum et al. and Boukai et al.'s separate investigations revealed a startling improvement in the TE properties (Refer to Figure 1i) associated with the low material dimensionality [80, 81]. According to the study conducted by Boukai et al., one can achieve ZT values representing an approximate enhancement of 100-fold, such as ZT ≈ 1 at 200 K, over bulk Si and a broad range of temperatures through variation of impurity doping levels and the nanowire size. Additionally, Hochbaum et al. demonstrated that ZT = 0.6 could be attained in a rough Si NW with a diameter of around 50 nm. They explained this improvement in ZT as the result of effective scattering over the whole phonon spectrum brought about by the introduction of nanostructures at diverse length scales. Lindeberg demonstrated a small thermopile construction with up to 224 thermocouple legs placed vertically in a polyimide flexible material (Figure 1j). The thermopile is produced using PCB-like (printed circuit board) fabrication and goes through optimization for the detection of IR heat radiation. A few hundred nickel/antimony electrodeposited sub-micrometer-sized strands make up each TE leg, and the interconnections with a dog-bone shape continue within the foil plane laterally [82]. As a result, the heat moves perpendicular to the foil's surface plane. The best thermopile exhibited a 3.6 mV response, which corresponds to a response to the irradiance of 4.3 V mm^2 W^{-1} or 0.88 V W^{-1}. The PbTe nanocrystal-coated glass fibers are capable of application for TE purposes. To study such a remarkable possibility, representative results from a study by Daxin Liang et al. [83] are presented in Fig. 1k, including the temperature dependence of their electrical conductivity, thermal conductivity between 300 and 400 K along the axial direction of the fibers, and Seebeck coefficient. The electrical conductivity of the glass fibers coated with PbTe nanocrystals is enhanced from 104.4 $S{\cdot}m^{-1}$ at 300 Kelvin to 172.4 $S{\cdot}m^{-1}$ at 400 Kelvin. Figure 1l illustrates the temperature dependency of the Seebeck coefficient of the glass fibers covered in PbTe nanocrystals. The p-type conduction is shown by the Seebeck coefficient's positive values. The measurement of the Seebeck coefficient indicates an ascending trend from 1201.7 $uV{\cdot}K^{-1}$ at 300 Kelvin to 1542.4 $uV{\cdot}K^{-1}$ at 400 Kelvin. The measured thermal conductivity at 300 Kelvin is 0.228 $W{\cdot}m^{-1}{\cdot}K^{-1}$ that increases to 0.234 $W{\cdot}m^{-1}{\cdot}K^{-1}$ around 350 Kelvin, and subsequently declines to 0.226 $W{\cdot}m^{-1}{\cdot}K^{-1}$ at 400 Kelvin. For the glass fibers coated with PbTe nanocrystals, the estimated ZT and power factor are raised from 0.20 and 0.15 $mW{\cdot}m^{-1}{\cdot}K^{-2}$ at 300 Kelvin to 0.73 and 0.41 $W{\cdot}m^{-1}{\cdot}K^{-2}$ at 400 Kelvin, respectively. To create an all-silicon nanostructured TEG, D Dávila et al. combined top-down microfabrication techniques with bottom-up intrinsic crystalline silicon nanowire arrays. They also proposed a vertical device architecture (refer to Fig.1m, n). In order to fabricate such a device, by bonding bottom and top silicon structures via nanowires, silicon nanowires were appropriately integrated vertically on hexagonal patterned microstructures, defining the TE legs of the generator. On free silicon surfaces, high-density epitaxial growth of nanowires was made possible by using gold catalytic nanoparticles as mediators [84].

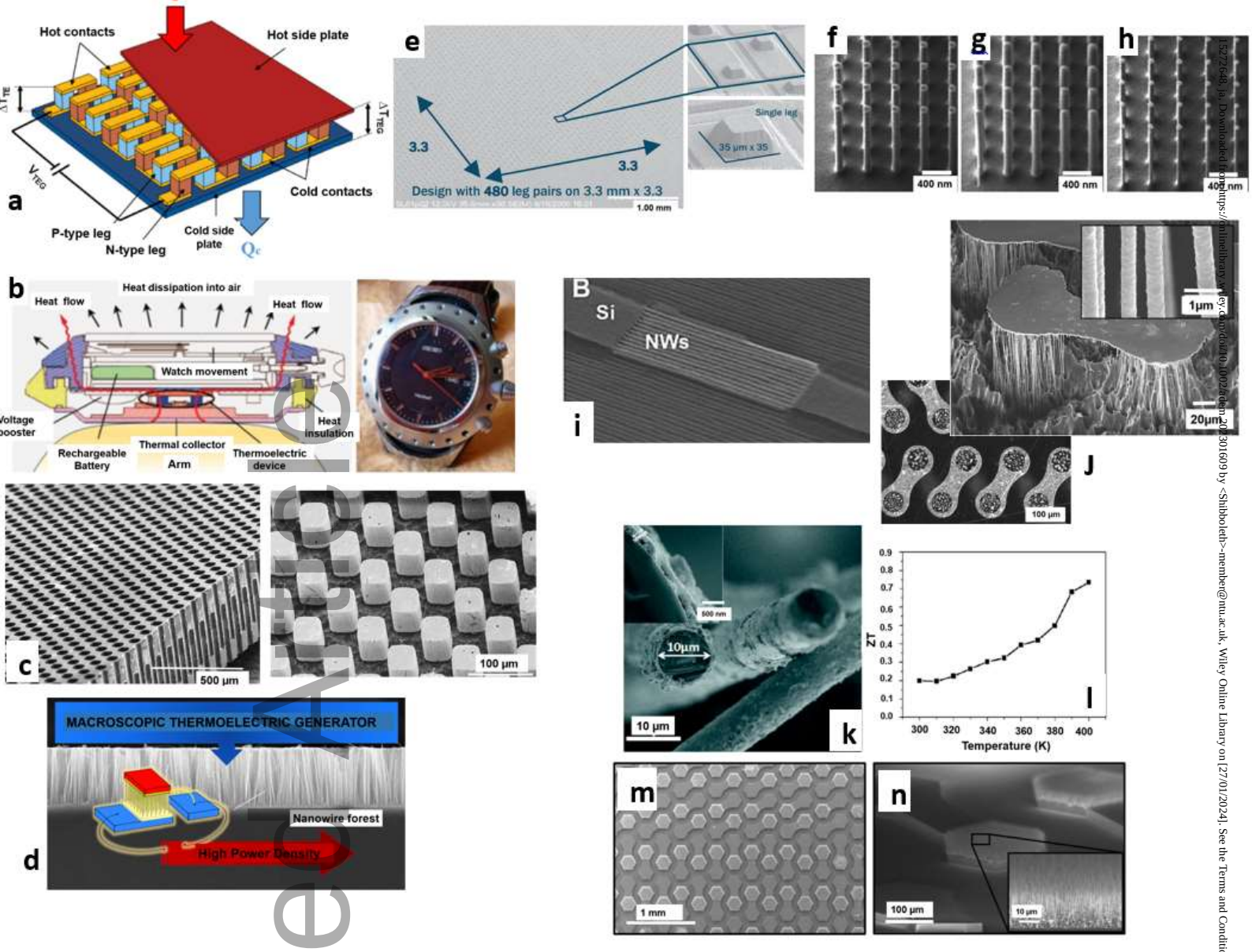

Fig. 1. (a) Schematic view of a typical vertical μ-TEG [43]. (b) Overview of the thermoelectric wristwatch [70]. (c) SEM photograph of µ-TEG by silicon molding process [72]. (d) High-density SiNW array serves as the foundation for the chip-level vertical µ-TEG structure [775]. [e] Micropelt created a high voltage thin-film thermogenerator [77]. a SiNW array's SEM pictures [f] as etched, [g] after heat oxidation to shrink the diameter of the SiNW and (h) after SiO2 has been removed in order to confirm that the SiNWs' diameter has decreased [79]. (i) EE Si nanowire array in cross-sectional SEM picture [81]. (j) Surface interconnections (or "dog-bone" structures) are visible in the close-up view of a microscope, and a SEM image reveals bundles of sub-micron strands that are coupled to the surface interconnections of one thermocouple via the MW -via. The tiny is shown in the up-close inset picture [82]. glass strands that are bendable and have thermoelectric nanocrystals on them. (k) SEM image of the glass fibers coated with PbTe to create a flexible thermoelectric material. (l) zT values over the temperature range of 300–400 K [83]. (m) Before connecting the top and bottom structures, the SEM picture of the device shows the hexagonal design of the thermoelectric elem ents. (n) Si NWs have been deliberately produced in highly ordered arrays on specific Si structures [84].

2.2- Lateral structure

A µ-TEGs featuring both lateral heat and current flow, as depicted in Figure 2a [43]. In lateral structure due to its interoperability with IC planar technology, the fabrication of µ-TEGs is simple. The vertical scheme has a simpler fabrication technique since the interconnections between the thermocouple legs in this planar configuration are made on the same surface level as the substrate, but it takes up more space. Silicon-based thermopiles are frequently made using this "in-the-plane" or horizontal construction for almost all commercial IR or temperature sensors. However, the lateral construction µ-TEGs' drawbacks include packaging challenges, enabling the chip-like device to be exposed to an in-plane temperature difference, and large parasitic heat flux going through the membrane, which results in its generally poor efficiency. Because of this, the lateral structure is rarely utilized to generate electricity and is usually used for other types of sensing, such as IR sensors, power sensors, or flow sensors. Leonov et al. (2011) from the IMEC/Holst Center suggest a

bulk-micromachined membraneless in-plane thermopile, as depicted in Figure 2c [85, 86]. Its output power on a matched external load was 2.34*10 $^{-3}$ μWK^{-2}, although its open-circuit output voltage could reach up to 95.0 mVK^{-1}. In addition, two plausible assembly schemes were presented by the authors, as depicted in Figure 2b. Nevertheless, it was challenging to realize efficient assembly of the in-plane μ-TEG. A lateral structure μ-TEG was presented by X. Yu et al. (2012) based on CMOS MEMS, which was equipped with an efficient path of heat dissipation [87] presented in Figure 2d. To efficiently dissipate the heat from the in-plane thermopile and lower the thermal contact resistance, the silicon substrate was etched into two comb-shaped blocks that served as the cold and hot sides of thin-film-based legs, respectively. These blocks were thermally insulated from one another. A single 3 mm×3 mm μ-TEG exhibited an open-circuit output voltage of 146 mVK^{-1}. This design of lateral structure μ-TEG can pave the way for an almost easy assembly, and through system analysis, its performance can be enhanced further [88]. CMOS or MEMS technologies, however, are incompatible with practically all current high-performance TE materials. By utilizing common microfabrication methods based on photolithography and dry-etching processes, Ohkubo et al. concentrate on the construction of miniaturized TE devices based on contemporary TE materials. This study used microfabrication techniques to create an in-plane p-type TE device made of epitaxial p-type $Mg_2Sn_{0.8}Ge_{0.2}$ and n-type bismuth (Bi) layers. At a temperature differential of 110 K, the microfabricated device demonstrated a fairly high output voltage of 0.58 V and an output power of 0.6 μW, translating to an output power density of 21 $mWcm^{-2}$ [89].

Wearable wireless medical devices could be powered by thermal energy using application-tailored devices, such as those described by van Andel et al. [90] and Su et al. [91] to scavenge energy from the human body, for instance, a thermal/solar-hybrid powered electro-encephalogram (EEG) equipped with hybrid energy scavenger or an electrocardiogram (ECG) installed within a shirt. In addition, they have wrist TEGs that allow powering a variety of wireless sensors [92]. Their main business is making vertical and planar micromachined modules using poly-SiGe thermocouples (See Figure 2e). Bottom-up Si NW (nano wire) arrays must be monolithically integrated into the structures in order for this to happen, Dávila et al. have presented a "in-the-plane" or planar approach [93-95]. This research group has created TE microgenerators using multiple electrically connected dense arrays of silicon nanowires (Si NWs) integrated into microfabricated structures. Planar micro-thermoelements can produce temperature gradients naturally thanks to the fabrication and design of suspended silicon structures created by silicon micromachining. The exposed (111)-oriented vertical trenches were seeded with Au nanoparticles before the horizontal arrays of silicon nanowires were formed using the Vapour-Liquid-Solid (VLS) bottom-up method. Notable is the quasi-epitaxial attachment of Vapour-Liquid-Solid silicon nanowires to both silicon surfaces. Very low electric contact and heat resistances are so anticipated. By gradually connecting additional Si NW arrays, raising the thermoelement "height" to create larger temperature differences while maintaining the internal thermoelement resistances low, the thermal performance of this equipment as an energy harvester has been increased [96]. The developed thermoelements have generated power output densities of up to 1.44 $mWcm^{-2}$ for a ΔT of 300 °C and a power density of 9 μ Wcm^{-2} for a ΔT of 27 °C (across the nanowires) in a single thermoelement when serving as energy harvesters. Perez-Marn et al. have created ultrathin single-crystalline Si membranes with a thickness of 100 nm [97]. Having embedded p- and n-type doped areas that are electrically and thermally coupled in series as the driving force behind a μ-TEG (See Figure 2f). For a ΔT of 5.5 K, A 4.5 μWcm^{-2} output power density is possible with the proof-of-concept planar device.

Maksymuk et al. [98] employed the flash evaporation technique in order to make high-performance n- and p-type semiconductor Bi_2Te_3-based TE thin films. The TE properties of the designed TE films have significantly improved thanks to improved technological conditions for film preparation and subsequent annealing, which are ultramodern in comparison with bulk materials. Additionally, a novel sandwich-layered design for a flexible film thermoelectric micro-converter (FTEM) is given in this study by utilizing perforation cuts between the n- and p-legs and a flexible polyimide substrate (see Figure 2g). This unique design paves the way for preventing a rise in electrical resistance as a result of an increased number of elements in the micro-converter. The dimensionless effective figure of merit ZT 0.6 (includes substrate, conversion, and radiation losses, as well as parasite heat flux losses) and TE efficiency ∏max=3.4% were obtained for the flexible film thermoelectric micro-converter (FTEM) prototype at temperature difference of 100 Kelvin (T_c=300 K). As a result, the adoption of the flash evaporation technique makes it possible to manufacture massive, extremely effective film TE devices. Additionally, the usefulness of the flexible FTEM is demonstrated for a thermal detector that uses a high output voltage to identify a weak heat flux up to ~107 W. A more effective and fundamental technique would be to integrate TE elements alongside metal interconnects and transistor blocks at the circuit and device levels. A good instance of this scheme has been presented by Aktakka et al., in which low-temperature high-quality Sb_2Te_3 and Bi_2Te_3 thin-film TE instruments were integrated with SOI FinFETs in order to harvest the power of ∼0.7 µW from a ∼21◦C thermal gradient [99]. By embedding poly (3-hexylthiophene) (P3HT) and polyaniline (PANI) within an Au-doped carbon nanotubes (CNTs) matrix, a foldable TE device was created [100, 101] (Refer to Fig. 2h). The instrument displayed a power generation of 1.74µW and ZT=0.2 in a seven p-n junction module running at room temperature with a 20 Kelvin temperature differential. Even though such an achievement is promising, for practical usage, the maximum power density of 0.4 µW cm^{-2} is around two orders of magnitude too low. Carbon nanotube-based flexible TE has been approved by employing n-type Ag_2Te NPs . After the synthesis of the composite nanoparticle/ carbon nanotube, through thermal annealing at 400 °C, the thiolcapping ligands found on the sample surfaces were eliminated. The observed reduced electrical conductivity may be due to Ag_2Te's phase change from a monoclinic structure (phase) to a face-centered cubic (FCC, phase) one. Samples exhibited an electrical conductivity of 100–200 S cm^{-1}, total thermal conductivity as low as 0.7 $Wm^{-1}K^{-1}$, and a Seebeck coefficient within the 30 to 228 µV K^{-1} over the temperature range of 325–525 K [101]. Also, the n-type 800 nm Bi 2Te3/ (Pt, Au) multilayers featuring p-type Sb_2Te_3 legs developed by Yang Liu et al. [3] were employed for the fabrication of ultrathin MEMS TE devices (see Fig. 2i-l). For the annealed Bi_2Te_3/Pt multilayer, the power factor is 46.5 µW cm^{-1} K^{-2} at 303 K, which is an improvement of more than 350% over pure Bi_2Te_3 in terms of power factor. The measured power of the device featuring Bi_2Te_3/Pt and Sb_2Te_3 multilayers is 20.9 nW at 463 K, as opposed to the predicted maximum output power of 10.5 nW, which is 39.5% higher than the device fabricated based on Bi_2Te_3 and Sb_2Te_3. By employing new ultrathin MEMS TE devices and multilayer structures for a broad range of purposes, this study is capable of providing an opportunity to enhance TE characteristics.

It seems that improving nanoscale TE materials using quantum-dot superlattices in thick films, nanoscale inclusions in bulk materials, and phonon-blocking/electron-transmitting superlattices in thin films are the most effective strategies to get higher ZT in TE materials. Superlattices are being designed in a variety of systems via the electron transmission/phonon-blocking concept for different temperature regimes in order to make power harvesting or thermal management possible at those respective temperatures. While Bi_2Te_3 based superlattices are useful below a temperature of 175°C,

PbTe/PbTeSe superlattices and PbTe-QD(quantum-dot) superlattices are useful within the 175-300°C range. ErAs: InGaAs/InGaAlAs quantum-dot superlattices and Si/Ge superlattices may present improved ZT in comparison with the bulk materials within the 300-500°C range [102]. If the electric transport occurs along the thickness of the film, which is across the superlattice interfaces, the quantum-dot superlattices and thin-film TE superlattices can be easily engineered into useful devices. Planar semiconductor device technology is applicable in these circumstances and can be used with conventional microelectronic equipment. The parts that follow will go through the superlattice TE technologies used in the Bi_2Te_3 material system. Venkatasubramanian [102] discusses the most recent developments in these materials and focuses on how these materials can be used to create device prototypes for microscale energy harvesting and active thermal management of high heat flux. The heated regions appear to be amenable to cooling (with flux levels > 1000 Wcm^{-2}) in high-power electronics as well as the entire solid-state micro-cooling down to 207 K. Through metallorganic chemical vapor deposition (MOCKS), the nanoscale superlattices are grown (see Figure 2m). A 4x4 array of p-n couplings using thin-film superlattice materials is demonstrated in Fig. 2n. The dimensions of the array are approximately 2.5 mm x 2.5 mm x 0.3 mm. In the case of applying an external ΔT of nearly 200 K across both ends of the 0.3 mm thick module, such modules have led to the generation of 1 W of electric power. This represents a specific power of about 100 Wgm^{-1}, an areal power density of 16 Wcm^{-2}, and a volumetric power density of over 50 Wcm^{-3}.

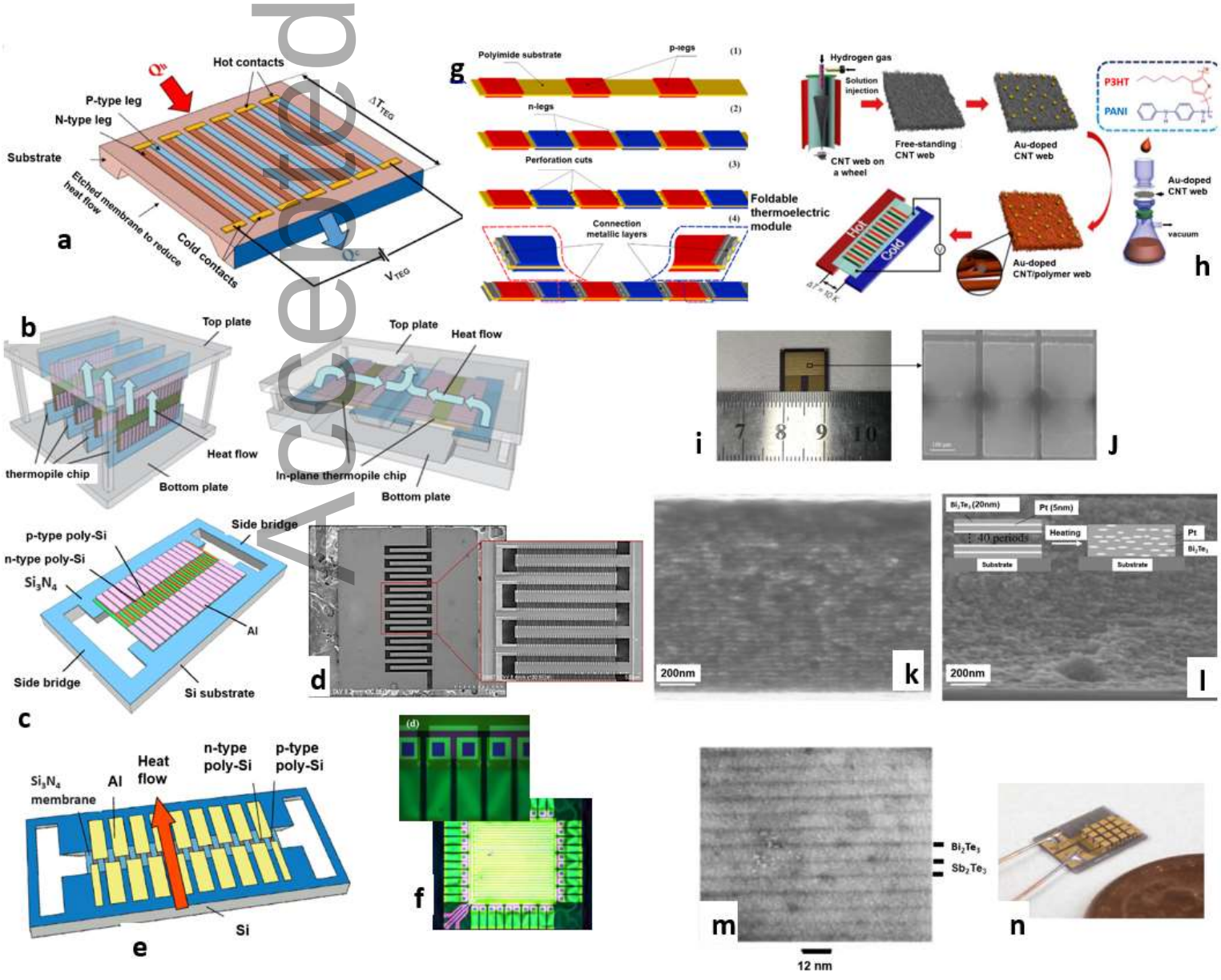

Fig. 2. (a) Schematic view of a typical vertical μ-TEG [43]. (b) Two potential methods of in-plane thermopile assembly [85] (c) Bulk-micromachined membraneless in-plane thermopile overview schematic;(d) images from SEM of the suggested lateral structure TEG. [87]. IMEC research center-developed micromachined thermoelectric energy harvesters. (e) Micromachined in-plane bulk thermopiles without a membrane for energy harvesting [92]. (f) Optical microscope images the n- and p-regions of the fabricated device [97]. (g) A schematic showing the primary steps in the creation of the flexible FTEM. FTEM ¼ film thermoelectric micro-converter [98]. (h) Schematic of the Manufacturing Process and Geometry of the Thermoelectric Module [101]. (i) Image of a real, manufactured MEMS device; (j) SEM view of the MEMS device's local structure (k) SEM cross-sectional picture of the supporting structure's cross-plane; (l) Cross-section of a single thermoelectric leg as seen through a scanning electron microscope [3]. (m) TEM image of a 10 Bi_2Te_3 /50 Sb_2Te_3 superlattice grown by MOCVD (n) 16 p-n couples are used to create a 4x4 module array [102].

2.3- Hybrid structure

Figure 3a shows a µ-TEG with lateral current flow and vertical heat flow [43]. The performance of a hybrid-structure µ-TEG is a compromise between those of the other two µ-TEG types; however, it also integrates their benefits. In a hybrid-structure µ-TEG, one side of the chip's surface is vertically pumped with heat from the surrounding area, it subsequently leaves from a different side vertically after being transported through the thermopile in a planar orientation. Since the heat flux flows in the vertical direction on the two sides, it enables the fabrication of a µ-TEG with a traditional package-like vertical structure. As a result, a hybrid-structure µ-TEG is favorable when its performance fulfills special purposes. In order to enhance the output power of hybrid-structure µ-TEGs, the key element to design is the heat flux path optimization [4]. To improve thermal coupling between the ambient and µ-TEG, the most successful approaches initially involve covering a metal layer on the thermopile's cold/hot side., changing the distribution and shape of the thermopile, and inserting a cavity above/under the thermopile. The construction of lateral and hybrid µ-TEGs primarily uses techniques like IC technology and MEMS, nanoscale technology and MEMS, and thin-film technology and MEMS. Particularly, nanoscale technology and MEMS employ high ZT nanoscale materials with evident performance enhancement and a future outlook for their applications [103]. M. Strasser et al. were the first to describe a hybrid µ-TEG based on poly-SiGe and poly-Si surface micromachining [104]. Figure 3b depicts a schematic depiction of the two TE pairs used in the Bi-COMS implementation. By discarding the oxide barrier, the direction of heat flux within the µ-TEGs was optimized. An air-filled cavity is available under this barrier for extra thermal isolation. The results of their subsequent research [105] showed that the fabrication of µ-TEGs by etching cavities into silicon substrates produced an electric power output of 1 W and a voltage of 5 V for a matched consumer with the generator of 1 cm^2 at a temperature decrease of approximately 5 K.

Z. Wang et al., from IMEC unveiled a fully functional wearable µ-TEG designed specifically for use on the human body [106]. Figure 3c illustrates a photograph of a µ-TEGs and a schematic design of a micromachined poly-SiGe thermocouple. This design maximized the thermal resistance of the thermocouple's microstructure by meeting a number of criteria. First, a 2.5 mm deep trench was dug out from under the cold junction. Second, a step with a height of 0.5 mm was added over the trench. Thirdly, the junction area's width remained relatively large to reduce contact resistance while the thermocouple leg width was tapered to the technological threshold. In addition, by deep reactive-ion etching (DRIE) of Si, a rim structure was created. The µ-TEG's

estimated output power and open-circuit output voltage on a matched external load were, respectively, 0.026 $\mu Wcm^{-2}K^{-2}$ and 12.5 $Vcm^{-2}K^{-1}$. When worn on the human body, the wearable TEG delivered an approximate output power of 0.3 nW and an approximate open-circuit output voltage of 0.15 V on a matched external load. An innovative MEMS TE generator design and manufacturing process with high-temperature efficiency was described by T. Huesgen et al. [107]. The μ-TEG is shown schematically in Figure 3d with an improved heat flow channel. Using a backside DRIE procedure via the substrate, the thermal insulation of the hot junction from the substrate was completed. In order to prevent cavity contamination and realize an appropriate thermal contact, a second wafer was attached to the rear end. Using the thermopiles fabricated from n-poly-Si and Al or n-$Bi_{0.87}Sb_{0.13}$ and p-$Bi_{0.5}Sb_{1.5}Te_3$, power factors of $8.14 \times 10^{-3} \mu Wmm^{-2}K^{-2}$ and $3.63 \times 10^{-3} \mu Wmm^{-2}K^{-2}$ are attainable, respectively. This investigation presents a new method to manufacture a TEG on the basis of thin-film technology. One can divide the fabrication procedure into three modules, the first of which is associated with the TE structure, deposited in thin-film technology. The second and third modules deal with the heat conductive structures needed to provide a strong gradient of in-plane temperature when the heat flux moves perpendicularly (cross-plane) across the device. In this method, a high integration density of thermocouples is concurrently achieved while the thermal contact surfaces are optimized.

Yang et al., [108] designed a TE energy harvester through a standard CMOS procedure presented in Figure 3e. A thermal isolation cavity was created beneath the thermocouples to preserve the temperature gradient, improve output power, and stop heat loss. The optimized μ-TEG can reach a voltage factor ($Ø_u = U_0/(A\,\Delta T)$, where U_0 is an open-circuit voltage and A is area) of 2.788 $Vcm^{-2}K^{-1}$ and the maximum performance factor of 0.0473 $\mu Wcm^{-2}K^{-2}$. Their follow-up study [109] adopted stacked polysilicon thermocouples in a μ-TEGs with the maximum voltage factor of 3.952 $Vcm^{-2}K^{-1}$ and the maximum performance factor of 0.0473 $\mu Wcm^{-2}K^{-2}$. Next, a thermocouple resembling a quantum well was used in 2011 [110], with a voltage factor of 0.241 $Vcm^{-2}K^{-1}$ and a maximum performance factor of 0.241 $\mu Wcm^{-2}K^{-2}$. CMOS and post-CMOS micro-TE power generators made of 24 thermocouples connected in series and built from p- and n-type polysilicon strips were shown by J. Kao et al. A silicon dioxide layer is used to insulate the cold part from the heat source. In order to increase the hot part's heat-receiving surface, the thermocouples are fastened to an aluminum plate [4]. Figure 3f shows the SEM photograph and schematic overview of the suggested TPG. To achieve a significant temperature difference between the two thermocouple junctions, heat is transported over the device from its bottom to top side. The output voltage was 67 V for a 1 Kelvin temperature differential between the two sides. A silicon-based monolithic planar μ-TEG through bonding technique was proposed by Ziouche et al. [111]. The air cavities of the thermopile on top of the cold junctions and below the hot junctions in both Si wafers were made using the back-side DRIE. The oxidized porous-Si functioned as a temporary support to shield the multilayer membranes from the forces applied during the bonding procedure. The maximum output power of a μ-TEGs with five membranes was 12.3 μWcm^{-2} for a 2 Wcm^{-2} input heat.

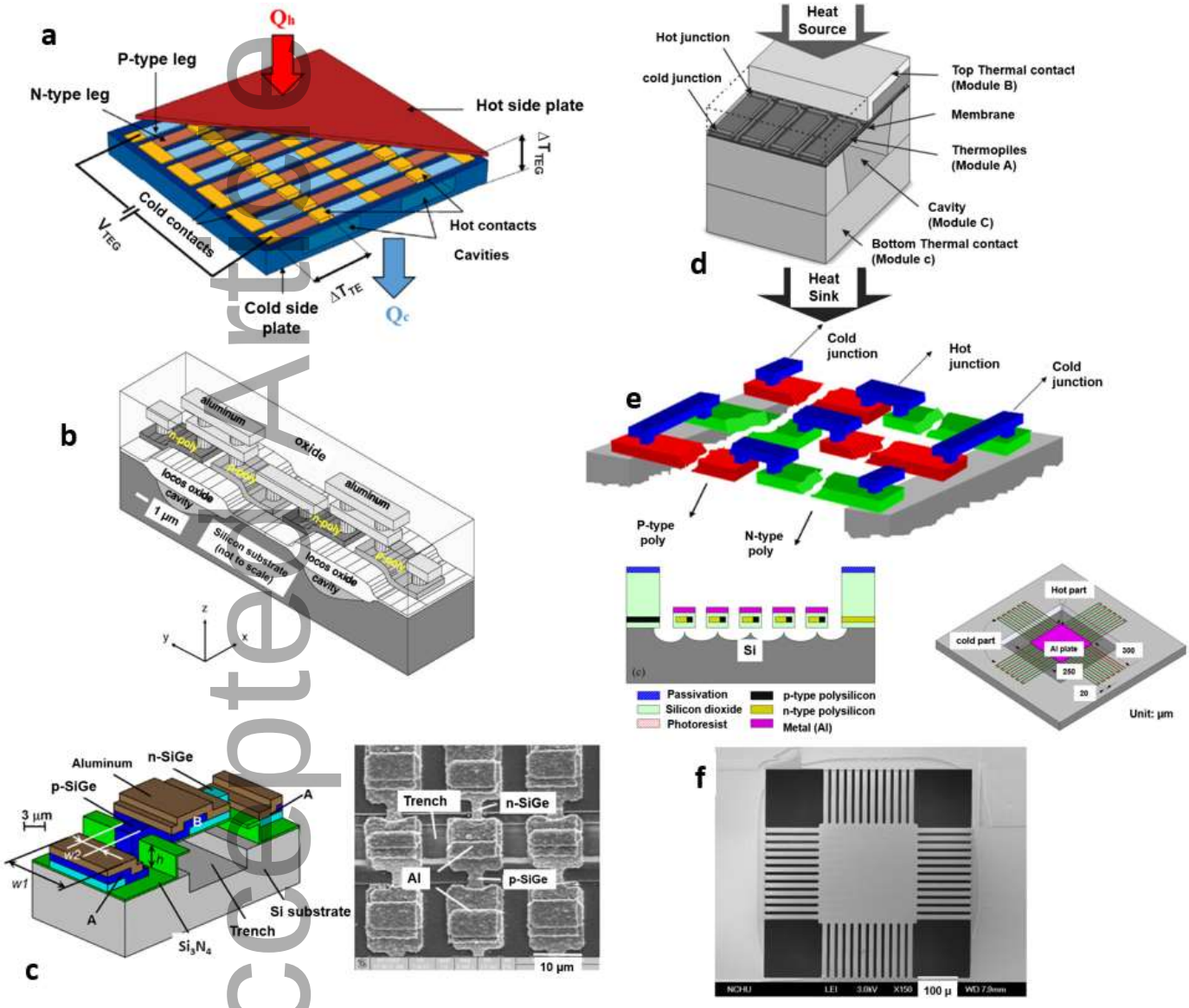

Fig. 3. (a) Schematic overview of hybrid structure µ-TEG reprinted with permission from [71]. (b) Diagram of the two thermoelectric couples used in the Bi-COMS implementation [104]. (c) Full-fledged wearable -TEG apps designed exclusively for use on the human body [106]. (d) The schematic for the µ-TEG shows an optimized heat flow path [107]. (e) A thermoelectric energy harvester employing the widely used CMOS technology has a thermal isolation cavity underneath the thermocouples [108]. (f) Schematic and microscopic view of the proposed TPG [4].

3- Optimization of micro thermoelectric structure and geometry

Optimization of TE structure and geometry is a crucial research field that has been scrutinized recently due to noticeable improvements realized in structural integrity and performance. As a matter of fact, special emphasis is placed on the mechanical and electrical performance improvements that can be obtained through the optimization of TE structure and geometry. The

four major parameters, i.e., cross-sectional area, leg height or length, leg shape (asymmetrical, hollow, and traditional rectangular geometries), and the number of legs, which are considered during optimization of the TE geometry, are thoroughly explored [112]. This optimization was carried out on a number of TE structures, including annular, flat plate, concentric, flexible, segmented, and micro coolers and μ-TEGs (in accordance with the heat sink shape and heat source), however, design and optimizing methodologies for vertical μ -TEGs will be investigated since their output power and efficiency are higher than other types and critical to the architecture. Additionally, the constant temperature difference (CTD) condition is typically used for conventional TE device design. However, in practical applications, the constant heat flux (CHF) condition predominates [113]. As a result, the methods for optimizing the geometry and structure, such as multi-objective optimization and 3D finite optimization, are thoroughly examined, and the most striking findings from the literature review are presented:

3.1. 3D finite optimization

Through 3D modeling, which also presents an improved perception of the heat transfer process and temperature distribution in systems and thus improves performance predictions, a more precise simulation is attainable [114]. Using the numerical model of the 3D finite difference method (FDM), finite element method (FEM), and finite volume method (FVM), 3D computational fluid dynamics (CFD), the temperature, voltage, geometric parameters, and stress distributions were optimized for a TEG device. The software tools used to conduct the numerical study were ABAQUS, COMSOL Multiphysics, and ANSYS.

3.2. Multi-objective optimization

Multi-objective optimization refers to the optimization procedure simultaneously applied to two or more inconsistent objective functions under constraints [115]. As several TE geometries must be optimized at the same time in order to obtain optimal performance, multi-objective optimization techniques have recently attracted much attention for optimization of the TE geometry. Since the 3D finite optimization technique is time-consuming and may not be capable of considering the entire set of potential variables at the same time, multi-objective optimization techniques present the most efficient and best results for optimization of TE geometry. Genetic algorithm (GA), improved Powell algorithm, NSGA-II, simulated annealing, and particle swarm optimization (PSO) algorithm have optimized the TE generator geometry to improve its output power and efficiency. Volume, material type, leg length size and shape factor, temperature, and the shape of installation position were included in the optimization process. The output power, efficiency, and reliability objective functions were optimized.

3.3. Combined optimization

With the FVM, FEM, and the 3D FDM, multi-objective optimisation has been used to fine-tune the TE geometry for better performance and reliability. Jang et al., [116] combined the simplified conjugate-gradient method (SCGM) and the 3D finite difference method to find the best thickness and spacing for the spreaders of the TE (see Figure 4).

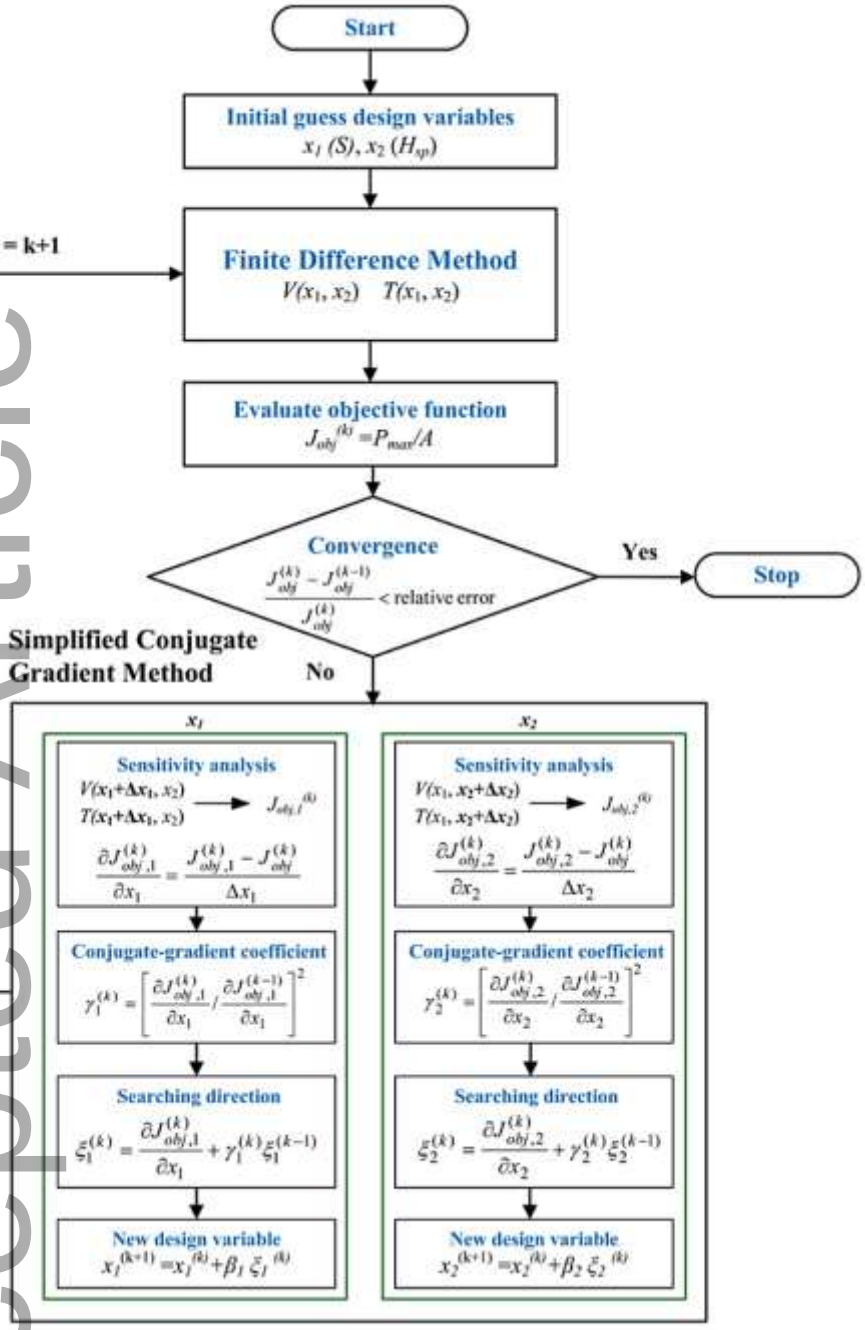

Fig. 4. The flowchart of FDM and SCGM optimization techniques [116].

The authors suggested using multi-objective optimization methods, such as the Taguchi method, simplified conjugate-gradient method (SCGM), NSGA-II, and GA, to concurrently increase output power and efficiency while lowering mechanical stress. Software packages, such as MATLAB and COMSOL, were employed to solve the multi-objective optimization algorithm and three-dimensional model, respectively.

3.1 Leg height or length

To increase the reliability and efficiency of the TE generator and cooler, it is important to adjust the leg height or length. Tanwar et al. [117] employed n-type copper telluride (CuTe) and electroplated p-type bismuth antimony telluride (BiSbTe) materials in their investigation. They used the FEM with COMSOL Multiphysics to optimize and assess how the leg structure and shape affected the

maximum efficiency and electrical power production of the μ-TEG. Leg height has a considerable impact on device manufacture and has a direct impact on the thermal conductance and electrical resistance of devices. To calculate the ideal height of the device, the height of micropillars varied between 1 and 50 μm and underwent a 5 K temperature gradient. The μ-TEG's overall electrical resistance and output power grew as the height of the pillars climbed. Fig. 5a illustrates the contribution of increased pillar height on the thermal conductance, output voltage, and electrical resistance. As the leg height is extended, the voltage across the leg pairs first increases steadily. Once the leg height reaches 10 μm, the voltage begins to stabilize. To maintain a consistent temperature gradient and a low electrical resistance simultaneously, a μ-TEG needs to attain a low thermal conductance. Fig. 5b presents the generated output power using a variety of pillar heights. At a height of 3 μm, the maximum output power of 3.96 μW was attained. As a result, it seems that with a pillar height of 10 μm without having to drastically reduce the device's output power, their described material properties are suitable for the intended human body applications. In their study, Kumar et al. [118] optimized TE components to recover waste heat in automobiles by employing the numerical model presented by Hogan and Shih [119]. Skutterudite TE material was utilized, and a uniform ΔT = 250℃ is considered across TE cold and hot side junctions. According to the authors, it is possible to get the highest power output while using less material by carefully choosing the fill fraction and leg height.

In addition, a detailed parametric optimization was carried out by Tian et al. [120] for a segmented thermoelectric generator (STEG) to recover energy from exhaust waste heat of diesel engines. Particularly for applications involving high heat source temperatures, the authors recommended employing a segmented thermoelectric generator (STEG) rather than a traditional TEG. The results also showed a link between the maximum power output and efficiency of the TEG and the length of the TE leg, as shown in Figures 5c and 5d, respectively. Zhang et al., [121] improved a STEG's leg length ratio in order to increase efficiency and output power. They employed the numerical model presented by Jiao et al. [122]. The user-defined functions (UDFs) for formulation of the numerical model were added to the FLUENT commercial software suite. They discovered various ideal leg length ratios for maximizing output power and efficiency (see Figure 5e). Also, they discovered that the best TE leg length ratio is decided in accordance with the TE material characteristics, conditions, and geometry for heat transfer. Ma et al. [123] recently conducted a comprehensive study on segmented TEG' leg length ratio optimization in order to recover energy from engine exhaust heat. This investigation introduced the numerical model into the FLUENT software package. Using a numerical model, the segmented TEG was optimized at both system and component levels. Five distinct situations were examined in terms of the ratios of the two components in each. While the first two cases were non-segmented traditional TEG, the remaining three cases served as STEGs featuring a variety of leg length ratios. Figure 5f illustrates the highest output power along with various lengths. In general, the optimum leg lengths differ for each TEG model, and it reaches the best performance in Case 4. When the length is lower than its optimum value, the output power declines rapidly. This is attributable to the stronger impact of contact resistance. It seems that STEGs are of higher capability in the optimization of structure based on similar output power requirements.

Shen et al. [124] investigated the performance (efficiency and power output) of an annular TEG using a constant heat flux and a FEM. Additionally, the relationship between TE materials and temperature was covered, and the effect of the shape parameter (Sr) on the annular thermoelectric generator (ATEG)'s output power was examined. They witnessed that as TE leg length increased,

the power output also increased (Figure 5g). Nonetheless, under constant temperature conditions, a reverse trend was detected. Shen et al. also conducted a theoretical analysis of a segmented annular thermoelectric generator (SATEG) and comparison with an ATEG [125]. They found that the SATEG's efficiency grew initially until it reached a maximum value, after which it decreased. Shittu et al. [126] studied the electrical and mechanical performances of a SATEG by employing a FEM technique and compared them with those of an ATEG. They witnessed that the performance of the SATEG surpassed that of the ATEG. Additionally, as shown by the data, the TEG's electrical performance declined as leg length increased. This study analyzes the numerical simulation of a SATEG by employing a 3D finite element analysis. Using the COMSOL 5.3 Multiphysics program, the effects of leg angle and TE leg length on the mechanical and electrical performances of segmented and non-segmented ATEGs were investigated. The geometries of segmented/non-segmented ATEGs are presented in Figure 5h, i, which are constituted of copper, alumina ceramics, TE legs, and the welding layer. According to Figure 5j-m, when the temperature difference exceeds 100 K, the efficiency of a SATEG surpasses that of an ATEG with Bismuth telluride material. The electrical performance is significantly impacted by the TE leg length, and it is well known that shorter TE leg lengths result in greater electrical performance than longer TE leg lengths. Eventually, the results (see Figure 5n) indicate that increased TE leg length can decrease the electrical performance and thermal stress of the segmented/non-segmented TEGs. For both the ATEG and SATEG, when the leg length is lengthy (L = 5), the von Mises stress is at its lowest.

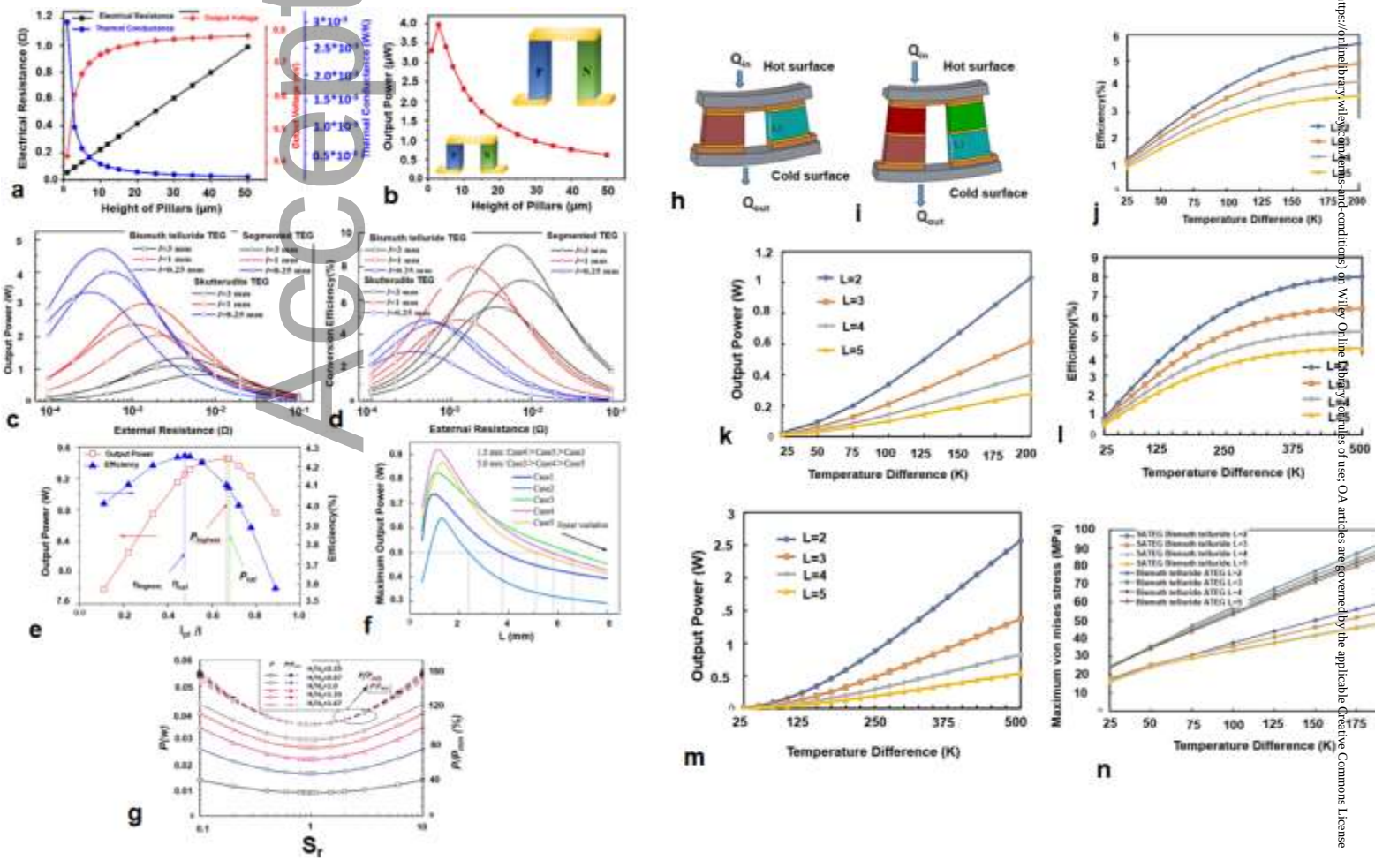

Fig. 5. a) Electrical resistance, the thermal conductance and output voltage b) power output against leg height at 5K temperature gradient [117]. Effect of leg length on (c) output power and (d) a comparison of three thermoelectric generators' efficiency [120]. (e) Thermal boundary condition at constant surface temperature, output power, and thermoelectric conversion efficiency of segmented TEGs with various length ratios (the length of the p1-type divided by the total length).(T1 = 580 K; T4 = 500 K) [121]. (f) Maximum output power with length in all cases [122]. (g) Variations of P and P/P_{min} with Sr under different H/H_0 [123]. The schematic geometry of h) ATEG i) SATEG. Different leg lengths with (j) Efficiency and (k) Output power of Bismuth telluride ATEG and (l) Efficiency and (m) Output power of SATEG when θ1 = 3, θ2 = 3, and RL = 0.001 Ω. (n) Effect of the thermoelectric leg length of bismuth telluride in SATEG and ATEG when θ1 = 6 and θ2 = 2 [126].

By employing the GA with constraints and metaheuristic optimization techniques, Yusuf et al. [127] tried to determine the optimal geometric parameters of a TEG. They improved the maximum power output and energy conversion efficiency for Skutterudites TE materials operating at a maximum temperature differential of 500 K. Fig. 6a depicts the concerned flowchart. The best energy conversion efficiency or the highest power output are often the two goals of GA optimization. This is because they cannot reach their maximum values simultaneously. As Fig. 6b depicts, as the length of the thermo-element lengthens, the power output decreases, whereas the efficiency of energy conversion increases until reaching a maximum point at the optimal thermo-element length. Fig. 6b is simply interpreted as follows. The thermo-element length should be roughly 0.5 mm if an effort is made to create power outputs of about 80 W. However, given the corresponding energy conversion efficiency of about 4.4%, the TE module must be capable of absorbing a heat input of 1818 W, and given the current performance of the TE materials, this is impossible. But, when the module is functioning at its ideal length, it only needs to absorb about 300 W of heat in order to produce 30 W of power. As a result, this is both economically wise and practicable to use the module at the optimal geometry, which is an objective of this investigation.

The use of artificial neural network (ANN), a deep learning technique, in forward modeling the maximum efficiency and power generation of a TEG and its use in the generator optimization and design, was demonstrated by Zhu et al. [128]. After training by employing a dataset containing 5000 3D FEM-based simulations (through COMSOL Multiphysics® software), the ANNs with five layers and 400 neurons in each layer indicate a very high prediction accuracy (>98%) and can function both when there is a steady heat flux and when there is a temperature differential while taking the surficial heat transfer into account, contact electrical resistance, and other TE effects (Figure 6c). Investigating the effectiveness of the TEG in relation to changing geometrical characteristics, including the height of the TEG leg (HTE), the filling factor (FF), the widths of the p-type and n-type legs (W_p and W_n), and the height of the connection (HIC). Combined with the genetic algorithm, the trained ANNs can optimize the leg width, leg height, interconnect height, and fill factor of the TEG for various contact resistance and operating conditions. The TE materials employed in this investigation are p-type $Bi_{0.5}Sb_{1.5}Te_3$ and n-type $Bi_2Te_{2.7}Se_{0.3}$ for the legs, respectively. The cold-side temperature (T_C) is set to 300 Kelvin as the constant value for the thermal boundary conditions. Figure 6d illustrates the optimization flowchart. In Figure 6e, f, the dashed lines indicate the η and PD_{max}(maximum power density) values predicted by the artificial neural network as a function of filling factor and H_{TE}, whereas the values of W_n, W_p, and HIC were fixed at 2.5 mm, 2.5 mm, and 1.5 mm, respectively. As soon as the network training and verification are completed, it is applicable for optimization of the design. Figures 6g, i depict the GA convergence curves for efficiency and

power optimizations, respectively. After ca. 100 generations, both procedures show a good convergence. While a maximum power density of 70 $mWcm^{-2}$ was obtained (see Figure 6g), the maximum efficiency was 3.2% (Figure 16i). For a constant T_h of 400 K, the optimized H_{TE} will be 1.3 mm to obtain the highest PD_{max}. As shown in Figure 6h, this is authorized by increasing its value from 0.5 mm to 5 mm and assessing the TEG performance using simulation and an ANN. From another viewpoint, the maximum efficiency η necessitates the optimized H_{TE} to achieve the predetermined range's upper limit (5 mm) (Figure 6j). Both the simulation's (blue dots by COMSOL) and ANN's (black lines) outcomes are very consistent with one another.

In both power generation and heating/cooling purposes, the temperature difference in TE legs leads to thermal stress because different materials show different thermal expansions. As a result, conducting thermal stress optimization and analysis is important in order to get informed about the high-stress locations in the legs. The primary goal of the study of thermal stress optimization is to significantly reduce the thermal stress on TE legs, which will lengthen the device's useful life. The largest observed stress of the legs occurred in the module corners, which had a longer distance from the center, according to Turenne et al analysis's of the stress level in a TE module [129]. Under steady-state conditions, the numerical study was completed using finite element analysis. The impact of geometrical features on the thermal stress of TEG was also studied by Gao et al. [130]. As the length of the TE leg grew, they discovered that the von Mises stress and shear stress were initially decreased. The ANSYS simulation software was utilized to carry out the numerical study along with the finite element analysis, and the stress analysis was completed on the assumption that the materials had anisotropic mechanical properties.

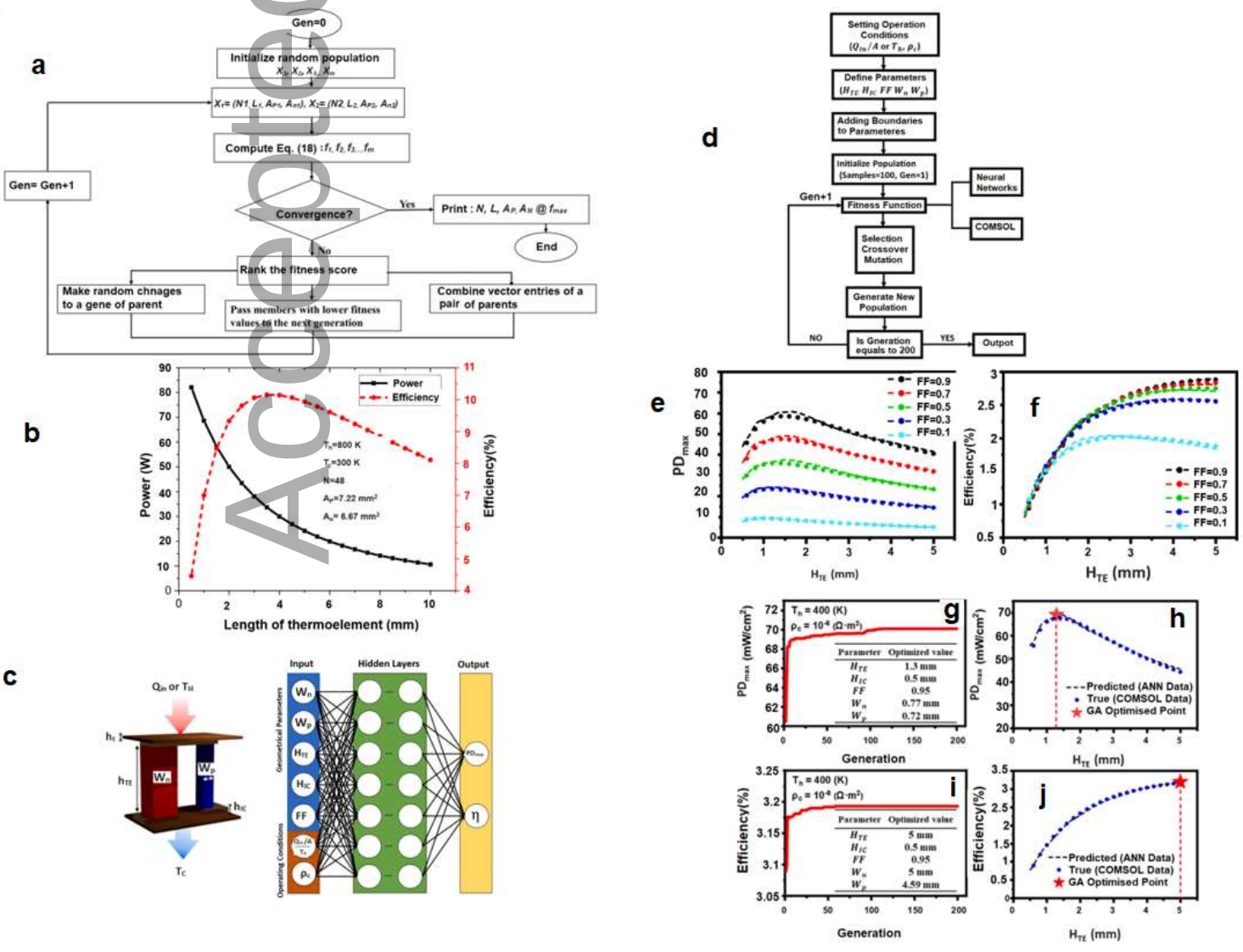

Fig. 6. a) Flowchart of the genetic algorithm. b) Effect of thermo-element length variation on power production and conversion effeciency [127]. c) The design of the forward modeling neural network used to forecast the TEG model's power performance . (d) Process flow diagram for the genetic algorithm. For the purpose of calculating fitness functions, both COMSOL simulation and neural networks have been used separately (e) PD_{max} and (f) efficiency η obtained from ANN (dashed lines) and COMSOL simulation (dots) as a function of HTE and FF. The operating condition chosen is Th of 400 K and ρC of 10^{-8} Ω· m^2. The H_{IC}, W_n and W_p values were fixed at 1.5 mm, 2.5 mm and 2.5 mm, respectively g) Convergence curve of genetic algorithm for (h) PD_{max} and (b) η (i, j) Comparison of PD_{max} and efficiency as a function of H_{TE} from ANN and COMSOL simulation [128].

3.2 Leg cross-sectional area

Another important characteristic that can be optimized to raise the TEG and cooler's performance is the cross-sectional area of the legs. It is recommended to use the output power per area and power density to estimate the TEG performance instead of efficiency and output power. The experimental analysis of the impact of the TE leg area on module performance was the focus of Cheng et al. [131]'s work on the structural optimization of TE modules. A polycrystalline bismuth telluride TE material was used. According to their findings, the highest power production is attained at an ideal leg cross-sectional area (Figure7a). The ideal TE leg area for a TEG's improved power production was identified by Fan et al. [132]. They concluded that while the TE conversion efficiency was nearly constant at constant surface temperature boundary conditions (case 4), it was inversely proportional to the cross-sectional area of the leg at constant heat transfer coefficient boundary conditions (cases 5 and 6) (Refer to Figure 7b). He et al. [133] created a thorough one-dimensional model to improve the TEG module geometry based on the Hill-climbing technique to increase power output. Numerical simulations were carried out in MATLAB, which were then validated in the COMSOL software package. As shown in Figure 7d, the maximum power output always rises as the leg area rises for any given leg length.

When Cui et al. [134] looked into the possibility of a porous ATEG for using waste heat, they found that it performed better than a bulk TEG. They came to the conclusion that, as the cross-sectional area is optimized, the maximum power output grows to a peak value and subsequently drops, as illustrated in Figure 7e. Understanding how the area ratio of the thermoelements affects power output, Yusuf et al. [127] employed the GA. In Fig. 7f, the n-type thermoelement area varies, whereas the other parameters retain their optimal values. As the A_n/A_p ratio is increased from 0 to approximately 3, the power output is constantly increased, whereas the efficiency of energy conversion is increased until reaching a maximum point, which is then decreased regularly. The optimal ratio of the regions as determined by GA corresponds to the location where energy conversion is most efficient.

By employing the A_p/A_n ratio of a μ-TEG, Tanwar et al. [117] used COMSOL Multiphysics to optimize the device's performance. The n-type leg's cross-sectional area was kept constant while the p-type leg's area changed. After modeling a number of different A_p/A_n ratio combinations ranging between 0.5 and 4, the results were plotted in Figs. 7g and h. The electrical resistance of the p-type leg decreased as the cross-sectional area increased, but the device's thermal conductivity increased

(Fig. 7g). The power of the single-leg pair TEG gradually rose as the A_p/A_n ratio grew (see Fig. 7h), and the output power increased from 1.1 to 4.78 µW; however, the efficiency experienced a decline of 17.5%. As a result, the cross-sectional area of the legs must be balanced to deliver a high output of power and optimum efficiency. In order to optimize the µ-TEG device featuring many pillars, two devices with various A_p/A_n ratios were considered, which are shown in Fig. 7i. The device featuring a constant footprint of 3.5×4.5 mm^2 was composed of 240 TE leg pairs with A_p/A_n = 2 and 312 TE leg pairs with A_p/A_n = 1. As Fig. 7j indicates, the output power of both devices was plotted versus varying load resistances at the 5 Kelvin temperature gradient. For the individual device, the maximum output power occurred at R_L= R_{TEG}. Additionally, as shown in Fig. 7k, estimates of both ratios' contributions to the device's output power were made at a variety of temperature gradients between 2 and 10 K. At low-temperature gradients, both ratios resulted in the same power outputs. Nonetheless, an A_p/A_n ratio of 2 at higher temperature gradients across the device resulted in higher power outputs in comparison with A_p/A_n = 1, despite the fact that the device with the higher ratio had fewer TE couples. This is explained by the fact that the device's overall resistance lowers when the p-type TE leg's cross-sectional area increases, even though it has poorer electrical conductivity than n-type material.

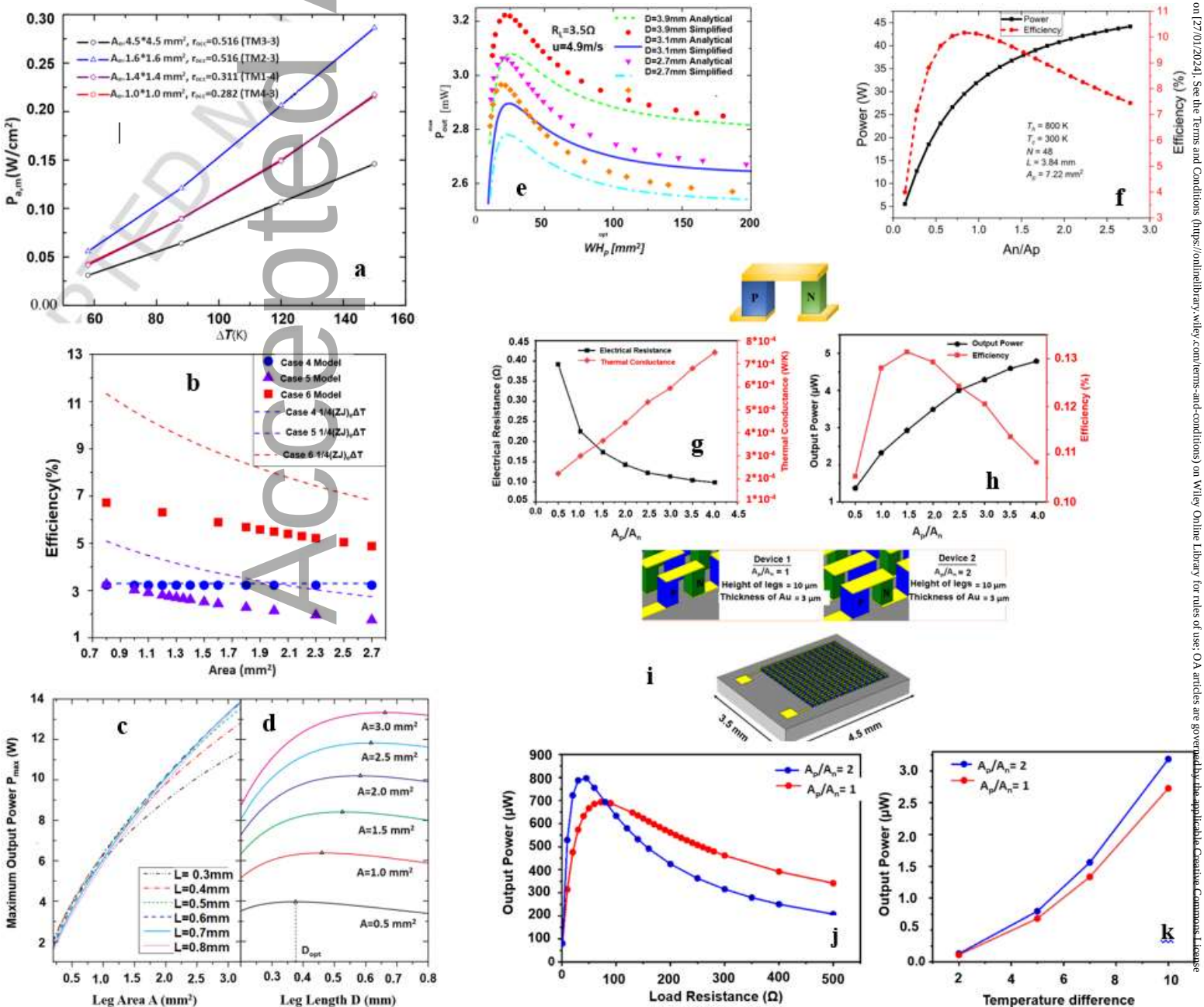

Fig. 7. a) Maximum output power and various temperature variations under various thermoelement cross sections [131]. b) Variation in conversion efficiency due to leg cross-sectional areas [132] The maximum output power P_{max} versus TE leg area (c) at different leg lengths D and that in comparison to TE leg length (d) at various leg areas A [133]. (e) Distribution of maximum power production in relation to the cross section's ideal size [133]. (f) Impact of thermoelement area variation on power production and conversion efficiency [117]. g) A_p/A_n ratio as a function of electrical resistance and thermal conductivity of a single-leg pair; (h) power production and single-leg pair's effectiveness for various A_p/A_n ratio. (i) Schematic of an improved device. (j) For devices with A_p/A_n ratios of 1 and 2, output power is shown against load resistance at a temperature gradient of 5 K. (k) Power output for devices with an A_p/A_n ratio of 1 and 2 at various temperature gradients [117].

3.3 Thermoelectric leg shape

When optimizing the performance of a device, the reliability, performance, and reduction in fabrication complexity of the device are significantly influenced by the leg shape. Although the traditional TE legs are symmetrical/rectangular, hollow shapes, complex geometries, and asymmetrical TE legs are under study in recent years as a technique for enhancing the heat transfer in the legs and TE reliability and performance. By using asymmetrical legs, TE legs can have a greater temperature gradient. This can be attributed to the TEG's overall lower thermal conductivity. In addition, the asymmetrical TE legs generally feature variable cross-sectional areas, leading to a trapezoidal shape. Lamba et al. [135] looked into how TE geometry configuration affected TEG performance (presented in Figure 8a, b). They concluded that the energy and exergy efficiencies of a trapezoid-shaped TEG were increased by 2.32 percent and 2.31 percent, respectively. Additionally, they discovered that the point at which the maximum energy and exergy efficiencies were recorded differed from the point at which the maximum output power was witnessed. An experimental and numerical investigation on TEGs featuring asymmetrical legs was carried out by Fabián-Mijangos [136]. The superiority of the asymmetrical legs over the symmetrical ones has been demonstrated in Figures c–f. The application of asymmetrical TE legs to enhance performance was demonstrated experimentally for the first time in this study. Shittu et al. [137] also gave a thorough analyzing a TEG numerically with asymmetrical and segmented legs under steady-state and transient conditions using the COMSOL 5.3 Multiphysics software, which is shown in Figure 8g-i. They evaluated the new TEG design against a non-segmented TEG and optimized it to boost electrical performance. Their results approved the greater performance of the optimized asymmetrical and segmented design compared to the conventional TEG.

Tanwar et al. [117] used the FEM to simulate three different kinds of pillar shapes (hexagonal, circular, and square) in order to get the most power out of a μ-TEG, as shown in Fig. 8j. The cross-sectional size of the pillars has no effect on the output power acquired for the device when subjected to a fixed temperature gradient since each leg pair has the same electrical resistance, as illustrated in Fig. 8k. For a single-TEG leg pair with a variety of shapes, the power output was estimated when undergoing a 5 Kelvin temperature gradient, and the acquired corresponding power outputs are illustrated in Fig. 8l for varied load resistances. When the matching internal resistance of the leg pairs was equal to the applied load resistance (RTEG = RL), the highest output power was realized for a single leg pair with a varied cross-sectional shape. The square-shaped pillar in Fig. 8l had the highest output power of 2.32 mW, which was 7.41% and 18.37% greater than the hexagonal- and circular-shaped pillars, respectively. On the basis of the first and second laws of thermodynamics, an exoreversible trapezoidal thermoelectric heat pump (TTEHP) was the subject of a TE model created by Lamba et al. [138] that took into consideration the Thomson effect as well as the leg geometry's impact on the heating load and coefficient of performance of the apparatus.

For the investigation of the operational and geometry parameters' effects on the heating load and thermoelectric heat pump's performance coefficient, including the shape parameter (A_c/A_h) (R_A), the MATLAB Simulink environment was used. Using the GA, the optimal parameters concerning the maximum heating load and the maximum energy efficiency were decided. Fig. 8m depicts the schematic view of a thermoelectric heat pump made up of trapezoidal-shaped TE legs sandwiched between the heat sink and heat source, as opposed to a flat-plate thermoelectric heat pump, which has a constant area. The cold junction's temperature is fixed at 300 K ambient temperature, whereas the hot junction's temperature ranges from 305 to 370 K. The dimensionless heating load is initially increased as the shape parameter (R_A) increases until reaching its maximum value at R_A =1. Then, it declines with further increases in the shape parameter (see Figure 8n). At R_A = 1, the internal resistance of the device is at its minimum value, leading to the creation of the maximum current flow and, as a result, the maximum input power. The device's internal resistance rises for both higher and lower R_A levels, resulting in decreased heating load and input power.

Using a FEM analysis conducted within the COMSOL Multiphysics software, Thimont et al. [139] carried out an investigation on the effect of the geometry of an individual leg on thermal resistance. Four basic leg geometries, i.e., square, triangular, trapezoidal, and circular, were examined with respect to their nominal shapes, which will be referred to as three geometrical variations: hollow, layered, and filled. These leg geometrical variations are presented in Fig. 8o. In all simulations, the steady-state analysis is used to explain how the Seebeck effect causes an electrical potential to build up across the leg and how heat moves through the leg. The two modeled materials were bismuth telluride (p-type $Bi_{0.5}Sb_{1.5}Te_3$ and n-type $Bi_2Te_{2.7}Se_{0.3)}$ and higher manganese silicide (HMS). Simulations of both new and old TE leg geometries show that the cross-sectional area of complicated geometries (like layered structures where the cross-sectional area changes along the leg length) may lead to higher output electrical power and thermal resistances than TE modules. The results show that TE legs with hierarchical topologies and inner voids have a significant potential. Nonetheless, it is difficult to achieve legs with complicated geometries using conventional, subtractive manufacturing methods. A resolution for such a technical challenge is offered by additive manufacturing because it makes it possible to fabricate customized parts featuring small, complicated characteristics. A recent study on the possibilities of this fabrication method for TE materials shows its promise and paves the way for greater adaptability and capability for TE technologies. The geometry of the leg has a big impact on the electrical potential and temperature difference across the leg. Layered and hollow geometries have more effective heat resistance than their filled counterparts. Particularly, layered leg geometries exhibit substantially larger temperature gradients than do the others. Since the electrical potential and temperature gradient are closely related, similar thermal trends can be applied to the open circuit voltages produced throughout each leg geometry. The temperature differential along a triangular leg is greater than that along a traditional square leg and bigger still than the temperature difference along a cylinder design. A greater temperature gradient results from the trapezoidal orientation with the small base (smaller cross-section at the hot side) than from the orientation with the large base. The voltage slope versus current in Figure 8p, q is displayed as the voltage slope to obtain the electrical resistance, which is determined by dividing the short circuit current by the open circuit voltage ($V_{oc)}$. The electrical resistances are the same for the filled cross-section legs because these legs have similar cross-sectional areas. However, the V_{oc} achieved for a squared-shape leg is lower than that of a triangular leg, and the lowest V_{oc} is likewise found for a circular leg. Due to the identical cross-sectional area for current transmission in both filled and hollow geometries, their

electrical resistances are equivalent. The hollow geometries have slightly higher values of V_{oc} because of the changes in temperature gradients observed throughout their legs. The related cross-sectional area dedicated to current conveyance for the layered geometries changes along the leg length.

Given the availability of regions featuring smaller cross-sectional areas, layered legs are of higher resistance compared to that of the other geometries. This agrees with the findings of the thermal resistance test. Compared to the traditional square-filled geometries, the trapezoidal ones are of higher internal resistances. Although the V_{oc} of the trapezoidal leg with a similar base is the same as that of the hollow legs (which is noticeably higher than that of the filled legs), the maximum V_{oc} occurs in layered legs. The theoretical power was estimated as a function of electrical current for each leg geometry, and the results are shown in Figure 8 r, s. The triangle leg displays a larger electrical power output despite the thermal radiation between layers in the layered leg geometry, layered legs have a wider total temperature differential throughout the entire leg than the square and cylindrical legs, which is caused by the higher temperature difference across the tria ngular legs despite the modest changes in electrical resistance. Compared to the filled square legs, the trapezoidal shape featuring a small base gives larger output power. The filled geometries lead to lower electrical power compared to the hollow ones, and in terms of the electrical power output, the layered geometries present the maximum advantage. Besides the advantage of the layered geometry in collection of legs in a TE module (for higher manganese silicide material), with higher electrical power output and V_{oc}(in comparison to other geometries) is reapproved. The overall temperature gradient throughout the entire leg is larger in layered legs despite the thermal radiation between layers in the layered leg geometry.

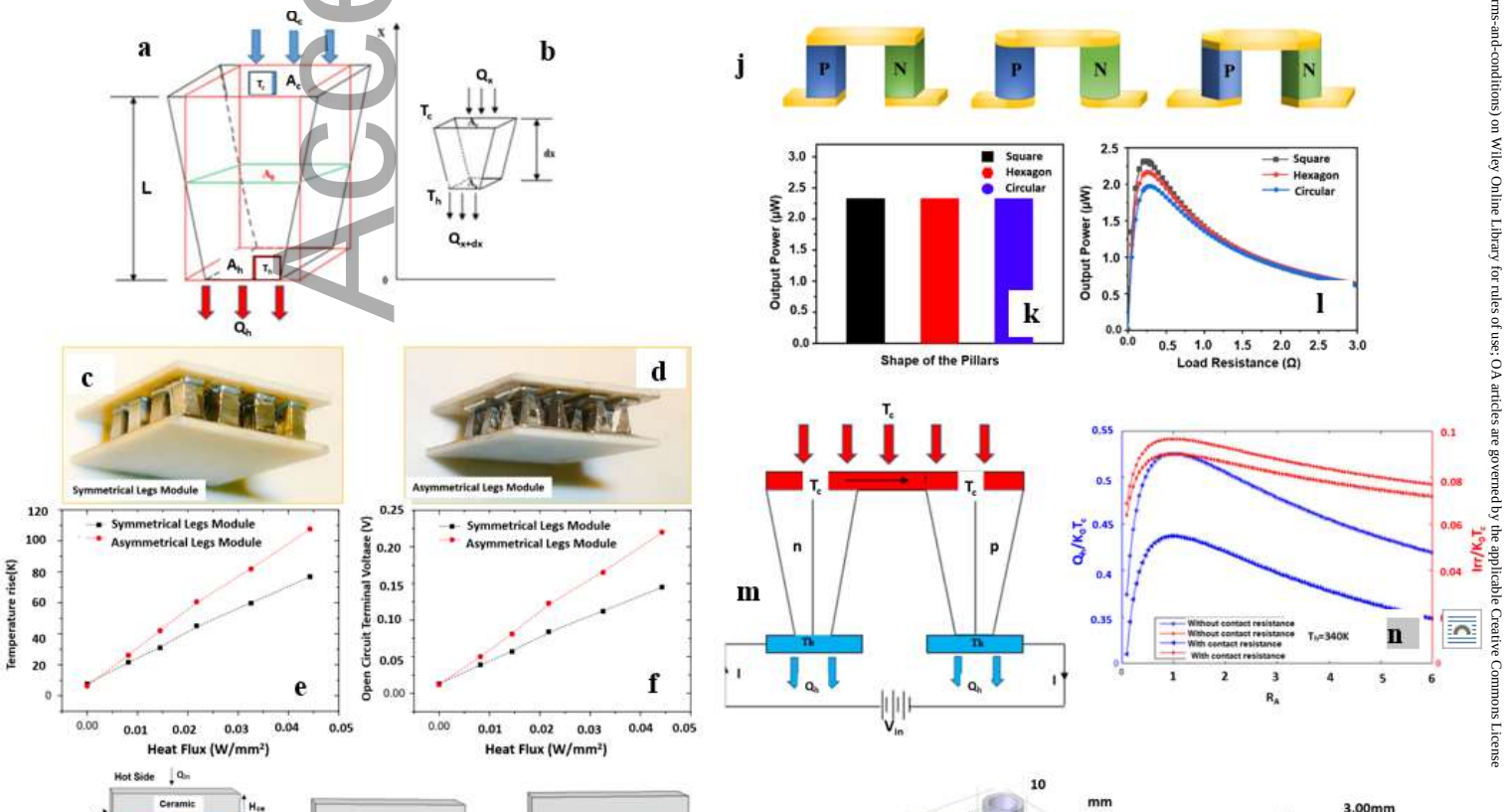

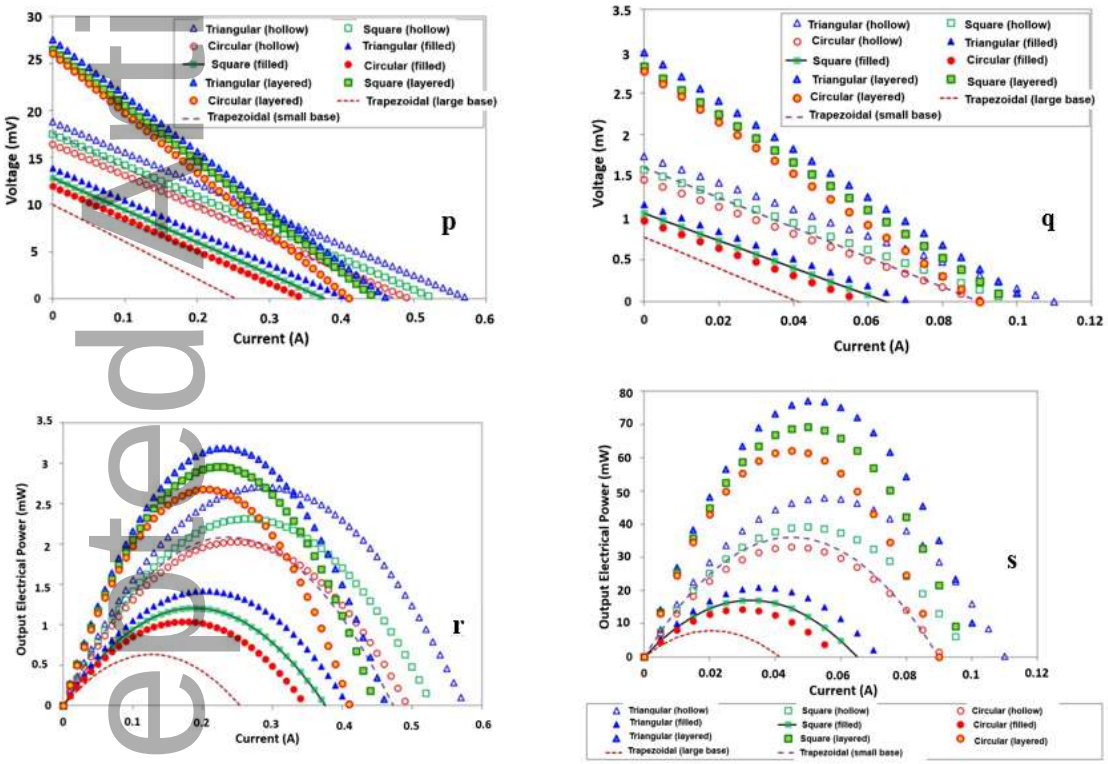

Fig. 8. (a) **…odule (c) with sym… :ed TEG (h) segment… g and two distinct pillar shapes; (k) output power for constant cross-sectional areas of various pillar shapes, and (l) Different pillar shapes at a 5 K temperature gradient with varying cross-sectional areas: output power vs. load resistance (preserving the device's effective surface area) [117]. (m) Trapezoidal thermoelectric heat pump schematic [138]. (n) R_A and the variation of dimensionless heating loads and dimensionless irreversibility (o) Diagram of the modeled leg geometries showing the geometries of triangular (hollow), square (hollow), circular (hollow), trapezoidal (large base), triangular (filled), square (filled), circular (filled), trapezoidal (small base), triangular (layered), square (layered), and circular (layered). The square (filled) geometry (of) approximates the conventional leg geometry. Each leg's shape for the open circuit voltage and short circuit current (p) higher manganese silicide and (q bismuth telluride. Output electrical power for legs made of (r) higher manganese silicide (s) bismuth telluride [139].**

By employing the COMSOL Multiphysics 5.5 FE software package, Li et al. [140] studied a variety of shapes of a hollow cross-section leg for TEGs from the mechanical and thermal perspectives simultaneously. The energy efficiency, Von-Mises stress, and output power/voltage were estimated for the mentioned structures, and the optimal conditions were determined. At the maximum input heat flux, the triangular shape, as a sample result, is capable of generating up to 100% more power

(in comparison with the rectangular one), whereas it is a less reliable design from a mechanical perspective. Figure 9a presents a schematic view of the TEG along with the entire basic geometry. To design the TE legs, five different geometric shapes are considered, which include square, circular, rectangular, triangular, and octagonal shapes depicted in Figure 9b. To improve the accuracy of the simulations, Bi_2Te_3 is used for the p-type and n-type pins, whose properties are thought to depend on temperature. Figures 9c, d display the results of the analysis of the effect of leg cross-section on output power and conversion efficiency at various cold side temperatures (heat flux is constant at 10000 Wm^{-2}). Cold side temperature varies within the 25°C-50°C range. The TEG's output power and DC voltage drop when the cold side temperature rises because there is less of a temperature differential along the device's legs. For the entire range of tested cold side temperatures, more power is generated by the triangular cross-section. Figure 9d amply demonstrates how the output power reduction impacts the TEGs' conversion efficiency, and increased cold side temperature leads to lower efficiency values. For hollow leg structures, $R_A = A_i/A_0$ defines the ratio of the inner hollow area to the total area in which A_i and A_0 stand for the area of the inner hollow section and the base area of shapes in filled conditions, respectively. The effects of R_A on the maximum conversion efficiency and output power are depicted in Figures 9e and f. It is evident that as the R_A value increases, the system's power generation increases. The higher R_A values indicate a lesser volume of legs and thinner legs. As the R_A value increases, the system's internal resistance is decreased, which is due to the fact that the cross-sectional area of the legs and internal resistance of TE devices are negatively correlated. As a result, as the R_A value increases, one can expect higher output power and electric current. The results also show that the TEG with triangular-shaped legs produces more power, while the usual square-shaped legs produce the least power. Figures 9 g, h illustrate the maximum Von-Misses stress subject to various cold side temperatures (even as the heat flux remains constant) and various heat fluxes (even though the cold side's temperature is constant), respectively. As Figure 9g, h shows, for the entire range of cold side temperatures and heat fluxes, compared to other cross-sections, triangle cross-sections generate more stress. The stress intensity in the triangle cross-section increases with the input heat flow. The smallest stress is associated with the circular cross-section. Thus, the most mechanically reliable design is that of a TEG with circular-shaped legs.

Doraghi et al. [141] used COMSOL Multiphysics to study the models featuring variable cross-section legs. The selected base material for their design was Bi_2Te_3. Figs. 9i-k show the entire geometries, which are of similar dimensions (5 mm × 6 mm × 1.5 mm). The current standard leg geometry is that of legs featuring rectangular geometry (see Fig. 9i), which has been selected as a reference. The temperature distributions are presented in Fig. 9 l-n for different models. A comparison of different models is presented in Fig. 9o. According to the results, a relatively smooth course is experienced by the rectangular shape leg. The cone- and diamond-shaped geometries experienced different courses. The distribution of thermal stress is depicted in Figure 9p–s. The hot junction side is where the von Mises stress is at its highest, as shown in the figure. For the diamond-shaped model, the maximum von Mises stress was 1.45×10^8 Pa, which was lower than that for cone- and rectangular-shaped models by 1.74×10^8 Pa. Overall, it can be said that the geometry of the leg has a significant impact on the thermal stress produced in the TE modules. Thermal stress is primarily produced in the region near the hot connections. The maximum stress is also formed around the leg edges. The thermal stress inside the device, which has the potential to reduce the service life of the TEG, limits the temperature difference in potential application. In addition, material failure as a result of the cracking induced by high stresses impairs the intended functions of the system. Investigating the

growth and production of thermal stress in TE systems is therefore essential, especially considering their long-term operations. Figure 9t-w presents the electric potential analysis. As seen in Fig. 9w, the new cone and diamond TEG models both generated larger voltage potentials than the traditional rectangle TEG.

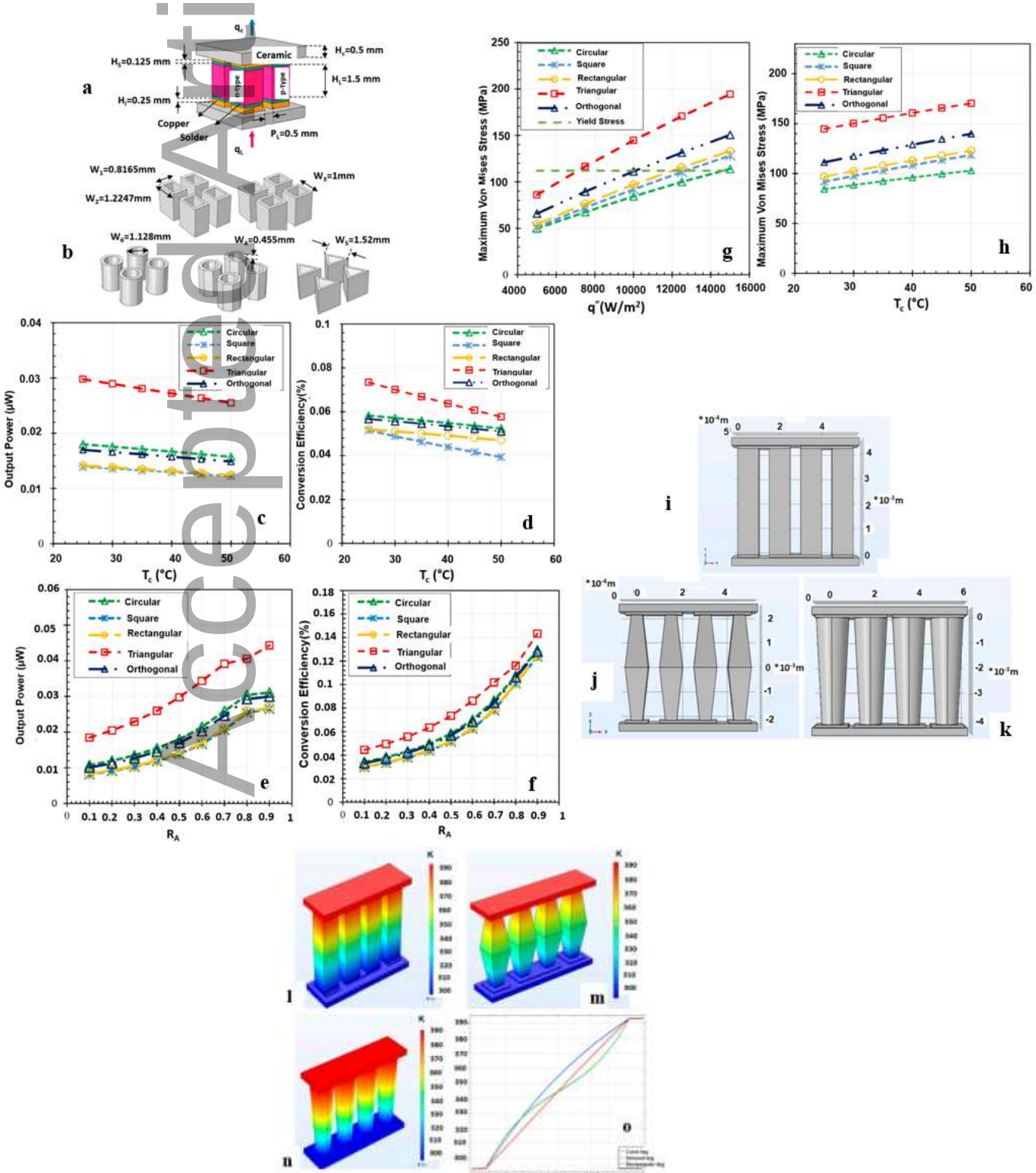

Fig. 9. a) The dimensions and thermoelectric generator's schematic, b) a number of examined ring leg cross-sections and their geometries Leg cross section effects on c) output power and d) on the effectiveness of conversion at varied cold side temperatures (heat flux = 10000 W/m2). The impact of the inner hallow area to overall area ratio (R_A) on (e) power generation (f) conversion efficiency (heat flux = 10000 W/m2). g) Leg cross section effects on Von Misses Stress under various heat fluxes and h) Leg cross section effects on Von Misses Stress at various cold side temperatures [140]. Geometry of the TEG legs analyzed: (i) Rectangular shape, (j) Diamond shape and (k) Cone shape. Analysis of TEG Temperature Distributions of (l) Rectangular shape, (m) Diamond shape, (n) Cone shape and (o) distributions of temperature for the examined geometries. The electric potential produced in (p) Rectangular fotm, (q) diamond form, (r) Cone form and (s) Voltage Comparison. The Stress analysis in (t) Rectangular shape, (u) Diamond shape, (v) Cone shape and (w) Von Mises Comparison [141].

Al-Merbati et al. investigated how the thermoelectric leg's geometry affected the thermal stress in TEG [142]. Three different leg geometries were examined, and it was discovered that the optimization of TE geometry was capable of lowering the stress formed in the TE legs to a large extent. The design of the TE leg shown in Figure 10 a, b was discovered to have the lowest thermal stress. Additionally, Mu et al. [143] investigated the extent to which geometric dimensions had an impact on the stress distribution in an Mg_2Si-based TEG and found that the maximum first principal stress of the TE legs increased as the length and width of the legs increased. By employing ANSYS software and a 3D FEM, a numerical study was conducted. As the leg width grows, the thermoelectric legs' maximum first primary stress increases nonlinearly. (See Figure 10c).

A number of studies on the relationship between the geometry of the TE legs and the mechanical performance of the TEG were conducted by Erturun et al. [144]. According to their findings (shown in Figure 10d–g), at a temperature difference of 100 °C, the rectangular legs had a thermal stress of 49.9 MPa and the cylindrical legs had a thermal stress of 43.3 MPa . Additionally, they discovered that using coaxial-leg configuration lowered the maximum stress of TE legs by 10% [145]. Additionally, they discovered that increasing the leg spacing and width and decreasing the leg height all resulted in increased thermal stress [146]. Bakhtiaryfard et al. [147] carried out numerical simulations for a variety of TE module geometries in order to study its mechanical performance under similar operating conditions and discovered that, compared to the traditional rectangular TEG, the circular shape resulted in a 13% reduction in stress. The thermal stress assessment was carried out using the finite element programme ABAQUS. Ibeagwu [148] conducted a thorough investigation on the stress on TEGs caused by varied leg shapes. The author concluded that the thermal stress in the new geometry was lower than that in the conventional geometries after studying four different leg shapes (see Figure 10e-j).

KARRI et al. [149] used the commercial FEA software ANSYS to carry out numerical simulations in order to model the thermo-mechanical stresses produced by the TE effect and the accompanying temperature distribution. In all investigations, an n- and p-type bismuth-telluride constant property couple is taken into account. They created a procedure to assess the reliability of brittle TE materials in line with standard procedure in the ceramics sector. By employing the Weibull analysis, the probabilistic thermo-mechanical reliability of TEG modules and couples was estimated. At shorter lengths, the cross-sectional geometry had a significant effect, and as the length increased, the effect declined. The performance optimization strategies could be combined with the structural integrity assessment method to produce reliable and perfect TEG. The reliability and stresses of TEG with a variety of typical cross-sectional geometries were explored, as well as the effect of the leg length to cross-section area ratios. The contours of von Mises stress in the modules featuring 4 MPa compressive load and constant hot-side conditions are illustrated in Fig. 10-o. As the picture again shows, the cold-side interface's furthest corners were where the von Mises stresses were the highest, producing 238 MPa, 272 MPa, 154 MPa, and 169 MPa for the square, hexagonal, octagonal, and circular legs, respectively. The reliability evaluation results from the two pair module simulations with fixed hot-side interface circumstances are summarized in Table 2. With the constant hot-side conditions, TE legs with circular and square cross sections produced the lowest (4.5%) and highest (0%), respectively, reliability levels. While in both cases, the external compression enhanced the reliability, In the case of the fixed hot side situation, the effect is confirmed, in which an absolute 5–75% enhancement was witnessed in module reliabilities for squared- and cylindrical-shaped legs, respectively.

Table. 2. Summary of reliability evaluation results from two couple module simulations [149].

	Fixed hot-side	
	%R with no load	%R with 4 MPa compression
Square	**0**	**4.5**
Hexagon	**0**	**44.0**
Octagon	**2.5**	**70.5**
Circle	**4.5**	**78.0**

The results also show that, in contrast to cross-sectional shapes, leg length is a geometrical parameter that governs the overall stresses. Legs' length and boundary conditions both affect how their cross-section geometry behaves. The concentration of local stresses reduces the durability of TEG couples with legs fixed (connected to a rigid substrate) at both ends; hence, cylinder-shaped legs with smooth cross sections are preferable.

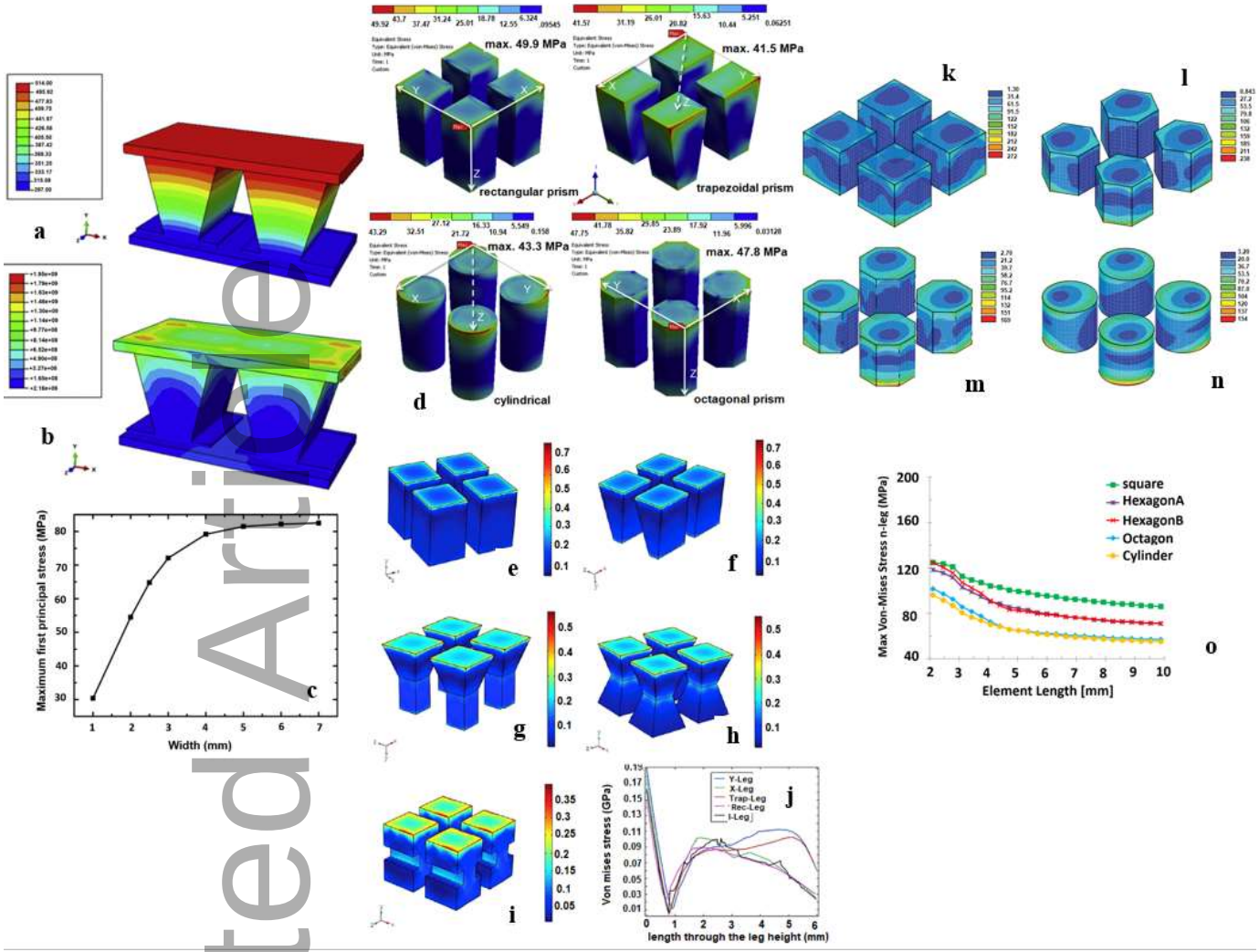

Fig. 10. (a) 3D spread of temperature and (b) thermal stress distribution [142]. C) Maximum first major stress vs leg width (W) in the TE legs [143]. (d) Maximum distribution of leg stress as a programme [144] Distributions of thermal stress in GPa for(e) Rect-leg (f) Trap-leg (g) Y-leg (h) X-leg (i) I-leg and (j) centerline stress profile [148]. the outlines of the maximum von Mises stress (Pa) in two couple modules with (k) square, (l) hexagon, (m) octagon, and (n) legs with a round cross-section and a fixed hot-side condition(o) Peak von Mises stresses in the presence of fixed hot-side hot-side contact conditions: Effect of leg cross-section geometry [149].

3.4 Number of TE legs and configuration

A numerical and experimental examination of the optimization of the TE module geometry to increase the power output at a reduced cost was conducted by Dongxu et al. [150]. It was looked into how the TE module coupling number affected the module's effectiveness and power output. According to the obtained results (depicted in Figure 11 a, b), as the number of legs increases, the power output is increased monotonically. This is attributable to the decreased electrical and thermal contact resistances. The effect of the TE module couple number on the module's efficiency and power output was looked into.

A two-stage TEG that was optimized by Liang et al. [151] and compared to a single TEG. They found that the output power and heat absorbed increased with the total number of TE legs; nonetheless, the conversion efficiency declined. Additionally, they found that, in compared to the cold source

temperature, the heat source temperature had a greater impact on the TEG performance. The efficiency and output power of a two-stage TEG are shown to be correlated with the number of TE legs in the bottom stage (n), the total number of TE legs (M), and the overall number of TE legs. The findings demonstrated that as M was increased, conversion efficiency declined, and maximum optimum output power increased (depicted in Figure 11 c, d). Lately, Luo et al. [152] recommended employing more TE legs to increase the TEG's output of power. Additionally, they found that the maximum efficiency and maximum power output of the TE module increased by 1.2 percent and 1 percent, respectively, as the number of TE legs grew (see Figures 11 e, f). The mechanical stability and reliability of TE modules were adjusted and examined by Miao et al. [153]. They concluded that optimizing the number of TE legs can reduce the internal stresses created in the module and improve its operational stability (see Fig. 11g).

Using the FVM, Meng et al. [154] simulated the typical performances of a 3D helical thermoelectric module and compared them to those of a traditional straight module (see Figure 11h). After looking at the relationship between the geometric parameters of the helical thermoelectric module and the different performances, an ideal helical design was proposed to get better performance. According to the simulation results obtained in the FLUENT environment, the helical module is capable of harvesting more heat compared to the straight one and, as a result, produces higher output power. This is because the two modules have nearly the same conversion efficiencies. The helical module's increased pitch has a favourable impact on its distinctive performances, including enhanced output power, improved heat harvesting, and improved conversion efficiency. In the helical module, the unit output power, unit heating area, and unit input heat decrease as the module diameter rises, but the radial expansion of the helical module has an opposite effect on the unit performances, which is represented by dividing the characteristic performances by the number of p-n pairs. Using a helical module with a shorter diameter and a longer pitch, higher performances can be obtained. At the same temperature difference between the cold and hot sources, Figure 11i demonstrates that the current and voltage of the helical module are greater than those of the straight module.

Tian et al. [155] scrutinized a hollow cylindrical configuration where the p-type and n-type legs are situated co-axially inside one another. Bi_2Te_3 material is chosen for the p-type and n-type legs. To study the suggested structure from economic, thermal, mechanical, and exergetic perspectives, Comsol 5.5 Multi-physics was used. One can prepare the cylindrical ring-shaped co-axial configurations in a variety of azimuthal angles. The ring-shaped structure can decrease the thermal stress level without reducing thermal efficiency. The parts of the cylindrical TEGs considered in this investigation are shown in Figure 11j by an assumption of a θ=360° azimuthal angle. The cylindrical TE is shown with other azimuthal angles, namely, θ=45°, 90°, and 180°, in Figure 11j. Figure 11k-m depicts the voltage, von Mises stress, and temperature distributions of a cylindrical TEG at a hot side temperature of 423.15 Kelvin, respectively. It is evident that when θ= 90°, on the heated sides of the legs, the contact zone is where the maximum electric potential, von Mises stress, and temperature gradient all occur. A closer look at the contact points reveals that the parts closest to the edges are those with the greatest risk of damage. θ and the hot side temperature vary, whereas other parameters are maintained at base conditions (ϕ = 0, W_L/ P_L = 0.5, and $T_c = 298.15K$). Figure 11n, o shows that the output power increases together with the hot side temperature for a cylindrical thermoelectric generator (CTEG) for any given azimuthal angle (θ). For azimuthal angles (θ) of 360° and 180°, a CTEG's highest output power at a hot side temperature of 373.15 Kelvin is 0.022 W and 0.011 W, respectively. Figure 11 o makes it abundantly evident that, in a number of

the case studies, CTEGs' legs experience thermal stress that is greater than their yield stress, which may shorten the system's lifespan.

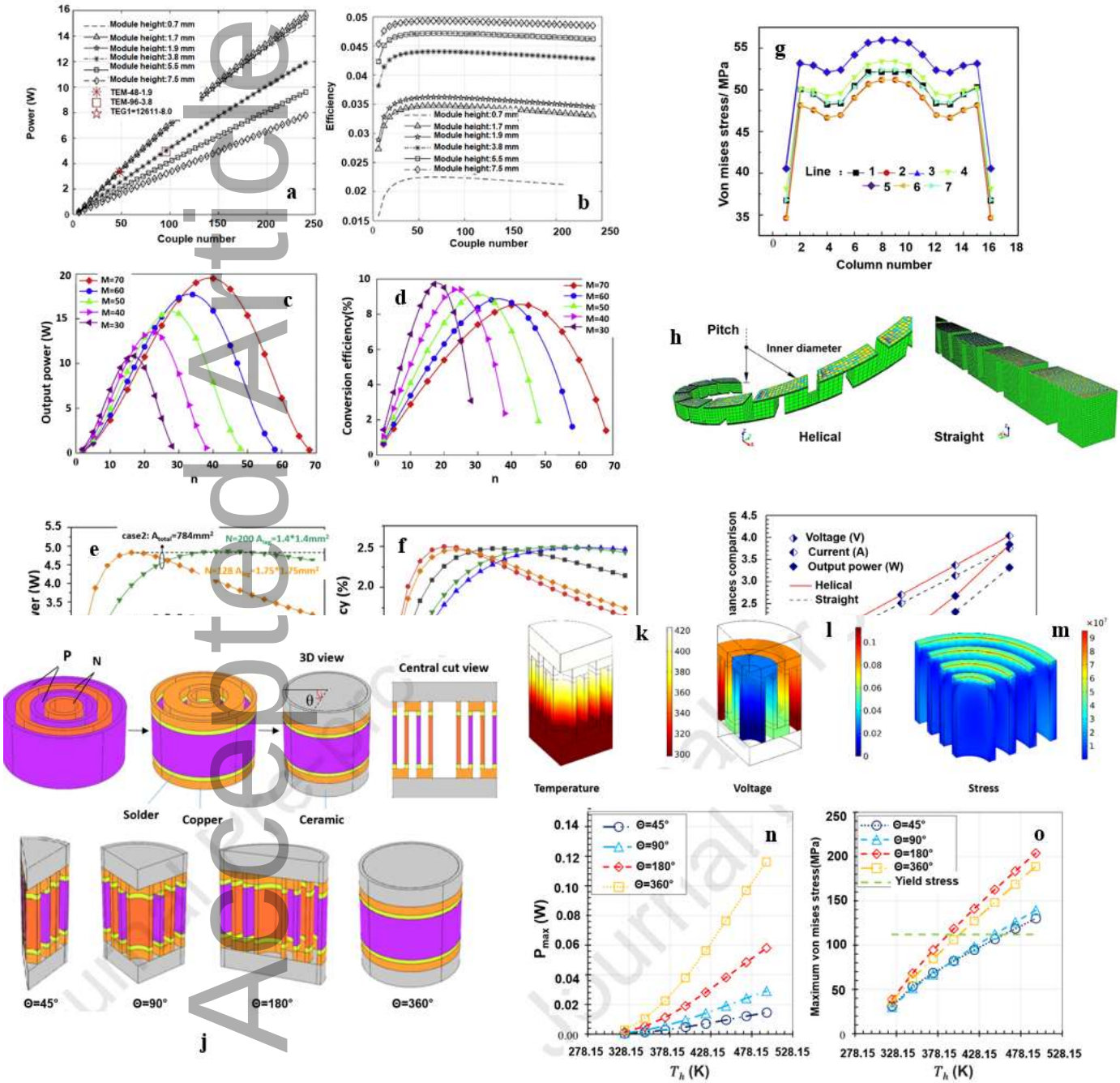

analysis of basic module group [153]. (h) Meshed models of TE modules. (i) Output performance of helical and straight modules [154]. (j) cylinder-shaped thermoelectric generator types and thermoelectric with different azimuthal angles θ. Graphs showing the distribution of(k) temperature at θ = 90° T_h = 423.15 K (l) voltage. The impact of hot side temperature (T_h) on a CTEG device's thermomechanical performance (m) output power and (n) maximum von Mises stress [155].

k

l

Choo et al. [33] employed TE characteristics of the 3D-printed Cu_2Se thermoelectric materials and COMSOL Multip hors in order to

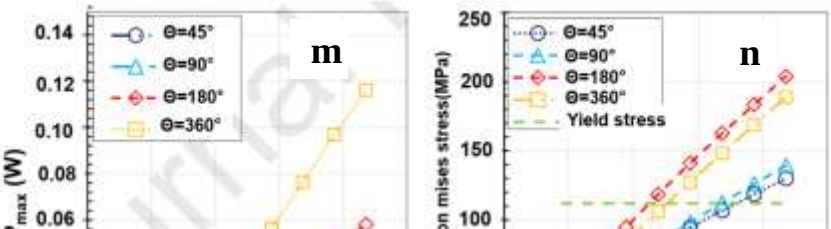

enhance the mechanical durability of TE legs. Honeycomb structures are renowned for having a high strength-to-weight ratio because of their efficient dispersion of external forces, particularly out-of-plane stress. They use a cuboid, a hollow hexagonal column, as a basic building block when creating honeycomb architecture because they have the ability to print them, and a honeycomb is made up of seven hexagonal columns. Honeycomb and hexagonal modules require lower amounts of heat in order to reach the same ΔT in comparison with a cuboid module. This can be attributed to the electrodes' less efficient heat spread. The enclosed zone on the cold side of the honeycomb and hexagonal modules is expected to have a negligible steady-state heat flux, as shown by the simulated heat flux distribution (see Figures 12a-c). This is because the electrode temperature is kept uniform (Figure 12a). The simulation findings demonstrated that, in comparison to a cuboid, the recommended cellular architectures could boost power generation efficiency. They used the three-dimensional FEM to compare three different topologies, i.e., a hollow hexagonal column, a honeycomb, and a cuboid. One can define generation efficiency as the power output to heat input ratio. It is anticipated that the honeycomb designs and hexagonal column will demonstrate 7.7 percent and 7.3 percent efficiency, respectively, which is 26 percent and 22 percent higher than the efficiency of ordinary cuboids, at a hot-side temperature of 873 Kelvin (see Figure 12d).

The new (Bi, Sb)$_2$Te$_3$-based multilayer composite structured thermoelectric module (MCTEM) developed by Wang et al. [156] is capable of achieving high power outputs. Such a novel design of MCTEM paves the way for its commercialization and fabrication via the development of a high-power TE generators. Fig. 12e, f illustrates the schematic views of a traditional TE module (TTEM) and an n-type $Bi_2Te_{2.79}Se_{0.21}$ single-leg MCTEM as examples. Figures 12g, h show the schematic views of the MCTEM and the classic TE module of the type. For the π-type MCTEM, the above optimized p-type $Bi_{0.5}Sb_{1.5}Te_3$ single-leg MCTEM and n-type $Bi_2Te_{2.79}Se_{0.21}$ single-leg MCTEM have been employed as the legs of the π-type MCTEM. The performance of π-type MCTEM and TTEM has been compared in Fig. 12i-k. When compared to the TTEM values, the coordinated variation of P_{max} and V of π-type MCTEM is enhanced. At T = 35 °C, the maximum value of Pmax is 10.5 mW, which is around 4.2 times more powerful than the conventional TE module.

Oualid et al. [16] made a new design for a flexible μ-TEG by using laminated copper/polyimide/copper plates to deposit wavy-shaped Bi_2Te_3-based TE materials. The copper plates helped heat move to and from the heat source and sink (see Figure 12l). They presented a cutting-edge μ-TEG design that successfully blended the benefits of cross-plane and in-plane systems. Compared to the architectures suggested before, a number of the advantages offered by this design are: i) a high thermal resistance (generally about 1 K W^{-1} for 1 cm^2 area of the TE elements) as a result of the employed specific geometry; ii) use of copper plates, which may be connected readily to a heat source and/or a heat sink for dissipation as needed and act as heat spreaders. A remarkable electrical power generation of 5.5 μW for each thermocouple during operation under a temperature difference of just 5 K, in accordance with computational models based on finite element studies, is another way they show that high TE performances are attainable near room temperature. The performances of the two μ-TEGs, which were constituted of 120 and 15 thermocouples featuring optimized geometries and produced via an easily scalable procedure because of current SMD (surface mounted-device) technology, are closely in line with the anticipations of finite element analyses, demonstrating the excellent experimental control of electrical contact resistances.

The efficiency, thermal stress, and power generation of a two-stage TE module was investigated by Lee et al. [157]. The ANSYS commercial program was used to calculate the performance parameters of the TE module using a numerical method. A schematic view of two-stage arrangements of a TE module is depicted in Fig. 12m. As a reference, a TE module with a single-stage configuration that consists of three conducting plates and a pair of n- and p-type TE legs was used. For a two-stage TE module composed of various materials and with various leg geometries, Figure 12o illustrates how the maximum power fluctuates with temperature difference. The maximum power was noticeably increased in the two-stage arrangement of the TE module with similar leg geometries when SiGe material was used in the first stage and Bi_2Te_3 material was used in the second stage as opposed to both stages being built solely of Bi_2Te_3 or SiGe. SiGe+Bi_2Te_3 material demonstrated maximum power of 0.46 W for square prism legs in a two-stage configuration at a temperature difference of 880 °C, 0.41 W for trapezoidal legs at a temperature difference of 830 °C, and 0.43 W for cylindrical legs. When using the SiGe material with a temperature difference of 980 °C, the trapezoidal and square prism legs displayed a maximum power of 0.25 W, while the cylindrical ones displayed a maximum power of 0.27 W. The maximum power for the trapezoidal and square prism legs was 0.12 W for a temperature differential of 480 °C and the Bi_2Te_3 material, whereas the maximum power for the cylindrical legs was 0.13 W. while in a single-stage configuration The maximum power displayed by all leg geometries made of SiGe material was 0.65 W at a temperature difference of 980 °C, and the greatest power displayed by all leg geometries made of Bi_2Te_3 material was 0.31 W at a temperature difference of 480 °C (Fig. 12n).

As depicted in Fig. 12q, for the two-stage TE module featuring a variety of materials and leg geometries, the maximum stress varies linearly as a function of temperature. For the trapezoidal and square prism legs in the context of the Bi_2Te_3, SiGe+Bi_2Te_3, and SiGe materials, the maximum stress variation with temperature difference was nearly identical to and greater than the maximum stress values for the associated cylindrical-shaped legs. With regard to the identical leg geometry, the SiGe+Bi_2Te_3 material showed the highest level of stress, followed by the Bi_2Te_3 and SiGe materials. The highest stress for the trapezoidal and square prism legs for the temperature difference of 980 °C and using the SiGe material was 1.62 GPa, whereas the maximum stress for the cylindrical-shaped legs was 1.38 GPa. At a temperature difference of 480 °C, the trapezoidal and square prism legs had a maximum stress of 0.82 GPa, but the cylindrical-shaped legs displayed a maximum stress of 0.7 GPa under the same circumstances. The maximum stresses for the trapezoidal and cylindrical legs of the SiGe+Bi2Te3 material were 1.81 GPa and 1.56 GPa, respectively, at a temperature difference of 830 °C, while the largest stress for the square prism legs was 1.91 GPa at a temperature difference of 880 °C. The trapezoidal and square prism legs with $A_{legs,hotside} > A_{legs,coldside}$ and $A_{legs,coldside} > A_{legs,hotside}$ displayed the maximum stress of 0.96 GPa in a

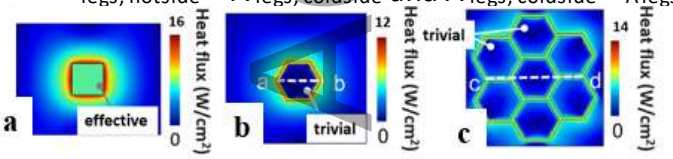

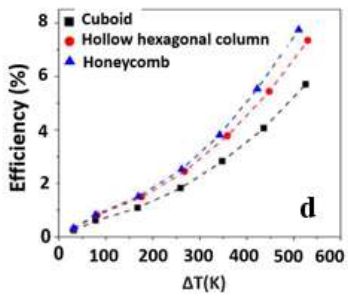

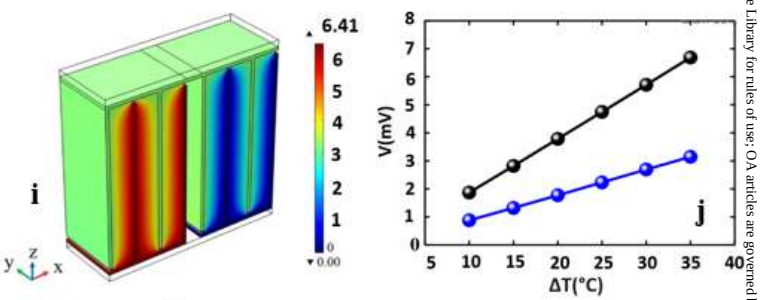

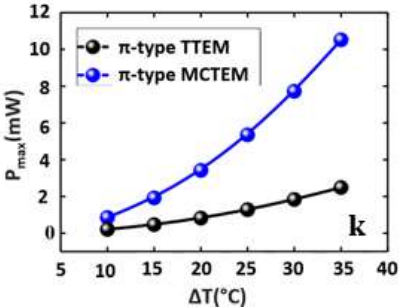

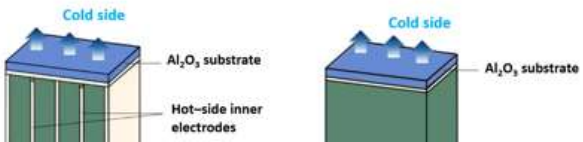

m

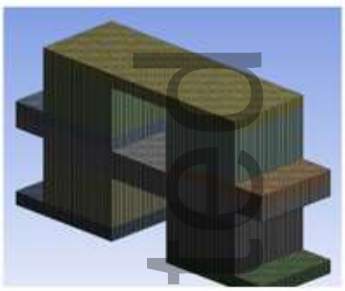

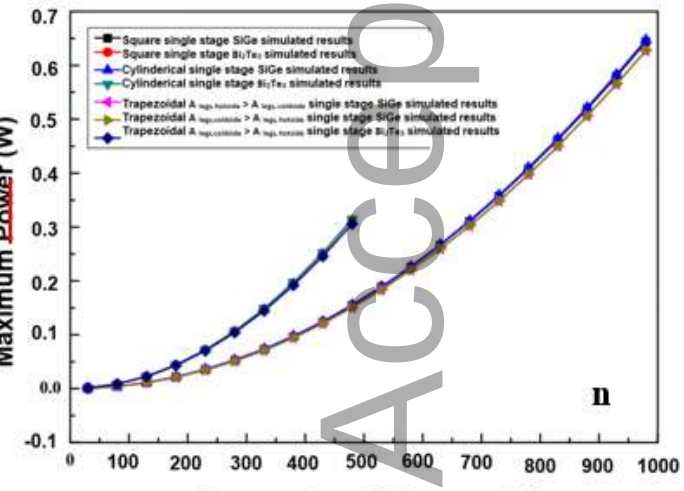

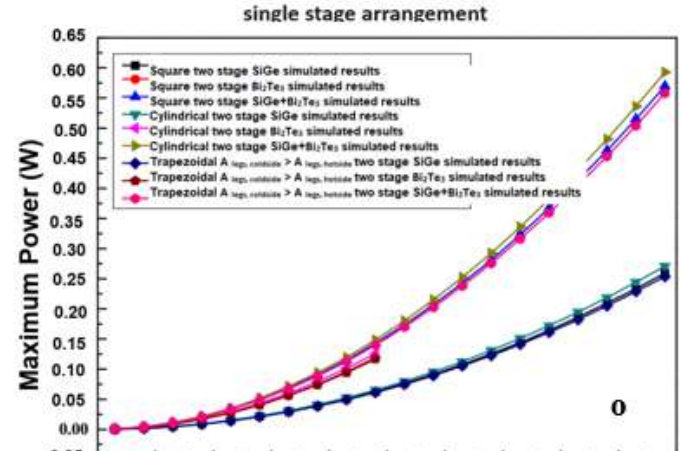

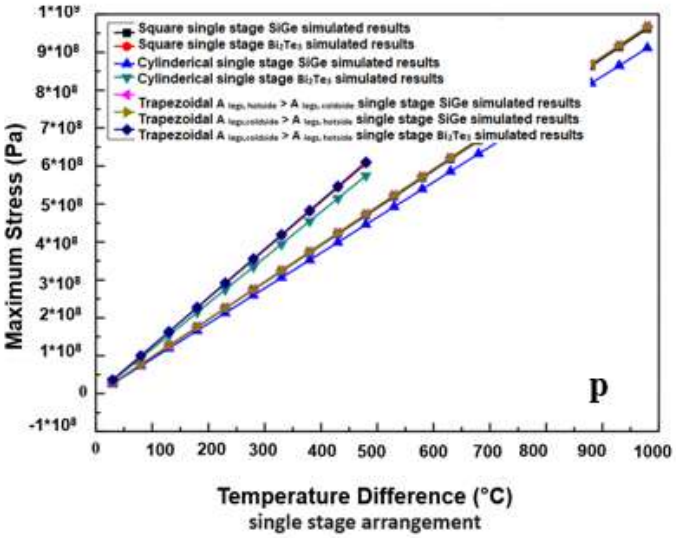

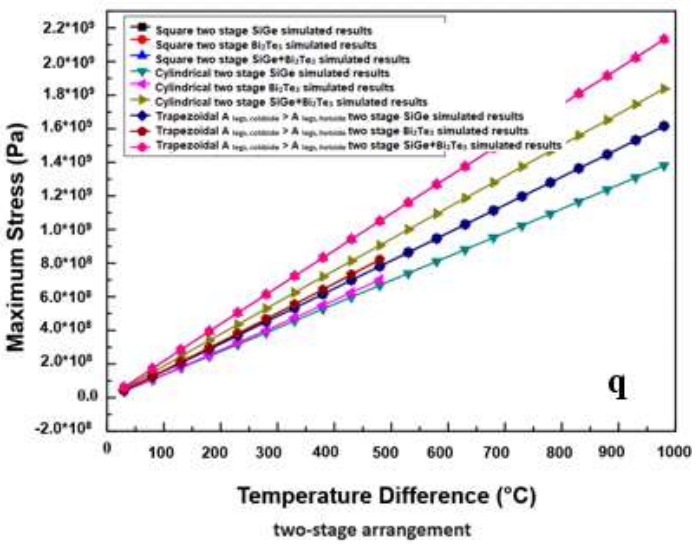

Fig. 12. Distribution of the simulated heat flow on the cold side of(a) cuboid-, (b) hollow hexagonal column-, and (c) honeycomb-shaped (d) Cu_2Se TE legs' generation efficiencies at temperatures between 323 and 873 K on the hot side [16]. Schematics of the n-type (e) Multilayer Composite Single-Leg Thermoelectric Module (single-leg MCTEM) and (f) common thermoelectric module with one leg (single-leg TTEM). Schematics of the (g) Multilayer composite thermoelectric module of the π-type (MCTEM of the π-type) and (h) π-type traditional thermoelectric module (π-type TTEM). i, j) When ΔT is 35 °C, the electric potential distribution in an open-circuit MCTEM of the π-type (k) Maximum output power as a function of ΔT for the MCTEM and TTEM of π-type. [156]. A perspective view of our planar micro-TEG's design. A wavy route is formed by the n- and p-type Bi_2Te_3-based materials [16]. (m) Two-stage arrangement. Maximum power for (n) a single-stage setup, (o) two-stage arrangement. Maximum stress for (p) single-stage configuration (q) two-stage configuration [157].

4. Micro-additive manufacturing of 3D micro-architected thermoelectric generator

Due to the high thermal barrier resistance and the fact that μ-TEGs traditional production approaches are limited to planar form factors (i.e., only thin, flat devices), effective heat transfer on non-planar surfaces is made challenging. Additionally, if leg shape significantly impacts μ-TEG leg and device thermal resistances, why are leg geometries and sizes so constrained? The solution relate to fundamental constraint on TE device advancement. Traditional manufacturing methods, take a significant amount of time and need the acquisition of pricey equipment High-energy processes, including ball milling, arc melting, melt spinning and spark plasma sintering, are often utilized in the conventional manufacturing of TE devices [158]. Legs made from the resulting ingots are then joined between metal contacts on ceramic substrates [158]. A significant portion of the TE material is thrown away at every stage of the process, but particularly during the dicing step [158]. Besides, as a result of the typical manufacturing method, the leg (cuboid geometry) and device shapes and sizes have been mainly limited. Therefore, topological optimization of bulk 3D TE legs and devices has generated a lot of interest in the creation of adaptable, shape-conformable geometries. As a result, a wide variety of micro-fabrication technologies have been created, each with a unique set of capabilities and uses as their fundamentals are very diverse. But Micro- and nanofabrication technologies must be improved in light of the current trend toward product miniaturization of microelectronic devices. These global megatrends have a significant impact on micro-manufacturing platforms as well.

There are a number of drawbacks to traditional micro-manufacturing technologies, such as difficulty in fabrication of complex shapes, material limitations, problems with tools, and the inability to really make things in three dimensions (3D) [159]. Numerous micro-manufacturing methods, including soft lithography [160], laser photoablation [161], localized electrochemical deposition [162], the LIGA (Lithographie (LI) Galvanoformung (G) Abformung (A)) method [163, 164], etc., have been developed, which has facilitated the technology's ability to create more and more intricate shapes. Manufacturing intricate 3D microstructures remained difficult in all of them. New approaches like micro-additive manufacturing (micro-AM) can be considered to enhance the capabilities of micro-fabrication technology in the area of producing actual 3D micro-components.

When a part is constructed utilizing AM, which enables the construction of free-form structures by layering a part, the majority of geometric limitations imposed by traditional subtractive manufacturing procedures are removed. The fabrication of TE materials and equipment has recently utilized additive manufacturing, often known as 3D printing. Numerous low- and high-temperature TE materials, such as bismuth telluride, higher manganese silicide (HMS), half Heusler, and skutterudite, have been shown to be amenable to additive manufacturing techniques. These breakthroughs in manufacturing capabilities allow for previously unimaginable μ-TEGs leg forms and sizes: a new frontier in the design of μ-TEGs legs have been opened. Rapid prototyping in a variety of sizes and shapes, as well as the efficient use of raw resources, are all advantages of additive manufacturing technology [41, 165]. Additive fabrication affords TE energy harvesting devices several options. This innovative method of manufacturing provides:

- Customizable leg designs.
- Minimal thermal boundary resistances.
- Less retooling.
- Reduced waste of TE materials.
- Manipulating microstructure for getting more remarkable figures of merit.

Hence 3D printing could be used to build Micro-Architected TEGs for various purposes (shape-versatile 3D thermoelectric). In conclusion, bulk μ-TEGs structures that have been topologically optimized and additively built offer an excellent option for TE energy harvesting and thermal control applications. It has only recently become possible to produce 3D micro-features on a number of materials, including metals, polymers, and ceramics, using micro-scale AM processes. Following is a discussion of AM techniques for micro-component fabrication.

4.1. Description and classification of 3D micro-AM (micro-additive manufacturing)

In recent years, AM at the micro-and nanoscale has garnered considerable interest, as seen by the proliferation of review articles on comparable approaches [39,166, 167]. Engstrom et al. have examined additive nanomanufacturing (ANM) techniques that produce components with a resolution of less than 100 nanometers (nm) utilizing a range of substances, including metals, polymers, and organic molecules [166]. For micro AM processes, a feature size of 10 μm is the standard benchmark [159]. Vaezi et al. [39] categorized 3D micro-AM into three principal groups: hybrid processes, 3D direct writing (3DDW) technologies, and scalable AM technologies. Scalable AM technologies can be employed for both macro- and micro-scale applications. Stereolithography (SL; also known as micro-SL (MSL) in the micro-scale), selective laser sintering (SLS; also known as micro-laser sintering (MLS) in the micro-scale), inkjet printing processes, fused deposition modeling (FDM), and laminated object manufacturing (LOM) are scalable AM technologies that have been viewed as a promising method for true complex 3D micro-components/assemblies. Micro stereolithography (MSL), while having a limited selection of materials, has emerged as the most effective micro additive manufacturing (AM) method due to its excellent resolution and repeatability [168]. Because they can't produce high feature resolution, both FDM and LOM methods have trouble processing metals. In the past, inkjet printing employed metal inks [169], but non-metals are still absolutely forbidden while employing this method. The printing of several materials and cold processing with 3D printing (3DP) and binder jet printing (BJP) offer promise even though the completed items often have a lot of porosity [170]. SLM and SLS, which stand for layer-by-layer melting on powder-bed or binder-based sintering, have shown promise for processing metals and ceramics without any resins (as in MSL) or binders (as in 3DP or BJP), thanks to their capacity to create real 3D micro-parts with good resolution [171]. Ink-based dispensing, aerosol jet,

laser transfer, and beam deposition techniques like EB and EB/LCVD writing are all included in the three-dimensional direct printing process. The processing of the direct writing technique has proven to be rather difficult and time-consuming, even though it typically has a high resolution that is adequate for nanoscale production [166, 167]. SDM (shape deposition modelling) and EFAB (Electrochemical FABrication) are part of the third set of 3D micro-additive technologies, which are known as hybrid methods. The AM techniques indicated in table 3 are used to create bulk TE structures with thicknesses in the millimetre range: material extrusion, laser powder bed fusion, and vat photopolymerization [158]. There are significant efforts to apply these techniques to microscale production. This article examines these printing techniques.

Table 3. AM technique classifications [158].Method	Used for	Principal	Advantages	Disadvantages	Higher ZT reported
Material extrusion	Composites, polymers, ceramics	Deposition through a nozzle in filament/ink form	Widespread. Inexpensive, adaptable	Anisotropy, high surface roughness, low resolution	1.7 at 485°C
Vat photopolymerization	polymers, ceramics	Photocuring of resin material	High resolution, excellent surface finish	Support structure neede, post processing required, poor strength	1.0 at 27°C
Powder bed fusion	Metals, Composites, polymers, ceramics	Fusion of powders via a high energy beam	High resolution, wide range of printable materials	High investment cost, size limitations	1.29 at 50°C
Binder jetting	Metals, Composites, polymers, ceramics	Selective deposition of a binding agent onto powder layers	Low cost, high speed	post processing required, poor strength	N/A
Material jetting	Composites, polymers, ceramics	Layer by layer solidification of droplets deposited using a dispenser	High accuracy, low waste, multi material	Support material needed	N/A
Sheet lamination	Metals, polymers, ceramics	Consolidation of sheet layers into bulk structures	Low cost, high speed	Post processing required	N/A
Direct energy deposion	Metals	Beam/ arc melting of a material deposited through a high degree of freedom nozzle in powder/wire form	High processing rate, large parts manufacturable	Coarse surface finish	N.A

4.1.1 Scalable AM processes

4.1.1.1 Vat photopolymerization

An AM process known as vat photopolymerization selectively consolidates a photocurable polymer resin by exposing it to a light source layer by layer. Depending on the type of light and its direction,

other names for the technology have been registered for patent protection, including Stereolithography (SLA), Digital Light Processing (DLP), and Continuous Liquid Interface Production (CLIP) [172]. Micro SLA is on the basis of classic SLA, a UV laser beam is shone on a liquid photopolymer's surface by a light source, and this hardens the photopolymer when exposed to UV light. Submicron accuracy for the x,y,z translational phases of MSL, a laser spot with a smaller diameter than in typical SLA (a few micrometers), and photopolymer solidification that takes place in a very tiny area of the resin allow it to manufacture micro components with layers as thin as 1–10 micrometers. In an experiment, microparts with various blade thicknesses were produced using a micro-SLA technique (Perfactory micro-SLA system) created by Vaezi et al. [39]. Sun et al [173].'s development of a high-resolution projection micro-stereolithography method using MEMS fabrication and the Digital Micro mirror Device is depicted in Figure 13 a, b. Because of resin viscosity and surface tension, the minimum layer thickness in micro-SLA systems is restricted. To solve this issue Ovsianikov created the two-photon polymerization (2PP) technique [174]. Figures 13c, d depict examples of the microstructures made by 2PP. With the 2PP technique, various micro/nano-3D structures can be precisely made.

From the standpoint of TE manufacturing, vat photopolymerization is currently of little interest. He and colleagues made the first attempt to make bulk samples of p-type amorphous $Bi_{0.5}Sb_{1.5}Te_3$ with ultralow thermal conductivity in 2015. $Bi_{0.5}Sb_{1.5}Te_3$ (BST) was added in amounts ranging from 40 to 60 weight percent to the composite resins before being treated with a laser beam with a wavelength of 405 nm, 1.2 watts of power, and a layer height of 100 m. (Fig 13e). The leftover resin was broken down, and the electrical conductivity was improved using a post-processing phase with settings tuned using thermogravimetric analysis (TGA). Despite the subsequent ultralow thermal conductivity of 0.2 W/m-K, the persistent porosity led to low electrical conductivity and a maximum ZT of 0.12 at ambient temperature [175]. Even though the vat photopolymerization technology provides great surface smoothness and high resolution, it faces several challenges, including a restricted number of resins that can be photopolymerizable and a necessary post-curing step to remove the resin's binder, similar to that required for material extrusion. The ZTs of samples created using this technology were much lower than those of bulk samples traditionally made [158]. The post-sintering procedure was required to get rid of resin remnants inside the TE material since the photo resin's ability to act as an electrical insulator would cause the printed material's electrical qualities to deteriorate. Photoresins underwent thermal annealing, which caused pores to develop and left the structure significantly hollow. In comparison to the hot-pressed conventional BST sample, which had a density of 6.89 g/cm3, the printed material with 60 wt% BST had a density of just 2.631 g/cm^3. In addition, the photoresin's breakdown created amorphous carbon and oxygen. The end product's poor electrical conductivity was brought on by the presence of carbon and oxygen as well as by the porous structure of the final product, as can be seen in Fig. 13f. A ZT value of just 0.12 at 43 °C, which is one-tenth that of bulk commercial Bi_2Te_3 [176], was achieved due to the material's poor electrical performance and low thermal conductivity of 0.2 Wm^{-1} K^{-1}. It was found that Park and Ferhat employed a vat photopolymerization method to fabricate orthorhombic β-Ag_2Se a bulk for use at ambient temperature, TE compound [177–179]. The tensile strength and TE properties of bulk samples with various -Ag_2Se ratios were assessed. Despite having a tensile strength drop of roughly 55 percent, samples loaded with 30 percent Ag_2Se showed a maximum ZT of 0.12 at 27 °C. For the production of bulk TE, Mallick et al. described a quasi-printing procedure utilizing vat photopolymerization. This method was used to spray n-type -Ag_2Se and p-type PEDOT inks over three distinct geometries of vat photopolymerization-printed

scaffolds for topological optimization [165]. (Fig. 13g). At ambient temperature, cylindrical bulk legs of n-type β-Ag2Se demonstrated a maximum ZT of 1.0 and maximum output power of 7 μW (see Figures 13 h, i).

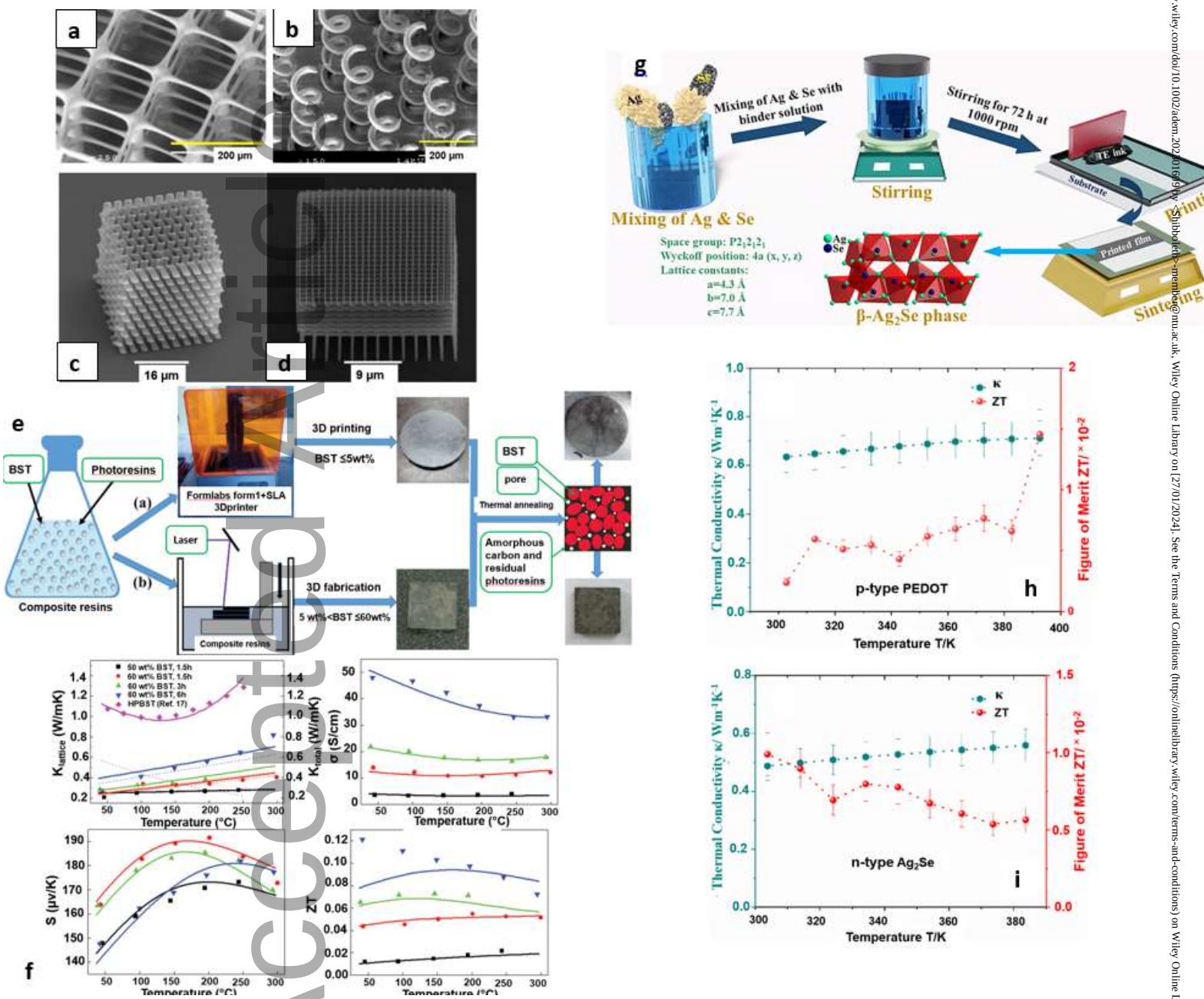

Fig. 13. PSL process-fabricated 3D complex microstructures: (a) micro matrix with a 5 m diameter suspended beam; (b) The entire size of the high aspect-ratio micro rod array, which has 21 11 rods, is 2 mm 1 mm. The rod measures 30 m in diameter and 1 mm in height, respectively [173]. c) Structures made of photonic crystals in three dimensions using the 2PP method [174]. (d) SLA 3D printing sample construction is shown schematically. (e) TE's temperature-dependent characteristics a diagram showing how printable n-type Ag_2Se films were made [174]. (f) Demonstration of the creation of printable films based on n-type Ag_2Se(g) and the p-type PEDOT figure-of-merit (ZT) and (h) n-type Ag2Se films. The ZT of the n-type film is equal to 1 [165] at room temperature.

3.1.1.2 Fusion of Powder Beds

In the process of creating a three-dimensional structure known as powder bed fusion, energy sources such as an electron beam or laser can be used to melt powder materials and layer by layer solidify them. The technology is flexible since it permits the manufacturing of small-to-medium-sized, very dense metal, composite, ceramic, and polymeric components with unique forms [158]. Powder bed fusion has several subcategories, including electron beam melting (EBM), selective laser sintering (SLS) and direct metal laser sintering (DMLS or SLM) [156]. Micro, meso, and macro-scale topological design and optimization for system-level advantages can also be made possible by this AM method. Powder particles between 20 and 50 µm in diameter are used and layers between 20 and 100 µm in thickness are produced in the majority of commercial SLM systems. According to Fig. 14 [159], the three key components that scale down traditional SLM to improve feature resolution are laser beam width, layer thickness, and particle size. Fewer than 40 µm for the laser beam diameter, less than 10 µm for the layer thickness, and less than 10 µm for the particle size were specified as the dimensions of the micro SLM scaled by Fischer et al. [180].

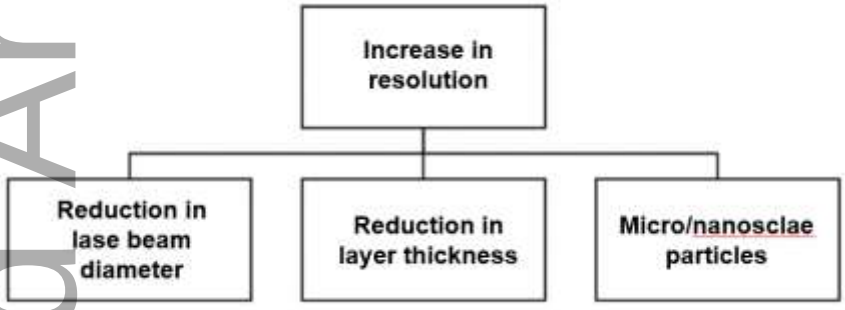

Fig. 14. Prerequisites for micro scale SLM characteristics [159].

Because they must be at least one order shorter than the required layer thickness in order to produce layers that are one micrometer thick, the particles used in the micro system are known as NPs (nano particles). Additionally, in order to achieve a feature resolution of less than 5 µm, it is necessary to use particles that are at least one order of magnitude smaller than the desired feature resolution [45, 181]. Although they have a high surface area to volume ratio [180], nanopowders experience severe agglomeration and oxidation. This causes inadequate sintering of the NPs, which results in poor component quality. At the nanoscale, van der Waals forces start to be stronger than gravity [182]. Agglomeration causes inhomogeneous powder stacking by increasing interparticle friction and decreasing powder flowability [183]. In addition, there is a balling effect and an increase in porosity. Small powder particles pose various challenges when developing micro SLM systems, including agglomeration, and the followings:

- The increased reflectivity of tiny powders minimizes the absorption of laser irradiation.
- Fine powders may evaporate at very high energy densities, causing a fall in part density and a change in chemical composition.
- Additional precautions must be used while handling and transporting the fine powder since it is very receptive to reaction.

Utilizing NP inks that aid in preventing the NPs from agglomerating during the powder spreading process is, therefore, a remedial approach. As a result, a brand-new power layer-by-layer NP coating technique using NP inks was created to manufacture multi-layer structures in the μ-SLS procedure. Several surfactant coatings on NP inks (such as PVP or PEG) keep the NPs from clumping together into larger clusters [45].

The size of the laser spot may considerably impact the micro SLM process features. It is anticipated that the formation of microstructures in micro SLM would be different from that in conventional SLM due to smaller spot sizes, thinner layers, and finer powders. This may lead to a finer microstructure as a result of quicker cooling rates and a more significant temperature gradient in micro SLM, as the spot size is smaller. It is important to note that micro SLM systems employ both CW (continuous wave) and pulsed lasers in this direction. When Regenfuss et al. [184] first built up their laser micro sintering apparatus, they utilized a Q-switched pulsed laser. Using a pulsed wave laser in micro SLS, ceramics and metals have been effectively produced [185]. Due to the lack of heat accumulation, the Q-switched pulsed laser produced a greater resolution for ceramic materials than the CW laser. Despite the successful sintering of a variety of metallic and ceramic materials using a laser micro sintering system with Q-switched pulsed lasers, it is thought that pulsed lasers in micro SLM still have limitations in terms of surface smoothness, melt pool stability, and defects. The use of CW lasers in most recent studies on this topic may be explained by these limitations as well as the extensive use of CW lasers in traditional SLM. The study done on the use of micro SLM/SLS in the processing of metallic materials is summarized in Table 4 [183, 186- 193]

Table 4: A survey of the literature about SLM/SLS approaches for microscale manufacturing [159].

specifications	Regenfuss et al. [184]	Streek et al. [188]	Gieseke et al. [189,190]	Fischer et al. [180, 191]	Robers and Tien [192]
Structural resolution (μm)	<30	15	<50	<40	30
Aspect ratio	>10	NS	30:1	262	NS
Layer thickness (μm)	NS	1-10	20	7	5
Surface roughness (μm)	<3.5	1.5-3.5	8	>7.29	5
Laser specifications	Nd:YAG laser (CW) Power:01-1 W Freq:0.5-50 kHz	Nd:YAG laser (pulsed)	Fiber laser Power:25/50 W	Pulsed laser Power:30 W Freq:1kHz-1MHz	NS
Spot size (μm)	25	25	19.4	30	30
Material	W, Al, Cu, Ag	W, Al, Cu, Ag, 316L, Mo, Ti, 80Ni20Cr	316L	316L	316L and 17-4PH
Powder particle size (μm)	0.3-10	1-10	5-25	3.5	D_{90}, 6
Enviroment	Vacuum (10^{-3}Pa) or reduced shield gas pressures (10^{4}-10^{5}Pa)	Vacuum (10^{-3}Pa)	O_2 <300ppm	Argon (O_2 &H_2O<10ppm)	Argon (O_2 &H_2O<1ppm)
Machine	Customized	Customized	NS	EOSINT μ60	DMP50GP

NS: not specified: Freq: frequency; D_{90}: the diameter of the particle that 90% of the particle distribution is below this value.

The Laserinstitut Mittelsachsen eV employed a Q-switched neodymium-doped yttrium aluminum garnet Nd: YAG Q-switched laser (0.5 to 2 kW) to construct the first micro SLS system more than a decade ago [180]. With a 0.1 m precision, the motors on the construction platform and powder dispenser can precisely regulate the layer thickness in the sub-micrometer range. This ground-breaking technique produced micro parts with a minimum aspect ratio of 10, a surface roughness of 5 micrometres, and a structural resolution of less than 30 micrometres. According to figure 15, powders of tungsten (W), aluminum (Al), copper (Cu), and silver (Ag) were evaluated for this investigation with average particle sizes between 0.3 and 10 µm [192-194]. A special µ-SLS system with a throughput of more than 60mm^3hr^{-1} and the ability to create full 3D metal components with sub-5 µm resolution is provided by Roy et al. [45]. In order to obtain the necessary feature resolution, the microscale powders utilized in traditional SLS methods are transformed to nanoparticle (NP) inks. A digital micro mirror device (DMD) array from Texas Instruments (TI) is used in the µ-SLS system to increase the process's throughput. These tests showed that both FS (femtosecond) and NS (nanosecond) laser sintered spots had considerable NP balling, which causes a low bed density in the finished part and poor sintered part properties. Due to the adaptability of the micro SLS design, it was modified to incorporate a slot die coating system in the enhanced configuration. Slot die coating, using precision metering and controlled dispensing, can deposit a variety of thicknesses from 20 nm to 150 µm. Comparatively, CW laser sintering demonstrated superior sintering quality due to minimal impact from NPs balling up and homogeneous necking between particles throughout the whole spot region. Images of circles with various requisite diameters are shown in optical microscope and surface profile images in Figure 15d-f. This shows how the technology can create 3D pillar structures for IC packing with diameters as tiny as 10 µm and deploy the present laser source over enormous areas. As illustrated in Figure 9(a), Gieseke et al. [194] produced components utilizing shape memory alloys (Ni-Ti) with a resolution of 50 µm. Figure 15g shows how Yadroitsev and Bertrand [195] created microfluidic devices out of stainless steel (SS) 904L using a commercial technology called PM 100. (figure 15h). 70 and 5 µm, respectively, were the spot size and layer thickness measurements. Produced were completely operational parts measuring 100–500 µm and structural pieces 20 µm. Notably, the spot size remained enormous, and the surface roughness was inadequate.

Today, the micro SLS procedure was commercialized as "EOSINT 60" and research in micro SLS/SLM was conducted by 3D MicroPrint GmbH, a firm established by 3D-Micromac AG and EOS GmbH specifically to produce micro SLS equipment for metallic microfabrication. Nagarajan et al. [159] recently created a special powder recoating method that can work with tiny powders for their in-house micro SLM system (Fig. 15i). with the subsequent processing variables: Their micro SLM system, which has hatch spacing of 10 µm, layer thickness of 10 µm, spot size of 15 µm, laser power of 50 W, and scanning speed of 800-1400 mms-1, was used to construct the features in Fig. 15j. The current state of the art allows for a minimal feature size of 60 µm and a minimum surface roughness (Ra) of 1.3 µm. Even yet, the technology can handle submicrometer and nanoscale particles to produce layers that are 1 µm thick. By further lowering the layer thickness and powder particle size, it is possible to achieve a substantially greater feature resolution (< 15µ m) and surface roughness (1 µm) by using the developed

approach. With a surface roughness of less than a millimeter and a feature resolution of less than 15 millimeters, current SLM systems can achieve more than 99 percent component density.

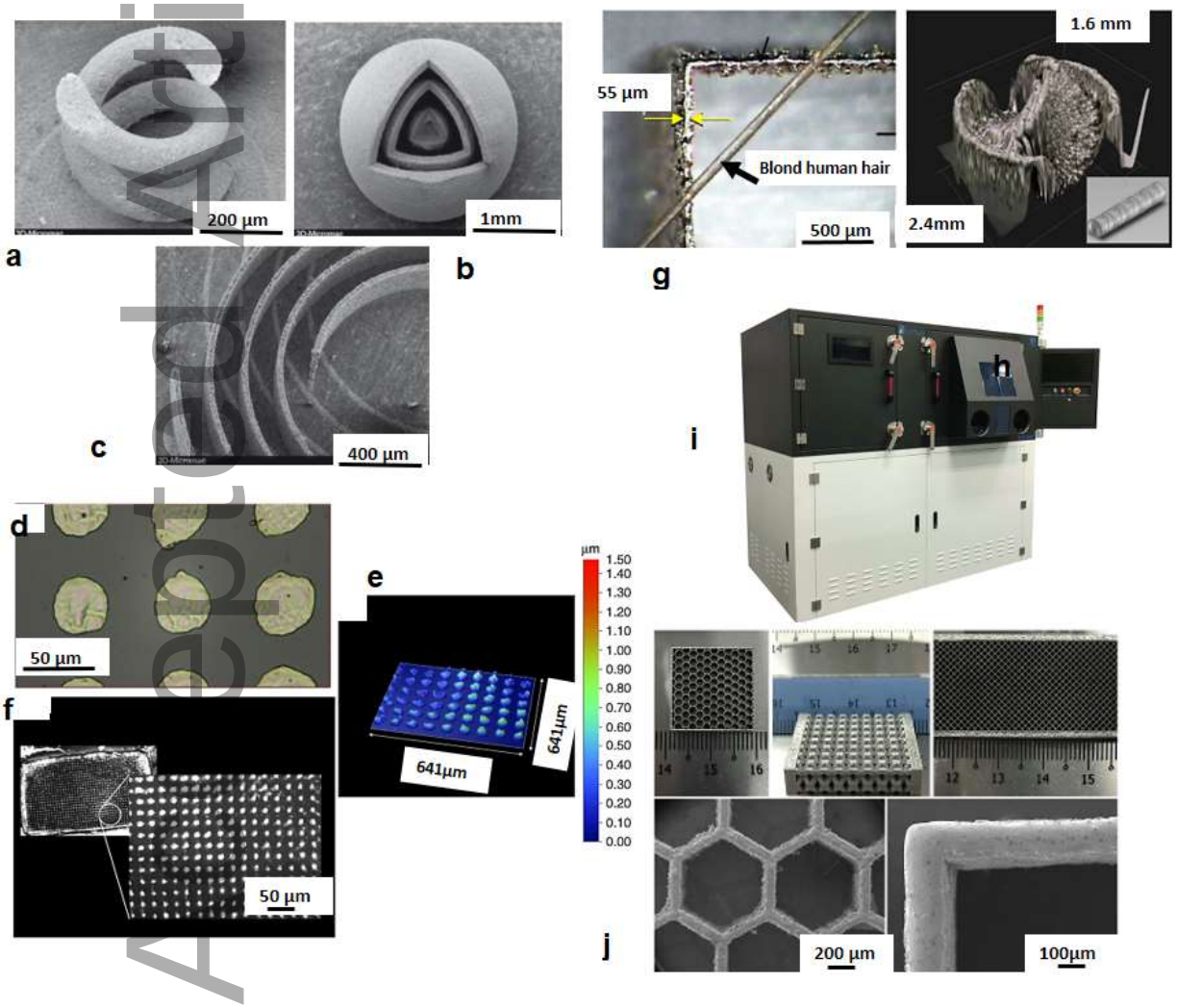

Fig. 15. Laser micro sintering for the fabrication of microfeatures. (a) tungsten powder-based sintered test structures (300 nm size); (b) nesting three hollow spheres; (c) concentric rings [193]. Ag nanoparticle ink produces single layer sintering. d) Image of a circle array under an optical microscope. e) Surface topography of an array circles f) a picture taken using an optical microscope displaying the entire array that was sintered on a 1 µm thick Ag NP ink layer [45]. components made with micro SLM. (g) Ni–Ti micro actuators; (h) SS 904L microfluidic systems in top view, its interior structure is seen in the insert image [194, 195]. i) SIMTech created a micro SLM system; (j) different characteristics manufactured with micro SLM [159].

Despite being a relatively new idea, powder bed fusion for additive production of bulk TEG structures has garnered a lot of interest. Powder bed fusion's capacity to create hierarchical structures is its key advantage. The method can generate inclusions and grain boundaries [196], which enhances phonon scattering and results in reduced thermal conductivity and enhanced charge carrier energy filters to raise the Seebeck coefficient [197]. Low melting temperatures, ductility, thermal conductivity, weak mechanical strengths, and a low thermal shock resistance are characteristics of TE materials, which are semiconductors as opposed to metallic materials [198]. Additionally, TE materials are characterized by poor thermal shock resistance. The chemical composition and brittleness of the finished materials from laser processing of TE materials may vary [199]. Because TE materials are so sensitive to chemical composition, even the slightest deviation could cause an unfavorable shift in conduction and lower TE performance. The right laser energy density must be obtained as a result. Before it was possible to produce a bulk sample using powder bed fusion, significant research on bismuth antimony telluride (BST) was conducted to discover the appropriate process parameters. SLS processing was also used in the synthesis of p-type BST, as reported by Shi, Chen, Jia, and Wang [200]. The manufacturing conditions led to the creation of a porous TE material with a very low thermal conductivity while preserving its electrical capabilities to a large degree; the greatest ZT value, which is greater than that of the commercial bulk BST material, was 1.29. (Fig. 16a-d). The new processing parameters did record a pioneering ZT, but its poorer mechanical qualities make it less suitable for conversion to a real TEG.

Qiu et al. [201] suggested using SLM to make textured $Bi_{0.4}Sb_{1.6}Te_3$ and improve TE properties and compressive strength along the building direction (BD) to make up for the poor mechanical properties of SLS processing. As seen in Figure 16e, the $Bi_{0.4}Sb_{1.6}Te_3$ generated by SLM contained grains with a columnar structure and a strong orientation along the BD. Despite the fact that the microstructures were very perfectly aligned, the printed sample's Seebeck coefficient was only around 112 μVK^{-1}, and its ZT value was only about 0.72. The printed sample was sintered at 673K for 24 hours in order to limit the quantity of anti-site defects, increasing the Seebeck coefficient to 195 μVK^{-1}. As a result, ZT obtained 1.1 at 316K. Strongly oriented microstructures also resulted in a notable improvement in mechanical properties. The maximum compressive strength of the SLM-printed sample is 91 MPa, which is more than that of the zone-melted samples (Figure 16 f). However, porosity was decreased at higher laser intensities of 3-5 W when El-Desouky et al. used SLM with a laser spot size of 300 µm [202]. In a following study, El-Desouky et al. used even stronger lasers and faster scan rates (10–25 W and 350 mm/s), Due to the reduced (70 µm) laser point size, they were nevertheless able to analyses the melt pool and microstructure formation of Bi_2Te_3 discs with comparable volumetric energy intensities. According to SEM imaging, a higher laser power allowed the laser heating to heat the matrix more deeply, creating a deep pool of molten material. In contrast, elevated energy density levels considerably decreased the surface porosities (Fig. 16g). Nonetheless, circular, and irregular subsurface holes continued to form as a result of trapped gases and melting pool boundaries shrinkage [203]. These studies revealed that the Bi_2Te_3 microstructure is a good option for powder bed fusion. The microstructural development of Bi_2Te_3 powder treated with various laser power inputs is shown in Fig. 16h. At increasing power levels, the grains' shape elongates in a direction similar to the build direction.

Skutterudites, half-Heusler alloys, and BST are the best intermediate-temperature TE materials for the SLS/SLM platform. They have high melting points, great mechanical properties, and thermal conductivities that are similar to metals [204-206]. Yan, Ke, Yang, Uher, and Tang's n-type $CoSb_{2.85}Te_{0.15}$ skutterudites were employed to deposit bulk materials directly on a Ti

substrate using an SLM approach [207]. The resultant substance was deposited at 823 K on a Ti substrate and had submicrometer-sized grains and a maximum ZT value of 0.56. The best SLM processing window was found by carefully looking at how different processing settings affected the chemical makeup and overall quality of the printed layers. A surface that deviates from this energy density zone will be porous, unstable, and will ball up, as seen in Figure 16 i–m. Additionally, Zhang et al. used pure ZrNiSn and nano ZrO2 doped $Hf_{0.3}Zr_{0.7}CoSn_{0.3}Sb_{0.7}$ to show the first laser powder bed fusion (SLM) of half-Heusler alloys. According to the findings, TE half-Heusleralloys may be used for powder bed fusion [208].

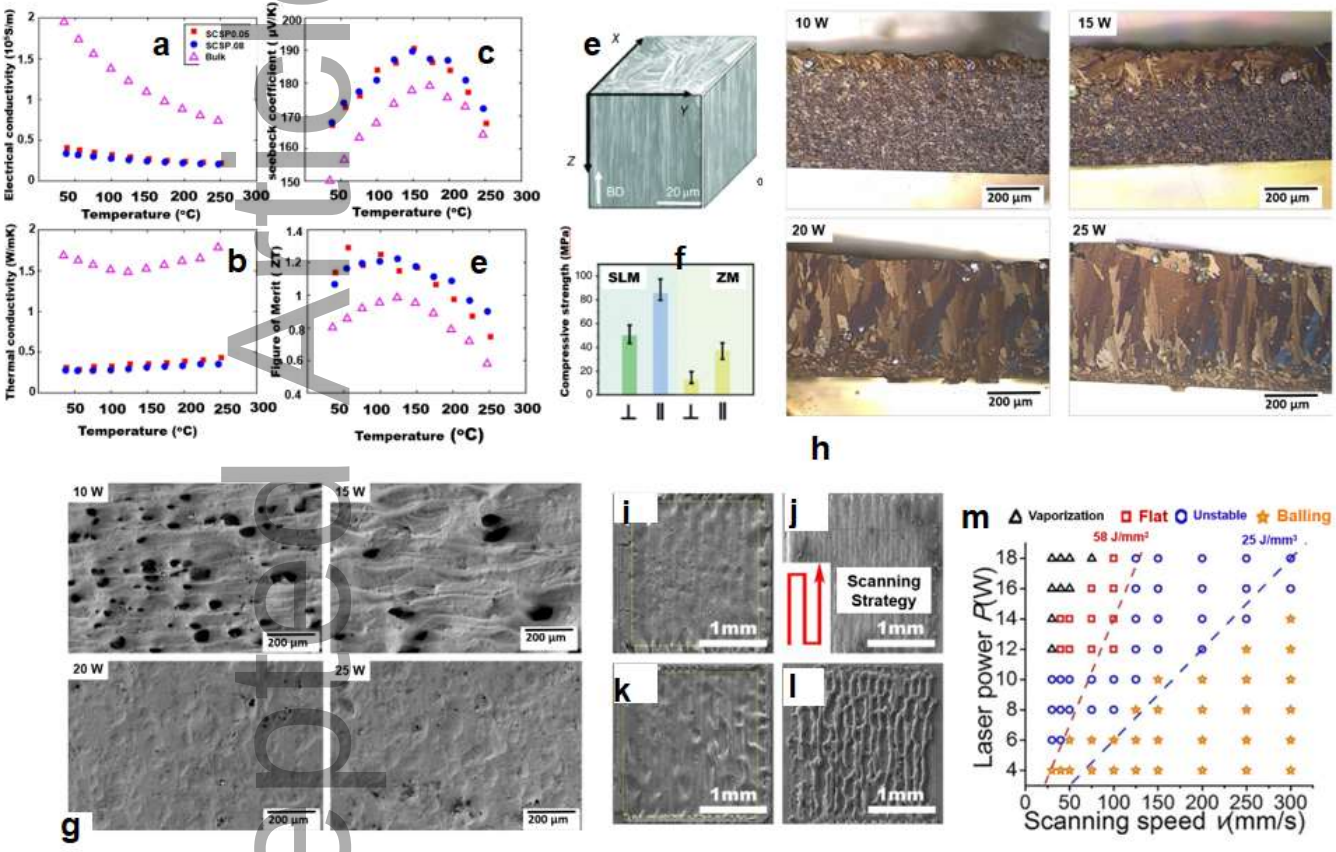

Fig. 16. The impact of temperature on (a) electrical conductivity, (b) Seebeck coefficient, (c) thermal conductivity, and (d) Comparing the sample's zT to commercial bulk (BST bulk) (e) XY, XZ, and YZ plane cross section FESEM images of 3D grain morphologies. (f) Comparing the printed and annealed sample's compressive strength to that of the ZM sample [199-201]. (g) Surface porosity decreases with increasing laser power input, as shown by SEM micrographs of the top surface of Bi_2Te_3 powder compacts that have undergone SLM processing. [202]. (h) Images captured by a polarized light microscope of the surface of Bi_2Te_3 samples cut cross-sectionally and subjected to various laser power inputs reveal elongated microstructures [203]. Four typical surface morphologies of layers created with SLM are shown in SEM pictures: (i) vaporization; (j) flat; (k) unstable; and (l) balling. (m) Window for SLM processing of a single layer of $CoSb_{2.85}Te_{0.15}$ [207].

Power PBF methodologies have seen some innovation. The pre-synthesised TE alloy powder was deposited on a build plate in each of the works thus far mentioned in order to carry out the powder bed fusion experiment. The alloying process itself was carried out using laser-based powder bed fusion in the unique approach that Gascoin et al. [209] published. This allowed for a fabrication technique that required less time to complete since the TE alloy would be created simultaneously when the component was being manufactured. Later, Shi et al. [210] employed

this method to laser scan a pseudo-homogeneous mixture of various elemental powders of Sb and Te twice at scan rates of 200-300 mm/s, 60-100 W laser power, and 50 µm hatch spacing. The components had a high relative density of 99.91 percent and a ZT of 0.4 at 250 °C, according to an X-ray diffraction analysis, as well as the atomic ratios that were essentially stoichiometric. Additionally, there has been a lot of interest in hybrid fabrication of bulk TE components, particularly powder bed fusion-based. To enable multi-material printing for device fabrication, Wu et al. integrated ink-based material extrusion with powder bed fusion [211]. High-temperature synthesis, ball milling, and ink printing were used to create a slurry containing Tween 20, Antifoam AR, and n-type $Bi_2Te_{2.7}Se_{0.3}$. Powder bed fusion was used to treat the deposited slurry at 6 W and 80 mms^{-1}. Using 75 layers of the ink-deposited slurry, which were repeatedly stacked, a composite sample with a thickness of 1.5 mm was created. The highest ZT recorded was 0.3 at 177 °C.

The ability to create extremely dense, unique geometries without needing an extra binder material is powder bed fusion's primary benefit over other processes for TE [212]. Powder bed fusion can also be utilized to create TE material from its component parts without significantly deviating from the intended TE alloy's stoichiometry [210]. Phonon scattering can make the Seebeck coefficients bigger and the thermal conductivity worse because the microstructure isn't uniform and the grains are more likely to be aligned along the temperature gradient [213]. However, high temperatures might cause TE materials to decompose during powder bed fusion. The absence of fusion, porosity, heat cracking, and oxidation are significant barriers. Additionally, the brittleness of TE materials [214, 215] raises thermal cracking danger. Furthermore, any change in the chemical composition will affect TE characteristics. Therefore, a thorough knowledge of the interaction between the material, design, process, and property is necessary due to the process' very complicated physics. In terms of computation, an integrated computational approach will enable researchers to forecast the composition, characteristics, and manufacturing conditions of complex materials before they are ever created. High precision compound property prediction is undoubtedly helpful and speeds up the hunt for novel materials. On the other hand, guess-and-check experimentation approaches tend to have poor sustainability qualities, such as significant material waste and high energy consumption, which require lengthy testing before a suitable solution is found. Additionally, it aids in completely comprehending and optimizing the production process. Fig. 17 depicts the artificial intelligence workflow for computational investigations of materials-design-processes-property, with a focus on the prediction of material characteristics and process parameters.

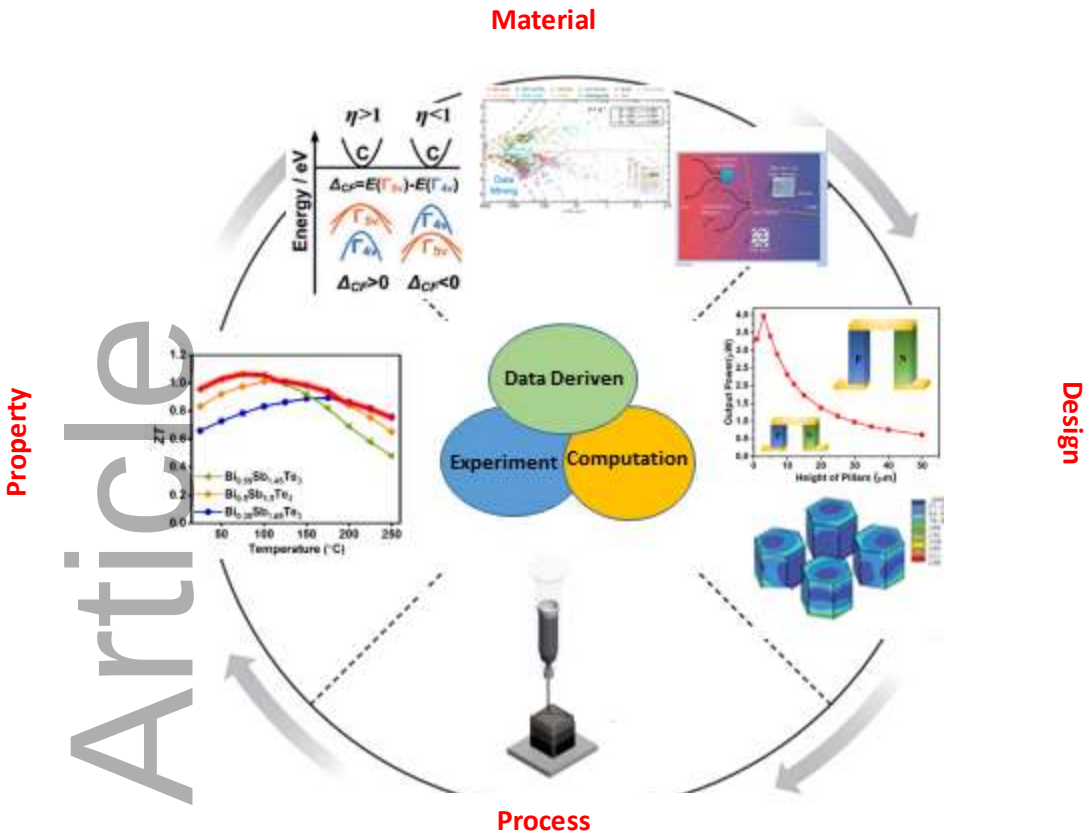

Fig. 17- Integrated computational framework for the development of high ZT and reliable thermoelectric materials [149,117, 247, and 224,225].

As a result, modeling approaches may lessen the need for experimentation while enabling the prediction of the final microstructure [212–223]. With future processing window improvements, it may be possible to create complex, extremely effective TE legs without the need for further post-processing to remove the binder. In conclusion, more work has to be done on the powder bed fusion of TE structures before it can be used as a practical method for producing TE devices.

3.1.2 Direct 3D Writing

3.1.2.1 Material Extrusion

Material extrusion is the most commonly used AM technique because it is affordable and capable of producing a variety of materials, such as composites, ceramics, and polymers [222, 223]. A material must first be deposited onto a substrate, which may be held at a specific temperature, in the form of a filament or viscous ink, before it can be extruded. These procedures include robocasting and dispenser printing. In dispenser printing, ink is applied directly to the substrate from the micrometer nozzle using pneumatic control. Material extrusion is appropriate for printing fully functioning materials with anisotropic properties since it is inexpensive and has the capacity to extrude a wide range of materials (Fig. 18a).

The extrusion pressure, printing speed, nozzle diameter, and distance between the nozzle and the substrate are all examples of processing parameters [176]. Depending on the kind of material that is extruded, there are three commercially licensed methods: direct ink writing (DIW), FDM, and fused filament fabrication (FFF) [226-228].

In order to achieve consistent deposition after material extrusion, rheological modifiers, which may be organic or inorganic, are required. In the process of extruding solid filament-based materials into TE bulk structures, the only binders that have been used up to this point have been organic polymers. In their initial research, Wang et al. customized the TE and mechanical properties of PLA (Polylactic Acid)/BST ($Bi_{0.5}Sb_{1.5}Te_3$) composite filaments at various loadings of multi-walled carbon nanotubes (MWCNTs), silane coupling agent, and plasticizer to achieve a ZT of 0.011 at room temperature [229]. To construct bulk, p-type bismuth telluride (Bi_2Te_3) structures, Oztan et al. used the method suggested by Wang et al. Using organic acrylonitrile-butadienestyrene (ABS) at a weight percentage of 20 percent as a binding agent allowed for the fabrication of bulk cubes with edges measuring 1 millimeter. At room temperature, the highest ZT for the bulk cubes that had been sintered at 500 degrees Celsius was 0.54 [230]. Organic binders are also used in the extrusion of ink-based materials. For the manufacture of bulk Bi_2Te_3 structures, Kenel et al. used an unconventional process that included the extrusion of a material based on ink. The process of heat treatment was used to convert the extruded Bi_2Te_3 + TeO_2 + Poly-lactic-co-glycolic acid (PLGA) ink to the TE form of Bi_2Te_3. The printed samples, despite warping and shrinking, were able to obtain a sufficiently high ZT of 0.4 [231].

Kim et al. [232] used viscoelastic TE inks made entirely of inorganic materials, with Sb_2Te_3 chalcogenidometallate (ChaM) ions acting as the inorganic binders for Bi_2Te_3-based particles due to the low electrical conductivity of organic materials (see fig. 18b). The maximum ZT values for p and n-type samples were 0.9 at 125 degrees Celsius and 0.6 at 175 degrees Celsius, respectively, for bulk samples of cuboid, disc, and half-ring shapes. The extremely soluble ChaM ions' conversion, after heat treatment, into crystalline semiconducting metal chalcogenides was credited with these better ZT numbers. The chalcogenidometallate-based (ChaM) ions, which are anions with metal atoms, are molecular ions linked to chalcogens, were used to replace the electrically insulating polymer matrix [176]. Colloidal nanocrystals of Pb and Bi chalcogenide that were capped with Sb_2Te_3-based ChaM were successfully created using a process developed by Kovalenko and colleagues [233]. Through electrostatic interactions, Sb_2Te_3 ChaM ions significantly enhanced interparticle coupling and stabilized the particles in a solution. In order to enable the 3D printing of high-performance TE material, the special properties of molecular ChaM ions that were identified at the nanoscale have been extended to microscale TE particles. Figure 18c illustrates the ChaM zeta potential curve. The ChaM ions' negatively charged surface was identified by a peak of 23 mV. The negatively charged ChaM ions on the surface of the TE particles operate as a dispersing and stabilizing agent due to the repelling interactions between the particles, resulting in an electrostatically stable dispersion (Figure 18d). The phase separation test in Figure 18 e made the increased colloidal stability obvious. Shape-conformal TE materials were 3D printed thanks to the accurate control of rheological characteristics and optimal ink composition. During the printing and subsequent heat treatment of irregularly shaped structures, Sb_2Te_3 ChaM ions improved the sintering procedure without introducing secondary phases (Figure 18f and g). A material with high mechanical strength was created because of the structural change from

molecular ChaM ions to crystalline phases. n- and p-type samples have electrical conductivities of 500 and 550 S/cm, respectively (Figure 18h). The n-type and p-type printed samples reached their greatest Seebeck coefficients, 145 and 199 μVK^{-1}, respectively, when the temperature was 175 and 200 degrees Celsius (Figure16h). The thermal conductivity of the hot-pressed BST which was significantly higher than printed materials that was found to range between 0.50 and 0.63 Wm^{-1} K^{-1}, according to the measurements taken (Figure 18i). The printed materials featured holes of various sizes, from the nanoscale to the macroscale. The macroscale pores successfully produced phonon scattering, which resulted in very poor thermal conductivity. Due to the electron and hole carriers' incredibly short mean free paths, the electrical carrier transport behavior remained unaltered. ZT values of 0.6 and 0.9 at 170 and 125 °C for n- and p-type TE materials, respectively, were obtained due to the weak thermal conductivity; these results are comparable to those of hot-pressed bulk materials (Figure 18j) [234,17].

Material was extruded into different shapes, such as cubes, cylinders, plates, disks, perforated plates, and tubes, which were then sintered without a big change in their mechanical properties. Using material extrusion and just inorganic inks, it has also been said that the topology of printed bulk TE legs can be optimized. Choo et al. showed a hollow hexagonal column and honeycomb-shaped bulk TE (Cu_2Se) structures with ZTs as high as 1.21 at 727 °C due to Se82- polyanions serving as a sintering-promoting agent (Figure 18k). Additionally, compared to the cuboid legs, the modified legs showed an improvement in power density of between 20 and 25 percent, which was also supported by simulation [33]. Yang et al. [235] describe the multi-material 3D printing of geometrically controlled, composition-segmented multi-BiSbTe composites by successively stacking different viscoelastic TE inks (Fig. 18l). They developed all-inorganic TE inks including chalcogenidometallate (ChaM) inorganic binders based on $Sb_2Te^{-2}_4$ and with carefully controlled BiSbTe particle compositions (Fig. 18m). At 75 °C, it was discovered that $Bi_{0.55}Sb_{1.45}Te_3$ had the highest ZT of 1.06. The 3D-printed materials clearly demonstrate how composition engineering was used to generate the segmented BiSbTe ZTs' peak shift from room temperature to 250 °C. They were successful in using successive printing techniques to create TE legs with composition segments by raising the peak ZTs of the TE legs from room temperature to 250 °C. (Fig. 18n). Kim et al. [236] demonstrate that direct printing with particle-based TE inks can be used to create microscale three-dimensional TE devices. A designed particle based on $(Bi, Sb)_2(Te, Se)_3$ is utilized to make colloidal inks with strong viscoelasticity and no organic binders. The complicated structures are then directly written with the inks utilizing a 3D printing technique. The produced structures have TE figures of merit that are similar to those of bulk ingots, 1.0 for the p-type and 0.5 for the n-type. Micro-thermoelectric generators are created by printing vertical filaments in three dimensions that have a significant temperature gradient. As a result of the high anisotropy of the TE legs, the generators have an output power of 2.8 W at a temperature differential of 82.9 °C and a power density of 479.0 W cm^{-2}.

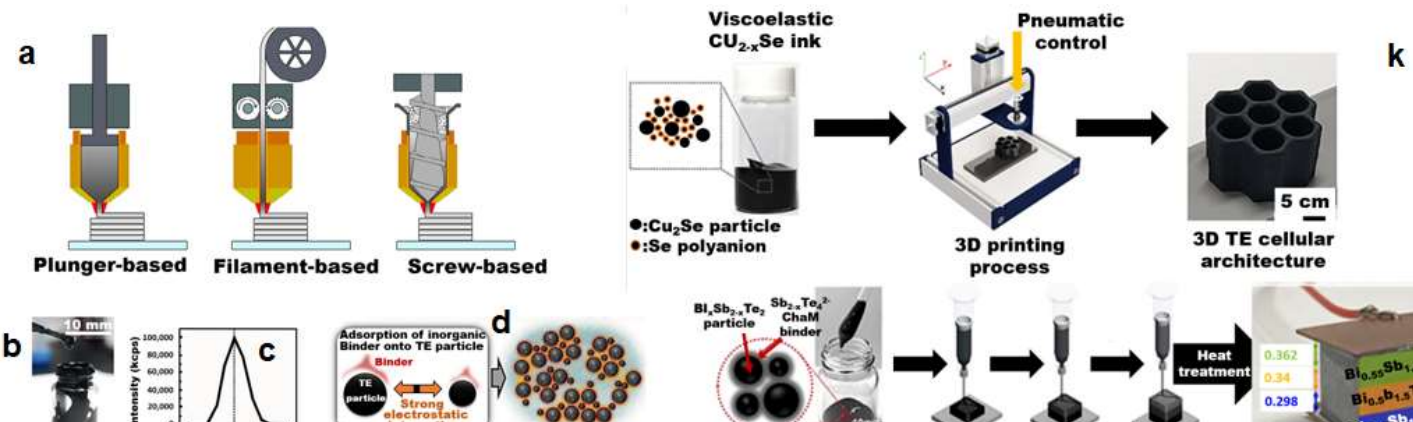

Fig. 18. (a) Diagram illustrating how material extrusion operates [215] (b) Bi_2Te_3-based TE ink images with ChaM (c) ChaM ions' zeta potential curve (d) Schematic representation of increased electrostatic interaction and polar energy of TE particles. A comparison of images showcasing TE ink based on Bi_2Te_3 (e) with ChaM and without ChaM. (f) images of printed materials in a range of shapes. (g) SEM images of the sintered materials produced by TE inks using Bi_2Te_3 without and with ChaM. n-type and p-type 3D-printed materials' temperature-dependent TE characteristics: electrical conductivity and absolute Seebeck (h) coefficient (i) thermal conductivity (j), and ZT [245,17] (k) a Plan for the 3D printing of the Cu_2Se-based honeycomb cellular design utilizing only inorganic materials $Cu_{2-x}Se$ ink. Compositionally segmented TE leg 3D printing schematic illustration using multiple materials [33]. (l) The diagram illustrates sequential 3D printing of multi-segmented TE materials. Green (Top), orange (Middle), and blue (Bottom) Multi-material 3D printing with TE inks containing $Bi_{0.55}Sb_{1.45}Te_3$, $Bi_{0.55}b_{1.5}Te_3$, and $Bi_{0.35}Sb_{1.65}Te_3$ particles, comprising colored patterns corresponds to each block in the compositionally segmented TE legs, respectively. (m) photographs of TE inks made entirely of inorganic materials containing $Bi_xSb_{2-x}Te_3$ particles (x = 0.3–0.6). (n) ZT values that vary with temperature. construction and power output of the μ-TEG [33].

Due to its scalability, flexibility, affordability, simplicity, and versatility, material extrusion, like the most common AM process, may be used with a range of materials. There have been several TE ink and filament formulations created thus far using organic, inorganic, and hybrid materials. In order to cure the ink and increase the part's tensile strength, a heat treatment phase is necessary when extruding ink-based materials. This heat treatment process makes the microstructure more porous, which lowers electrical conductivity and results in ZTs that are less dense than their bulk counterparts. It is necessary to have a high colloid volume fraction of TE particles in order to reduce volume shrinkage and voids that are generated during the breakdown of the binders and to have the highest possible thermal power and the best possible quality of the material that is created [175]. The heat treatment step, which also causes warping, shrinking, and other geometric anomalies in the legs, may be the method's major fault. The process parameters for the heat treatment phase must be carefully chosen considering all of these variables. Danaei et al. used intense flash of UV light to sinter bismuth telluride-based nanoparticles TE film within milliseconds [237]. On the other hand, the groundbreaking discovery of ChaM as an inorganic binder with good electrical and rheological properties has led to the development of material extrusion into a technology that offers a variety of potential for AM of vertical μ-TEG structures.

5-Visions and Future Directions

Significant work has been done over the past 20 years to develop the vertical μ-TEG from a prototype to a functional coproduction to power low-power electronics. The main drawback is the low output power, which falls short of meeting the actual power requirements of most devices. Geometrical constraints, a low ZT value for TE materials, contact resistance between semiconductor and metal, and a low thermal resistance of vertical-TEG from hot to cold side are all influencing factors. The inadequate TE characteristics of the available materials are the fundamental impediment to the development of μ-TEG. Recently, nanostructured materials have attracted much interest and are believed to be a strong contender to overcome the TE field's bottleneck and increase the ZT value. The development of micro-AM-compatible printable TE material is another serious challenge. Moreover, it is necessary to point out how vital material costs are for the practical uses of μ-TEG.

Owing to the enormous possibility for TEG efficiency and reliability improvement, the current focus of research is on structural optimization and μ-TEG geometry. In a μ -TEG device, optimizing leg length, leg cross-sectional area, and number of TE legs are advocated. Additionally, it has been claimed that asymmetrical TE legs function better than traditional rectangular/symmetrical legs because they transmit heat more effectively. Another crucial factor in the design and geometry optimization of μ-TEG is the heat resistance of the μ-TEG package. The length and aspect ratio of the μ -TEG legs significantly impact the heat resistance of vertical structures. Due to the hot and cold sides of μ-TEG's low thermal resistance, an increase in thermal resistance typically results in higher output power. As a result, enhancing μ-TEG's heat resistance is essential. The purpose of the μ-TEG design is to have a high overall thermal resistance. FEM and multi-objective optimization techniques have been used to optimize geometry and structures. Thermoelectric geometry can be effectively optimized by considering the device's electrical and mechanical efficiency using multi-objective optimization and the three-dimensional finite element/volume method, in which temperature and thermal stress distributions may be mapped out in detail to identify the locations of high stress. It could offer precise temperature and thermal stress distributions to identify high-stress spots. In order to improve electrical and mechanical performance, it is advised that future research concentrate on merging three-dimensional and multi-objective optimization of geometry. However, there is little to no actual research on how TE geometry affects the dependability of the TEG's electrical and mechanical systems. Consequently, further experimental work combined with numerical optimization must be carried out and advised to improve the likelihood that μ-TEGs will be commercialized. A strong framework for designing TEG would be made possible by combining three-dimensional finite optimization with multi-objective optimization employing research efforts.

It seems necessary to use micro-AM techniques to manufacture topology-optimized, high aspect ratio μ -TEGs. Micro AM yields better consequences despite technique-specific restrictions. By integrating AM technologies with advanced materials and digital freeform design, AM can transform the architected material concept into μ-TEG area. Architected materials with ideally planned topologies (cellular or completely dense, single or multiphase, periodic or functionally graded) exhibit several distinguishing characteristics. Specifically, they make it possible to decouple features such as thermal conductivity and the Seebeck coefficient. In order to implement this concept, it has been advised to use extrusion-based processes with all-inorganic binders in most materials that have produced record-high ZT values. However, powder bed fusion produces components with hierarchical structuring and preferred grain alignment that may improve ZT by suppressing heat conductance. This approach is advised as a prospective study topic. Furthermore, powder bed fusion allows the TE material powder to be processed without needing binders. Due to the scarcity of

photocurable polymers, the vat polymerization approach has received much less attention than alternative techniques. Vat polymerization of bulk TE structures might benefit from further investigation into innovative composite resins. Lastly, AM processing factors may substantially affect the printed microstructure and functionality of the resulting items. Consequently, AM necessitates the construction of a relationship between process-structure-property-performance. Machine-learning approaches may assist in numerous areas of AM, based on the current availability of a large dataset, the high processing power, and the complexity of the design algorithm. A major worry for industrialization would be the reduced mechanical endurance of TE legs produced using 3D printing compared to TE legs produced using traditional fabrication methods because of their lower density.

6-Conclusions

The μ-TEG possesses the potential to substitute conventional batteries due to the advantages of its least moving parts, extended lifetime, no maintenance, compact size, and high output voltage. However, its application in microelectronics seems not to be not simple. Despite the benefits of vertical μ-TEG devices, the general use of TE technology in miniature scale has been hindered by the inefficiency of vertical μ-TEG devices, high material costs, and microfabrication limitations. As a result, many studies are being conducted on vertical μ-TEG geometry and material optimization. The difficulty of employing such TE microdevices for extensive commercial applications is strongly linked to the materials, designs, and production techniques. Existing basic investigations in nanoscience attempt to push such restrictions to increase the TE figure of merit of the material. Unlike conventional TEG, vertical μ-TEG typically operates at modest temperature differences; therefore, electrical and thermal parasitic resistances seem extremely serious. These must be considered while designing vertical μ-TEG and its packaging. Complex 3D geometries, such as layered structures with varying cross-sectional areas across the leg length and TE modules, might create larger thermal resistances and generate electrical power, as well as better structural integrity, as demonstrated by the design and structure optimization of vertical μ-TEG leg geometries. According to the data, TE legs containing inner voids and hierarchical designs have promising importance. Three-dimensional finite element model and multi-objective optimization were considered the basic design and optimization methodologies for thermoelectrics. Nevertheless, obtaining legs with complicated geometry using conventional, subtractive manufacturing techniques is challenging. The technological issue may be resolved using micro additive manufacturing (AM), which makes it possible to create components with small and complicated characteristics. The most recent advances in additively built TEGs were discussed. The latest research on micro additive manufacturing illustrates the promise of this fabrication method and opens up greater possibilities and flexibility for TE technology. A significant advancement in the vertical μ-TEGS in local energy supply implementations, including wireless sensor networks, remote actuators, or cutting-edge micro/nano devices, might be created if nanostructured materials, design, and micro-AM are appropriately combined. Key enabling technology for producing architected materials that make transition from “μ-TEGS" to "microarchitecture TEGs" is the interaction between micro-AM and digital design.

7. Refrences

1. D. Dávila, A. Tarancón and L. Fonseca, Springer International Publishing AG 2018.

2. Y.Tan, S.Panda, InTech U.S. Department of Energy Critical materials strategy, Technical report, 2010.

3. Y. Liu, E. Mu, Z. Wu, Z. Che, F. Sun, X. Fu, F.Wang,X. Wang and Z. Hu, nano Convergence, 2020, 7, 8.

4. P-H. Kao, P-J. Shih, C-L. Dai, and M-C. Liu, Sensors 2010, 10, 1315-1325.

5. C. Hadjistassou, E. Kyriakides, J. Georgiou, Convers Manage. 2013, 66(66), 165–172.

6. J.R. Lim, J.F. Whitacre, J.-P. Fleurial, C.-K. Huang, M.A. Ryan, N.V. Myung, adv. Mater. 2005, 17, 1488-1492.

7. L.D. Hicks, M.S. Dresselhaus, Phys. Rev. B, 1993, 47(19), 12727–12731.

8. L.D. Hicks, M.S. Dresselhaus, Phys. Rev. B, 1993, 47(24), 16631–16634.

9. R. Venkatasubramanian, E. Siivola, T. Colpitts, B. O'Quinn, Nature, 2001, 413(6856), 597–602 (2001)

10. H. Lee, G. Anoop, H. Lee, W.S. Kim, J. Jo, RSC Advances , 2019, 9, 11595–11601.

11. M.S. Dresselhaus, G. Chen, M.Y. Tang, R.G. Yang, H. Lee, D.Z. Wang, Z.F. Ren, J.-P. Fleurial, P. Gogna, Adv. Mater. , 2007, 19(8), 1043–1053.

12. T. Sun, M.K. Samani, N. Khosravian, K.M. Ang, Q. Yan, B.K. Tay, H.H. Hng, Nano Energy, 2014, 8(9), 223–230 (2014).

13. S. Sumithra, N.J. Takas, D.K. Misra, W.M. Nolting, P.F.P. Poudeu, K.L. Stokes, Adv. Energy Mater., 2011, 1(6), 1141–1147 (2011).

14. M. Strasser, R. Aigner, C. Lauterbach, T. F. Sturm, M. Franosch, and G. Wachutka, Sens. Actuators A, Phys.,2004, vol. 114, nos. 2–3, pp. 362–370.

15. S. M. Yang, T. Lee, and C. A. Jeng, Sens. Actuators A, Phys., 2009, vol. 153, no. 2, pp. 244–250.

16. S.El. Oualid, F. Kosior, A. Dauscher, C. Candolfi, G. Span, E. Mehmedovic, J. Paris, B. Lenoir, , Energy & Environmental Science, 2020, 10.

17. F. Kim, B. Kwon, Y. Eom, J. E. Lee, S. Park, S. Jo, S. H. Park, B-S Kim, H. J. Im, M. H. Lee, T. S. Min, K. T. Kim, H. G. Chae, W. P. King & J. S. Son, Nature Energy volume, 2018, 3, pages301–309 (2018).

18. R.He,G. Schierning,K. Nielsch, adv.mater.tech, 2018, 3, 4.

19. S.Pelegrini, A.Adami, C.Collini, P.Conci, L.Lorenzelli, A.Pasa A, Proceedings of the SPIE, 2013, 8763, 8763 E22pp.

20. A.Z. Sahin, B.S. Yilbas, Energy Convers. Manag. 2013, 65, 26–32,

21. Y. Thimont, S. LeBlanc, J. Appl. Phys., 2019, 126, 95101.

22. U. Erturun, K. Erermis, and K. Mossi, Appl. Therm. Eng., 2014, 73, 1, 128.

23. U. Erturun and K. Mossi, Appl. Therm. Eng., 2015, 85, 304.

24. B.S. Yilbas, S.S. Akhtar, A.Z. Sahin, Energy, 2016, 114, 52–63

25. R. Lamba, S.C. Kaushik, S.K. Tyagi, Int J Energy Res. 2017, 1–15.

26. C.WH, W. PH, L.YL. , Appl Energy 2018; 209:211–23.

27. W-H.Chen, Y-B.Chiou , Appl Energy, 2020, 274,115296.

28. J-H.Meng, H-C.Wu, L.Wang, G.Lu, K.Zhang, W-M.Yan. , Appl Therm Eng 2020; 179, 115721.

29. MM.Najafabadi, F.Villanustre, TM.Khoshgoftaar, N.Seliya, R.Wald, E.Muharemagic , J Big Data 2015; 2:1–21.

30. A.Voulodimos, N.Doulamis, A.Doulamis, E.Protopapadakis, Comput Intell Neurosci, 2018, 2018, 1–13.

31. AB.Nassif, I.Shahin, I.Attili, M.Azzeh, K.Shaalan , IEEE Access, 2019, 7,19143–65.

32. K.Zhao, P.Qiu, Q.Song, AB.Blichfeld, E.Eikeland, D.Ren, Mater Today Phys, 2017, 1, 14–23.

33. S.Choo, F.Ejaz, H.Ju, F. Kim, J.Lee , S. Eun Yang, G. Kim , H. Kim , S.Jo, S.Baek, S. Cho, K. Kim, J-Y. Kim , S.Ahn, H. G. Chae, B.Kwon, J. Sung Son, Cu_2 Se-based thermoelectric cellular architectures for efficient and durable power generation, Nature Communications, 2021, 12, 355034. Y.Ge, Z.Liu, H.Sun, & W.Liu, Optimal design of a segmented thermoelectric generator based on three-dimensional numerical simulation and multi-objective genetic algorithm. Energy, 2018, 147, 1060–1069 Z. Sahin, & B. S. Yilbas, Energy Convers. Manag. , 2013, 65, 26–32.

36. U.Erturun, K. Erermis, & K. Mossi, Effect of various leg geometries on thermo-mechanical and power generation performance of thermoelectric devices. Appl. Therm. Eng., 2014, 73, 128–141.

37. M.Picard, S.Turenne, D.Vasilevskiy, & R. A. Masut, , J. Electron. Mater. , 2013, 42, 2343–2349.

38. S.Ferreira-Teixeira, & A. M. Pereira, Energy Convers. Manag. 2018,169, 217–227.

39. M.Vaezi, H.Seitz& S. Yang, A review on 3D micro-additive manufacturing technologies. Int. J. Adv. Manuf. Technol. , 2013, 67, 1721–1754

40. F. Kim, S. Eun Yang, H. Ju, S. Choo, J. Lee, G. Kim, S. Jung, S. Kim, C. Cha, K. Tae Kim, S. Ahn, H. Gi Chae and J. Sung Son, Nature Electronics, 2021, 4,579–587.

41. M.M.Mallick, L. Franke, A. Georg Rosch, and U.Lemmer, ACS Energy Lett. 2021, 6, 85−91.

42. R.He, G.Schierning, K.Nielsch, , Adv. Mater. Technol. 2018, 3, 1700256.

43. N.Jaziri A.Boughamoura, J.Müller, B.Mezghani, F.Tounsi, M.Ismail, a Comprehensive Review of Thermoelectric Generators: Technologies and Common Applications. Energy Reports. Energy Reports, 2020, 6(7):264-28744. S.LeBlanc, Sustain. Mater. Technol. 2014, 2, 26−35.

45. K.R.Nilabh , B.Dipankar , G.D.Obehi, S. F.Chee and M. A. Cullinan,, , Microsystems & Nanoengineering, 2019,5, 64

46. Wohlers Associates Publishes 23rd Edition of Its 3D Printing and Additive Manufacturing Industry Report | Wohlers Associates, 2018.

47. Wohlers Report 2018: 3D Printer Industry Tops $7 Billion. https://www.forbes. com/sites/tjmccue/2018/06/04/wohlers-report-2018-3d-printer-industry-rises- 21-percent-to-over-7-billion/#5c639f592d1a ,2018.

48 L.Hirt, A.Reiser, R.Spolenak, & T.Zambelli, 20171604211.

49. Y. Thimont, S.LeBlanc, The impact of thermoelectric leg geometries on thermal *resistance,* J. Appl. Phys., 2019,126, 095101.

50.A.ElDesouky, M.Carter, M.Mahmoudi, A.Elwany, andS.LeBlanc , Journal of manufacturing Processes, 2017,25,, 411-417.

51. H.Zhang, D.Hobbis, G.S.Nolas, andS.LeBlanc, “Laser additive manufacturing of powdered bismuth telluride,” J. Mater.Res., 201833(23), 40314039.52. M.J.Carter, A.El-Desouky,M.A.Andre, P.Bardet, and S.LeBlanc, “Pulsed laser melting of bismuth telluride thermoelectric materials,” J. Manuf.Process. 2019, 43, 35- 46.

53. A.El-Desouky, M.Carter, M.A.M.A.Andre, P.M.P.M.Bardet, and S. LeBlanc, “Rapid processing and assembly of semiconductor thermoelectric materials for energy conversion devices, Mater.Lett” 2016, 185, 598602.

54. K. Wu, Y.Yan, J.Zhang, Y.Mao, H. Xie, J. Yang, Q. Zhang, C.Uher, X. Tang,, , Phys.Status Solidi RapidRes.Lett. , 2017, 11(6), 1700067.

55. Y.Mao, Y. Yan, K.Wu, H. Xie, Z. Xiu, J.Yang, Q.Zhang, C. Uherc and X.Tang, RSC Adv., 2017,7(35), 2143921445.

56. Y.Thimont, L.Presmanes, V.Baylac, P.Tailhades, D.Berthebaud, and F.Gascoin, , Mater. Lett., 2018, 214, 236239.

57. H. Zhang, S.LeBlanc, S.Wang, J.Yang,andP.Taylor, , Proc.SPIE, 2018, 10663, 106630B.

58. Y.Yan, H.Ke, J.Yang,C.Uher, andX.Tang, , ACSAppl. Mater.Interfaces, 2018 10(16), 1366913674.

59. M.He, Y.Zhao, B. Wang, Q. Xi, J.Zhou, Z.Liang,, Small 2015,11, 5889–5894.

60. N.Su, P.Zhu, Y.Pan, F.Li & B. Li, , Energy, 2020, 195, 116892.

61. Y. Du, J. Chen, Q.Meng, J.Xu, B. Paul, P.Eklund, J. Materiomics , 2020,6, 293–299.

62. J. Qiu, Y.Yan, T. Luo, K.Tang, L.Yao, J.Zhang, M.Zhang, X.Su, G.Tan, H. Xie, M.G. Kanatzidis, C.Uher and X. Tang ,, Energy Environ. Sci. 2019, 12, 3106–3117.

63. C.Oztan, S.Ballikaya, U.Ozgun, R.Karkkainen, & E.Celik,Appl. Mater. Today, 2019, 15, 77–82.64. S. Jo, S.Choo, F. Kim, S. H. Heo, & J. S. Son, Adv. Mater. 2019, 31, e1804930 ().

65. Y. Yun Aw, C. Keat Yeoh, M. Asri Idris, P.Leng Teh, K Amali Hamzah and S. Aqzna Sazali , 2018, Materials 11, 466.

66. S. Kim, D. Hyeog Kim, W. Kim, Y. Tae Cho & N. X. Fang, International Journal of Precision Engineering and Manufacturing-Green Technology, 2021,8, 303–326.67. C.Parra-Cabrera, C.Achille, S.Kuhn, & R.Ameloot, (). , Chemical Society Reviews, 2018, 47(1), 209–230.

68. J. U.Surjadi, L.Gao, H.Du, X.Li, X.Xiong, N. X.Fang, Advanced Engineering Materials, 2019, 21(3), 1800864.

69. L.Valdevit, J. Bauer, "FABRICATION OF 3D MICRO-ARCHITECTED/ NANO-ARCHITECTED MATERIALS", in book: Three-Dimensional Microfabrication Using Two-Photon Polymerization, 2016, edition 1st, chapter: 13.1, 345-373.

70 S.Zhu, Z.Fan, B.Feng, R.Shi, Z.Jiang, Y. Peng, J. Gao, L. Miao and K. Koumoto," Energies, 2022, 15, 3375.

71. J. Snyder, J. R. Lim, C.-K. Huang, and J.-P. Fleurial,Nature Mater.,2003, 2,528–531.

72. J. F. Li, S. Tanaka, T. Umeki, S. Sugimoto, M. Esashi, and R. Watanabe, Sens. Actuators A, Phys., 2003, 108,1– 3, 97–102.

73. H. Bottner, J. Nurnus, A. Gavrikov, G. K uhner, M. J agle, C. K unzel, D. Eberhard, G. Plescher, A. Schubert, K.H. Schlereth, J. MEMS 13 (2004) 414–420.

74. W. Glatz, E. Schwyter, L. Durrer, and C. Hierold, J. Microelectromech. Syst., 2009, 18, 3, 763–772.

75. S. Elyamny, E.Dimaggio, S. Magagna, D. Narducci, and G. Pennelli, Nano Lett. 2020, 20, 4748-4753

76. Y. Li, K. Buddharaju, B. C. Tinh, N. Singh, and S. J. Lee, "Improved vertical silicon nanowire based thermoelectric power generator with polyimide filling," IEEE Electron Device Lett., 2012, 33,5, 715–717.

77. j. Nurnus, B, Habbe, , SENSOR+TEST Conferences 2011, 397 - 398

78. R.Venkatasubramanian, C.Watkins, C.Caylor, G.Bulman, In: PowerMEMS 2006. The 6th international workshop on micro and nanotechnology for power generation and energy conversion applications, 1–4.

79. Y. Li, K.Buddharaju, N.Singh, S.Lee, J Electron Mater, 2012, 41, 989–992.

80. A.Hochbaum, R.Chen, R.Delgado, W.Liang, E.Garnett, M.Najarian, A.Majumdar, P.Yang,Nature, 2008, 451(7175),163–167.

81. A.Boukai, Y.Bunimovich, J.Tahir-Kheli, J-K.Yu, W.Goddard, J.Heath,Nature, 2008, 451(7175),168–71.

82. M.Lindeberg, H.Yousef, H.Rödjegård, H.Martin, K. Hjort, J Micromech Microeng, 2008, 18(6), 065021.

83. D.Liang, H.Yang, S W.Finefrock and Y.Wu,Nano Lett. 2012, 12, 2140.

84. D. Dávila, R. Huber and C. Hierold, Journal of Physics: Conference Series 660 (2015) 012101.

85. V. Leonov, Y.van Andel, Z.ang, R. J. M. Vullers and C. Van Hoof, IFSA Publishing, Sensors & Transducers, 2011, 127,4, 15-26.

86. Z. Wang, Y. van Andel, M. Jambunathan, V. Leonov, R. Elfrink, and R. J. M. Vullers, J. Electron. Mater. 2011, 40, 5, 499–503..

87. X.Yu, Y.Wang, Y.Liu, T.Li, H. Zhou, X. Gao, F.Feng, T.Roinila and Y.Wang, J. Micromech. Microeng., 2012, 22, 10, 105011.88. X. Yu, D. Xu, Y.Liu, H. Zhou, Y. Wang, X. Gao, F. Feng, Y. Wang, T. Li , Int. J. Elect. Power Energy Syst., 2015, 67, 417–422.

89. I. Ohkubo, M. Murata, M.S.L. Lima, T. Sakurai, Y. Sugai, A. Ohi, T. Aizawa, T. Mori, Materials Today Energy, 2022, 28, 101075

90. J.Su, V.Leonov, M.Goedbloed, Y.van Andel, M.de Nooijer, R.Elfrink, Z.Wang, R. Vullers , J Micromech Microeng. 2010, 20(10):104005.

91. Y.van Andel, M.Jambunathan, R.Vullers, V.Leonov , Microelectron Eng, 2010, 87(5–8):1294–1296

92. V.Leonov, C.Van Hoof, R.Vullers, In: IEEE (ed) Sixth international workshop on wearable and implantable body sensor networks, 2009. BSN IEEE, 195–200.

93. D.Dávila, A.Tarancón, M.Fernández-Regúlez, C.Calaza, M.Salleras, A.San Paulo, L.Fonseca , J Micromech Microeng, 2011, 21(10),104007.

94. D.Dávila, A.Tarancón, D.Kendig, M.Fernández-Regúlez, N.Sabaté, M.Salleras, C.Calaza, C.Cané, I.Gràcia, E.Figueras, J.Santander, A.San Paulo, A.Shakouri, L.Fonseca , J Electron Mater 2011, 40(5),851–855

95. D. Dávila, A. Tarancón and L. Fonseca, Commercialization of Nanotechnologies–A Case Study Approach, Springer International Publishing AG 2018.

96. D.Dávila, A.Tarancón, C.Calaza, M.Salleras, M.Fernández-Regúlez, A.San Paulo, L.Fonseca, J Electron Mater, 2013, 42(7), 1918–1925.

97. A.Perez-Marín, A.Lopeandía, L.Abad, P.Ferrando-Villaba, G .Garcia, A.Lopez, F.Muñoz-Pascual, J.Rodríguez-Viejo , NanoEnergy, 2014, 4,73–80.

98. M. Maksymuk, 2021, 21, 100753.

99. E. E. Aktakka, N. Ghafouri, C. E. Smith, R. L. Peterson, M. M. Hussain, and K. Najafi, , IEEE Electron Device Lett., 2013, 34, 1334.

100. S. Yazdani and M., Nanotechnology, 2018, 29, 432001.

101. C.J. An, Y.H. Kang, A-Y. Lee, K-S.Jang, Y. Jeong, S. Y. Cho, ACS Applied Materials & Interfaces, 2016, 8, 34, 22142-22150.102. R. Venkatasubramanian, Cynthia B Watkins G. Bulman , In Proceedings of PowerMEMS, 2006, 1 – 4.

103. D. M. Rowe, Boca Raton, FL, USA: CRC Press, 2005.

104. M. Strasser, R. Aigner, M. Franosch, and G. Wachutka, Sens. Actuators A, Phys., 2002, 97–98, 535–542.

105. M. Strasser, R. Aigner, C. Lauterbach, T.F. Sturm, Conference: TRANSDUCERS, Solid-State Sensors, Actuators and Microsystems, 12th International Conference on, 2003, Volume: 1.

106. Z. Wang, V. Leonov, P. Fiorini, and C. Van Hoof, Sens. Actuators A, Phys., 2009,156, 1,95–102.

107. T. Huesgen, P. Woias, and N. Kockmann, Sens. Actuators A, Phys., 2008,145–146, 423–429.

108. S. M. Yang, T. Lee, and C. A. Jeng, Sens. Actuators A, Phys., 2009, 153, 2, 244–250..

109. S. M. Yang, T. Lee, and M. Cong, Sens. Actuators A, Phys., 2010, 157, 2, 258–266.

110. S. M. Yang, M. Cong, and T. Lee, Sens. Actuators A, Phys., 2011, 166, 1, 117–124,

111. K.Ziouche,Z.Yuan, P. Lejeune, T. Lasri, D. Leclercq, andZ. Bougrioua, , J. Microelectromech. Syst. 2017, 26, 1, 45–47.

112. S. Shittu, G. Li, X. Zhao, X. Ma, Applied Energy, 2020, 268, 115075.

113. Q. Wang, W. Wang, L. Sun, P. Jiang, Materials Today Energy, 2023, 34, 101282.

114. S.Shittu, G.Li, X.Zhao, YG.Akhlaghi, X.Ma, M. Yu, Energy Convers Manag, 2019, 193, 1–14.

115. TH.Kwan, X.Wu, Appl Energy, 2016, 165, 297–307.

116. JY.Jang, YC.Tsai, Appl Therm Eng, 2013, 51,677–89.

117. A. Tanwar, S. Lal and K. M. Razeeb, Energies, 2021, 14, 2339.

118. S.Kumar, SD.Heister, X.Xu, JR.Salvador J Electron Mater, 2015, 44,3627–36.

119. T. Shih and T. Hogan, 2005, 1223.

120. H. Tian, X.Sun, Q .Jia, X.Liang, G.Shu, X.Wang , Energy,2015, 84,121–30.

121. G.Zhang, L.Fan, Z.Niu, K.Jiao, H.Diao, Q.Du , Energy Convers Manag, 2015, 106, 510–9.

122. ZQ.Niu, SH.Yu, QS.Li , Int J Heat Mass Transfer, 2015, 85,12–32.

123. X.Ma, G.Shu, H.Tian, W.Xu, T.Chen Appl Energy 2019, 248, 614–25.

124. Z-G.Shen, S-Y.Wu, L.Xiao, Energy Conversion and Management, 2017, 150, ,704-713.

125. Z-GG.Shen, X.Liu, S.Chen, SY.Wu, L.Xiao, Z-XX. Chen, Energy, 2018, 157, 297–313.

126. S.Shittu, G.Li, X.Zhao, X.Ma, YG.Akhlaghi, E. Ayodele , Energy Convers Manag, 2019, 184,180–93.

127. A. Yusuf, N. Bayhan, A.him, H. Tiryaki and S. Ballikaya, Int J Energy Res. 2021, 45, 9382–9395

128. Y. Zhu, D. W. Newbrook, P.Dai, C.H. Kees de Groot, R. Huang, Applied Energy, 2022, 305, 117800.

129. S.Turenne, T.Clin, D.Vasilevskiy, RA.Masut J Electron Mater, 2010, 39,1926–33.

130. J-L.Gao, Q-G.Du, X-D.Zhang, X-Q. Jiang, J Electron Mater 2011; 40:884–8

131. F.Cheng, Y.Hong, W.Li, X.Guo, H.Zhang, F.Fu, Energy 2017; 121:545–60.

132. L.Fan, G.Zhang, R.Wang, K.Jiao , Energy Convers Manag, 2016, 122,85–94.

133. H.He, Y.Wu, W.Liu, M.Rong, Z.Fang, X.Tang ,Energy Convers Manag, 2019 183,645–59.

134. YJ.Cui, BL.Wang, KF.Wang, and L.Zheng , Int J Heat Mass Transf 2019; 137:979–89.

135. R.Lamba, SC.Kaushik, Energy Convers Manag, 2017, 144, 388–98.

136. A.abián-Mijangos, G.Min, J.Alvarez-Quintana, Energy Convers Manag 2017; 148:1372–81

137. S.Shittu, G.Li, X.Zhao, X.Ma, YG.Akhlaghi, E.Ayodele, J Power Sources 2019; 428:53–66.

138. R. Lamba, S.C. Kaushik, S.K. Tyagi, Int J Energy Res. 2017; 1–15.

139. Y. Thimont and S. LeBlanc, Journal of Applied Physics, American Institute of Physics, 2019, 126 (9), pp.095101.

140. M.Li, H. Sadighi Dizaji, S. Asaadi, F.Jarad, A.E. Anqi and M. Wae-hayee, Case Studies in Thermal Engineering, 2021,27 , 101314.

141. Q. Doraghi, N. Khordehgah, A. Zabniei´nska-Góra, L.Ahmad, L. Norman, D. Ahmad and H. Jouhara, ChemEngineering 2021, 5, 45.

142. AS.Al-Merbati, BS.Yilbas, AZ.Sahin , Appl Therm Eng 2013; 50:683–92.

143. Y.Mu, G.Chen, R.Yu, G.Li, P.Zhai, P.Li Mater Sci Semicond Process, 2014; 17:21–6.

144. U.Erturun, K.Erermis, K.Mossi, Appl Therm Eng 2014; 73:128–41.

145. U.Erturun, Kumasi, Appl Therm Eng 2015; 85:304–12.

146. U.Erturun, K.Erermis, Kumasi, Appl Energy 2015; 159:19–27.

147. L. Bakhtiaryfard, YS.Chen Adv Mech Eng 2015; 7:1–22.

148. I. OI, Energy 2019; 180:90–106.

149. N. K. KARRI and C. MO, Journal of ELECTRONIC MATERIALS, 2018, 47, 6101-6120.

150. J.Dongxu, W.Zhongbao, J.Pou, S.Mazzoni, S.Rajoo, A.Romagnoli, Energy Convers Manag 2019; 195:236–43.

151. X.Liang, X.Sun, H.Tian, G.Shu, Y.Wang, X.Wang , Appl Energy 2014; 130:190–9.

152. D.Luo, R.Wang, W.Yu, W.Zhou , Renew Energy 2020; 154:542–52.

153. Z,Miao, X.Meng, S.Zhou, M.Zhu, Renew Energy 2020; 147:2272–8.

154. X. Meng, R. O. Suzuki, Applied Thermal Engineering, 2016, 99,, 352–357.

155. M-W. Tian, L. Mihardjo, H. Moria, S. Asaadi, S. Pourhedayat, H. S. Dizaji, M. Wae-hayee, Applied Thermal Engineering, 2021, 184, 5,116274.

153. X.Wang, H. Wang, W. Su, T. Wang, M. A. Madre, J. Zhai, T. Chen, A. Sotelo, and C. Wang, Novel multilayer composite structured thermoelectric module with high output power, Journal of Materials Chemistry A, 2020, 6.

157. MY. Lee, J-H. Seo, H-S. Lee and K. S. Garud, Symmetry 2020, 12, 786.

158. C. Oztan, R. Welch and S. LeBlanc, Energie,s 2022, 15, 3121

159. B. Nagarajan, Z. Hu, X. Song, W. Zhai, J. Wei, Development of Micro Selective Laser Melting: The State of the Art and Future Perspectives, Engineering 5, 2019, 702–720.

160. Y.Xia, GM.Whitesides, Angew Chem Int 1998, Ed 37, 550–75.

161. S.Mihailov, S.Lazare, Appl Optic 1993, 32, 6211–6218

162. JD.Madden, IW.Hunter, J Microelectromech Syst 1996, 5, 24–32

163. A.Bertsch, H.Lorenz, P.Renaud (). In: Proceedings of the IEEE International Conference on Micro Electro Mechanical Systems (MEMS), 1998, 18–23.

164. W.Ehrfeld, A Schmidt, J Vac Sci Technol B, 1998, 16, 3526–34

165. A. Sarbajna, A. Georg Rösch, L. Franke, U.Lemmer, M.M.Mallick, Advanced Engineering Materials, 2023, Volume25, Issue2.

166. DS.Engstrom, B.Porter, M.Pacios, H.Bhaskaran, J Mater Res 2014; 29(17):1792–816.

167. L.Hirt, A.Reiser, R.Spolenak, T.Zambelli, Adv Mater 2017; 29(17):1604211.

168. A.Bertsch, P.Renaud, Stereolithography. Boston: Springer; 2011. p. 81–112.

169. SH.Ko, J.Chung, N.Hotz, KH.Nam, CP.Grigoropoulos, J Micromech Microeng 2010; 20(12):125010.

170. PK.Gokuldoss, S.Kolla, J.Eckert, Materials (Basel) 2017; 10(6):672.

171. P.Regenfuss, R.Ebert, H.Exner, Laser Tech J 2007; 4(1):26–31.

172. A.Davoudinejad, In Additive Manufacturing 2021, 159–181.

173. C. Sun, N. Fang, D.M. Wu, X. Zhang, Sensors and Actuators A 121, 2005, 113–120.

174. A. Ovsianikov, J. Viertl, B. Chichkov, M. Oubaha, B. MacCraith, I. Sakellari, A. Giakoumaki, D. Gray, M. Vamvakaki, M. Farsari, and C. Fotakis, ACS Nano, 2008, 2, NO. 11, 2257–2262.

175. M.He, Y.Zhao, B.Wang, Q.Xi,J.Zhou, Z. Liang, Small 2015, 11, 5889–5894.

176. K.Fredrick, C.Seungjunand S.S.Jae , , 2021, Chapter 13.

177. D.Park, S.Lee, J.Kim, Compos. Commun. 2022, 30, 101084.

178. M.Ferhat, J.Nagao, J. Appl. Phys. 2000, 88, 813–816.

179. D.Park, S.Lee, J.Kim, Sci. Rep. 2021, 11, 16683.

180. J.Fischer, M.Kniepkamp, E.Abele, Micro In: Proceedings of the 25th Annual International Solid Freeform Fabrication (SFF) Symposium; 2014, 22–35.

181. N.Roy, C.Foong, M.Cullinan In: Proceedings of the 27th Annual International Solid Freeform Fabrication Symposium, 2016, 1495–508.

182. NK.Roy, CS.Foong, MA. Cullinan , Addit Manuf 2018; 21:17–29.

183. AT.Sutton, CS.Kriewall, MC. Leu, JW.Newkirk In: Proceedings of the 27th Annual International Solid Freeform Fabrication Symposium; 2016, 1004–30.

184. P.Regenfuss, A.Streek, L.Hartwig, S.Klötzer, T.Brabant, M.Horn, Rapid Prototyping J 2007; 13(4):204–12.

185. A.Cohen, E.Kruglick () EFAB technology and applications. In: Gad-el-Hak M (ed) The MEMS handbook, vol 2nd. CRC Press, Boca Raton, 2006.

186. P.Regenfuss, A.Streek, F.Ullmann, C.Kühn, L.Hartwig, M.Horn, Interceram 2008; 57(1):6–9.

187. P.Regenfuss, L.Hartwig, S.Klötzer, R.Ebert, H.Exner, In: Proceedings of Rapid Prototyping and Manufacturing Conference; 2003 Paper no.: TP04PUB185

188. A .Streek, P.Regenfuss, R.Ebert, H.Exner; In: Proceedings of the 19th Annual International Solid Freeform Fabrication Symposium; 2008 , 297–308.

189. M. Gieseke, V. Senz, M.Vehse, S.Fiedler, R.Irsig, M.Hustedt, Biomed Tech 2012; 57(Suppl 1):398–401.

190. C. Noelke, M. Gieseke, S. Kaierle, J Laser Appl 2013, 1, 1–6.

191. M. Kniepkamp, J. Fischer, E. Abele In: Bourell DL, editor. Proceedings of the 27th Annual International Solid Freeform Fabrication Symposium; 2016 1530–7.

192. RC .Roberts, NC.Tien In: Proceedings of 2017 19th International Conference on Solid-State Sensors, Actuators and Microsystems, 2017, 1233–6.

193. P. Regenfuss, R .Ebert, H.Exner, Laser Tech J 2007; 4(1):26–31.

194. S. Dudziak, M. Gieseke, H. Haferkamp, S. Barcikowski, D. Kracht, Functionality of laser-sintered shape memory micro-actuators Physics Procedia,2010, 5, 607-615

195. I .Yadroitsev, P.Bertrand Annals of DAAAM for 2010 & Proceedings of the 21st International DAAAM Symposium. Vienna: DAAAM International; 2010.

196. L.Gomell, M.Roscher, H.Bishara, E.A.Jägle, C.Scheu, B.Gault, Scr. Mater. 2020, 193, 153–157.

197. B.Feng, G.Li, X.Hu, J. Alloy. Compd. 2020, 818, 152899.

198. A. R. A.El-Desouky, P.Bardet, M.Andre, & S.LeBlanc, (). Proceedings of Solid Freeform Fabrication Symposium, 2015, 1043.

199. A.El-Desouky, M.Carter, M.Mahmoudi, A.Elwany, & S. LeBlanc, Journal of Manufacturing Processes, 2017, 25, 411.

200. J.hi, H.Chen, S.Jia, & W.Wang, (2019). Journal of Manufacturing Processes, 2019, 37, 370.

201. J.Qiu, Y.Yan, T.Luo, K.Tang, , L.Yao, , J.Zhang, , X.Tang, (). 3D Printing of highly textured bulk thermoelectric materials: Mechanically robust BiSbTe alloys with superior performance, Energy Environ. Sci., 2019, 12, 3106-3117.

202. A.El-Desouky, M.Carter, M.A.Andre, P.M.Bardet, S.LeBlanc, Mater. Lett. 2016, 185, 598–602.

203. A. El-Desouky, M. Carter, M. Mahmoudi, A.Elwany, S.LeBlanc, J. Manuf. Process. 2017, 25, 411–417.

204. X. Su, H. Li, Y. Yan, G. Wang, H. Chi, X. Zhou, C. Uher, Acta Materialia, 2012, 60, 3536.

205. H. Li, X.Tang, X. Su, & Q. Zhang, Applied Physics Letters, 2008, 92, 202114.

206. G.Li, S.Bajaj, U.Aydemir, S.Hao, H. Xiao, , W. A. Goddard, , G. J. Snyder, Journal of Materials Chemistry, 2016, 28, 2172.

207. Y.Yan, H. Ke, J.Yang, C.Uher, & X. Tang, ACS Applied Materials & Interfaces, 2018, 10, 13669.

208. H.Zhang, S.Wang, P.J Taylor, J. Yang, S. LeBlanc, Materials, Devices, and Applications VIII; International Society for Optics and Photonics: Bellingham, WA, USA, 2018, 10663,106630B.

209. Y. Thimont, L. Presmanes, V.Baylac, P. Tailhades, D.Berthebaud, F. Gascoin, Mater. Lett. 2018, 214, 236–239.

210. J. Shi, X. Chen, W. Wang, H.Chen, Mater. Sci. Semicond. Process. 2020, 123, 105551.

211. K. Wu,; Y.Yan, J. Zhang, Y.Mao, H.Xie, J.Yang, Q.Zhang, C. Uher, X.Tang, Phys. Status solidi (RRL)–Rapid Res. Lett. 2017, 11, 1700067.

212. L.E. Murr, E. Martinez, S.M. Gaytan, D.A. Ramirez, B.L. Machado, P.W. Shindo,J.L. Martinez, F. Medina,J. Wooten,D. Ciscel, Met. Mater. Trans. A, 2011, 42, 3491–3508.

213. R. Welch,D. Hobbis, A.J.Birnbaum, , Adv. Mater. Interfaces 2021, 8, 2100185.

214. G. Li,Q. An, W. Li, I.W.A. Goddard,P. Zhai,Q. Zhang, G.J. Snyder, Chem. Mater. 2015, 27, 6329–6336.

215. G. Li, Q. An,W.A. Goddard, ,Acta Mater. 2016, 103, 775–780.

216. W. Pei, W. Zhengying, C. Zhen, L. Junfeng, Z. Shuzhe, D. Jun, Appl. Phys. A, 2017, 123, 540.

217. Y. Li, D. Gu, Addit. Manuf. 2014, 1, 99–109.

218. M. Khan, N.A. Sheikh, S. Jaffery, Lasers Eng. 2014, 28, 319–336. 100.

219. P. Ansari, M.U. Salamci, J. Alloy. Compd. 2021, 890, 161873.

220. K.H. Leitz, P. Singer A. Plankensteiner, B. Tabernig, H. Kestler, L. Sigl, Met. Powder Rep. 2017, 72, 331–338.

221. P. Yuan, D. Gu, J. Phys. D Appl. Phys. 2015, 48, 035303.

222. Q. Tang, P. Chen, , J. Chen, Y. Chen, H. Chen, Optik 2019, 201, 163336.

223. W. King, A.T. Anderson, R.M. Ferencz. N.E. Hodge, C. Kamath, S.A. Khairallah, Mater. Sci. Technol. 2015, 31, 957–968.

224. L. Yang, Z-G. Chen, M. S. Dargusch, J. Zou, Advanced energy materials, 2018 .8. 6.

225. X. Shi, J. Zou, and Z-G. Chen, Chem. Rev. 2020, 120, 15, 7399–7515

226. J. Gonzalez-Gutierrez, S. Cano, S. Schuschnigg, C. Kukla, J. Sapkota and C. Holzer, Materials 2018, 11, 840

227. I. Gibson, D. Rosen, B. Stucker, 2021, 17.

228. S.C. Daminabo, S. Goel, S.A. Grammatikos, H.Y. Nezhad, V.K. Thakur, Mater. Today Chem. 2020, 16, 100248.

229. J. Wang, H. Li, R. Liu, Compos. Sci. Technol. 2018, 157, 1–9.

230. C. Oztan, S. Ballikaya, U. Ozgun, R. Karkkainen, E. Celik, Appl. Mater. Today 2019, 15, 77–82.

231. C. Kenel, M. Al Malki, D. Dunand, Acta Mater. 2021, 221, 117422.

232. F. Kim, B. Kwon, Y. Eom, J.E. Lee, S. Park, S. Jo, S.H. Park, B.S. Kim, H.J. Im, M.H. Lee ,Nat. Energy 2018, 3, 301–309.

233. M.V. Kovalenko,, B. Spokoyny, J.S. Lee, M. Scheele, A. Weber, S. Perera, D.V. Talapin , Journal of the American Chemical Society, 2010, 132, 6686.

234. Y. Eom, F. Kim, S. Eun Yang, J. Sung Sona, H. Gi Chae, Journal of Rheology, 2019, 63(2), 291-304

235. S. Eun Yang, F. Kim, F. Ejaz, G. Seung Lee, H. Ju, S. Choo, J. Lee, G. Kim, S. Jung, S. Ahn, H. Gi Chae, K. Tae Kim, B. Kwon, J. Sung Son, Nano Energy, 2021,81,105638.

236. F. Kim,S. Eun Yang, H. Ju, S. Choo, J. Lee, G. Kim, S. Jung, S. Kim, C. Cha, K. Tae Kim, S. Ahn, H. Gi Chae and J. Sung Son, Nature Electronics, 2021, 4,579–587.

237. R. Danaei, T. Varghese, M. Ahmadzadeh, J. McCloy, C. Hollar, M. Sadeq Saleh, J. Park, Y. Zhang, R. Panat, Advance Engineering Materials, 2019, 21, 1

Saeed Asadi has a strong background in metallurgy of various kinds of materials as well as design appreciation. He is a highly focused and self-disciplined material specialist with remarkable background in modelling, simulation and manufacturing and has a combined skill of running experiments and using analytical tools for solving complex problems. With high motivation in new manufacturing process and in its impact on the environment, he has been working for several years on several interesting projects, from structural integrity to additive manufacturing. He has published his scientific papers in international journals and presented in international conference.

Ali Zolfagharian

Ali Zolfagharian is recipient of Australian Research Council Discovery Early Career Award and recognized for his innovative direction in 4D printing and has been acknowledged as a top 2% cited scientist by Stanford University and Elsevier for consecutive years. His accolades include the Alfred Deakin Medal for Best Doctoral Thesis and the Alfred Deakin Postdoctoral Fellowship. A co-founder of the 4D Printing Society and co-editor of the Smart Materials in Additive Manufacturing book series, he is a senior lecturer at Deakin University, Australia. His pioneering work spans 118 journal articles, 15 special issues, 8 book chapters, and 5 books in the realm of 3D printing of smart robotic materials.

Mahdi Bodaghi

Mahdi Bodaghi is Senior Lecturer in the Department of Engineering at Nottingham Trent University. He is also the founder and director of the 4D Materials & Printing Lab that hosts a broad portfolio of projects focusing on the multi-physics multi-scale behaviours of smart materials, metamaterials, bio-composites, robotic materials, and 3D/4D printing technologies. His vast experience and research on smart materials and additive manufacturing have led him to co-found the 4D Printing Society and to co-edit the book series- Smart Materials in Additive Manufacturing. His research has also been disseminated as 250 scientific papers in prestigious journals as well as the presentation of his work at major international conferences. Mahdi has also served as Chairman and member of Scientific Committees for 20 International Conferences, as Guest Editor for 10 Journals, as Editorial Board Member for 12 scientific Journals, and as Reviewer for over 150 Journals. Mahdi's research awards include the Best Doctoral Thesis Award of 2015, 2016 CUHK Postdoctoral Fellowship, the Annual Best Paper Award in Mechanics and Material Systems presented by ASME in 2017, 2018 Horizon Fellowship Award, 2021 IJPEM-GT Contribution Award recognized by the Korea Society for Precision Engineering, and SLAS Technology Authors Choice Award.